UNIVERSITY OF STRATHCLYDE
DEPARTMENT OF PHYSICS

Localisation of Bose-Einstein Condensates in Optical Lattices

by

Russell Campbell

A thesis submitted in partial fulfillment for the degree of Doctor of Philosophy

June 2018

Declaration of Authorship

This thesis is the result of the author's original research. It has been composed by the author and has not been previously submitted for examination which has led to the award of a degree.

Signed: 

Date: 11/06/2018

Abstract

The properties of Bose-Einstein condensates can be studied and controlled effectively when trapped in optical lattices formed by two counter-propagating laser beams. The dynamics of Bose-Einstein condensates in optical lattices are well-described by a continuous model using the Gross-Pitaevskii equation in a modulated potential or, in the case of deep potentials, a discrete model using the Discrete Nonlinear Schrödinger equation. Spatially localised modes, known as lattice solitons in the continuous model, or discrete breathers in the discrete model, can occur and are the focus of this thesis. Theoretical and computational studies of these localised modes are investigated in three different situations.

Firstly, a model of a Bose-Einstein condensate in a ring optical lattice with atomic dissipations applied at a stationary or at a moving location on the ring is presented in the continuous model. The localised dissipation is shown to generate and stabilise both stationary and traveling lattice solitons. The solutions generated include spatially stationary quasiperiodic lattice solitons and a family of traveling lattice solitons with two intensity peaks per potential well with no counterpart in the discrete case. Collisions between traveling and stationary lattice solitons as well as between two traveling lattice solitons display a dependence on the lattice depth.

Then, collisions with a potential barrier of either travelling lattice solitons or travelling discrete breathers are investigated along with their dependence on the height of the barrier. Regions of complete reflection or of partial reflection where the incoming soliton/breather is split in two, are observed and understood in terms of the soliton properties. Partial trapping of the atoms in the barrier is observed for positive barrier heights due to the negative effective mass of the solitons/breathers.

Finally, two coupled discrete nonlinear Schrödinger equations can describe the interaction and collisions of breathers in two-species Bose-Einstein condensates in deep optical lattices. This is done for two cases of experimental relevance: a mixture of two ytterbium isotopes and a mixture of Rubidium (^{87}Rb) and Potassium (^{41}K) atoms. Depending on their initial separation, interaction between stationary breathers of different species can lead to the formation of symbiotic localised structures or transform one of the breathers from a stationary one into a travelling one. Collisions between travelling and stationary discrete breathers composed of different species are separated in four distinct regimes ranging from totally elastic when the interspecies interaction is highly attractive to mutual destruction when the interaction is sufficiently large and repulsive.

Acknowledgements

I would like to thank my supervisor Gian-Luca Oppo for his help and patience throughout my PhD. I am also grateful for the help of Mateusz Borkowski, a collaborator on one of my papers. I would also like to thank my family and friends for their support over the past few years. Lastly I would like to thank the Glasgow Lindy Hop community for lifting my spirits when needed and keeping me sane.

Contents

List of Figures

List of Tables

Publications and Conference Presentations

Published Papers

- R. Campbell, G.-L. Oppo and M. Borkowski, "Interactions and collisions of discrete breathers in two-species Bose-Einstein condensates in optical lattices", Phys. Rev. E **91**, 012909 (2015)
- R. Campbell and G.-L. Oppo, "Stationary and traveling solitons via local dissipation in Bose-Einstein condensates in ring optical lattices", Phys. Rev. A **94**, 043626 (2016)

Conference Contributions

- R. Campbell, M. Borkowski and G.-L. Oppo, "Collision of Discrete Breathers in Two-Species Bose-Einstein Condensates in Optical Lattices", poster presentation at CLEO/Europe-IQEC 2013, Munich (2013)

- R. Campbell, M. Borkowski and G.-L. Oppo, "Collisions of Discrete Breathers in Two-Species Bose-Einstein Condensates in Optical Lattices", poster presentation at the workshop "From Dynamics to Statistical Mechanics and Back", Dresden (2013)

- R. Campbell, G.-L. Oppo and M. Borkowski, "Interaction of Breathers in the Two-Component Discrete Nonlinear Schrodinger Equation", poster presentation at Nonlinear Photonics, Barcelona (2014) and DOQS 2014 - Workshop on Many-Body Dynamics and Open Quantum Systems, Glasgow (2014)

- R. Campbell, G.-L. Oppo and M. Borkowski, "Interactions of two-species Bose-Einstein condensates in optical lattices", Oral presentation at Photon14, London (2014)

Chapter 1

Introduction

This thesis investigates the theory, simulations and applications of Bose-Einstein Condensates (BECs) in optical lattices, and in particular, localised modes in this setting. What follows in this chapter is a brief review of BECs and BECs in optical lattices.

1.1 Bose-Einstein Condensates

Bose-Einstein Condensates were predicted by Bose in 1924 [1], saying that photons of the same energy were indistinguishable, and Einstein, who extended this idea to atoms [2, 3], resulting in Bose-Einstein statistics. This consequently predicted that when cooling an ensemble of bosons to low temperatures (near absolute zero), the bosons will collectively condense into the lowest quantum state. This transition to a macroscopic occupation of a single quantum state is known as Bose-Einstein condensation.

This transition can be characterised by the phase-space density $n\lambda_{dB}^3$, where λ_{dB} is the deBroglie wavelength of the atoms and n is the number density. As the

temperature is lowered, the deBroglie wavelength of the atoms gets bigger. When $n\lambda_{dB}^3 \sim 1$ (i.e. when the wavelength becomes comparable to the spacing between the atoms), the waves of the atoms overlap and Bose-Einstein condensation occurs.

Effects attributed to BEC were observed early on in different areas, for example, in studies of liquid Helium [4]. Due to the strong interactions of atoms in a liquid (as opposed to a dilute gas), only a small amount of atoms would condense to the lowest state. It would be 90 years until the first BEC was realised experimentally, when the needed cooling technology was finally available. With laser cooling, clouds of atoms can be cooled down to temperatures of a few hundreds of micro-Kelvins. The atoms, held in a magnetic or optical trap, can then be evaporatively cooled to temperatures as low as a few nano-Kelvins by lowering the trap depth to allow the most excited atoms to leave and the ones left to rethermalize. Bose-Einstein condensation was first observed in 1995 with experiments on vapours of rubidium and sodium [5, 6], and the groups involved earned the 2001 Nobel Prize for this work [7, 8].

1.1.1 BECs in Optical Lattices

This thesis is concerned with BECs trapped in optical lattices (see [9] for a review), in which we have a periodic potential. The periodic potentials are formed from the interference patterns of two or more laser beams. Here, only one-dimensional lattices are considered, caused by two identical laser beams counterpropagating so that they overlap. The distance between the lattice minima, or the lattice spacing, is given by $d = \lambda_L/2$, with λ_L as the laser wavelength and a typical resulting periodic potential is given by $V(x) = E_0 \sin^2(\pi x/d)$ with E_0 as the potential depth.

When trapped by an optical lattice, BECs have similarities with solid-state systems (i.e. electrons in crystal lattices). An advantage here is that there is almost complete control of the parameters (e.g. potential depth and lattice spacing) of the potentials created from the lattice. Compared to studying cold atoms in optical lattices, there are several advantages in using BECs. The low temperatures mean that the BEC will often be in the lowest levels of the potential wells without need for further cooling. Also, the high atomic densities mean that the effects due to atom-atom interactions become more important, enhancing the nonlinearity.

If the potential wells in the lattice are sufficiently deep, the atomic density at the minima will increase. If the wells are close enough that the condensate atoms can tunnel through to the other wells, the condensate spreads throughout the lattice to the other sites. The nonlinearity, however, increases as the atomic density increases, since it occurs due to the atom-atom interaction. An interesting result of this is the onset of self-localisation leading to the formation of lattice solitons [10, 11].

Solitons are localised solutions of nonlinear wave equations. First observed by John Scott Russell in the waters of the Union Canal near Edinburgh in 1834 [12], solitons are present in a wide variety of nonlinear media. In the case without a lattice, bright solitons, which are localised peaks in the wavefunction, are formed with attractive BECs[1] (as demonstrated experimentally in [13, 14]). These are the result of the interplay between the dispersion and nonlinearity. In a lattice, bright solitons can exist for both repulsive and attractive BECs. Bright lattice solitons have been experimentally obtained with repulsive BECs [15]. This is because the dispersion relation is changed due to the periodic potential, making anomalous dispersion possible, characterised by a negative effective mass.

[1] Dark solitons, localised dips, are formed with repulsive BECs, but in this thesis we will only concentrate on bright solitons. For an experimental example, see [16].

The evolution of the wavefunction of a BEC in an optical lattice is well described by the Gross-Pitaevskii (GP) equation, which is a nonlinear Schrödinger equation with an extra term that accounts for the external potential, which is, in our case, periodic. This situation may also be investigated using the discrete nonlinear Schrödinger equation (DNLS), which is relevant for deep potentials. The equivalent of lattice solitons here are known as discrete breathers (due to the oscillating real and imaginary parts of the wavefunction). In this thesis, lattice solitons are examined in the GP equation, and discrete breathers in the DNLS equation.

1.2 Arrays of Optical Waveguides

The results in this thesis can be generalized to the analogous situation of light travelling through arrays of optical waveguides. A well-known example of an optical waveguide is an optical fibre. In optics, a typical waveguide is one in which a core region is surrounded with a material with a lower refractive index.

In a waveguide array, in which identical waveguides are equally spaced, the refractive index has a periodic profile. The light sees this as a periodic potential, like atoms see an optical lattice. If the waveguides are close enough to each other, the light fields from each waveguide overlap, and light can travel from one waveguide to another. This diffraction was studied theoretically in 1965 [17] and first realised experimentally using gallium arsenide waveguide arrays in 1973 [18]. It was not until 1988 [19] that it was shown that in nonlinear waveguide arrays, light could localise. This happens when the on-site nonlinearity is balanced with the linear diffraction. The optical beam is then trapped in a few waveguide sites creating an optical soliton. This was first realised experimentally in aluminium gallium arsenide waveguide arrays ten years later in 1998 in Glasgow [20].

This system can be described by the same equations as those of BECs in optical lattices. In this thesis we concentrate on BECs in optical lattices. However, the results should apply to the analogue of light in arrays of optical waveguides. A review of this can be found in [21].

1.3 Outline

The thesis is structured as follows. The continuous and discrete models that describe BECs in optical lattices are introduced in chapter 2, along with some of the basic concepts relating to localisation.

In chapter 3, we present a model of a BEC in a ring optical lattice with atomic dissipation using the GPE with angular coordinates. The localized dissipation can be applied at a stationary or moving location on the ring and is shown to generate and stabilise stationary and travelling lattice solitons. Interesting results presented here include stationary quasiperiodic lattice solitons and travelling lattice solitons with two intensity peaks per potential well that cannot be described in the discrete model. We then investigate collisions between stationary and travelling lattice solitons and between two travelling lattice solitons.

In chapter 4, the collision of travelling lattice solitons with potential defects in the form of Gaussians in the lattice is investigated. The collisions' dependence on the height of the barrier is studied.

In Chapter 5, the dynamics of breathers in two-species BECs are investigated. Coupled DNLS equations are used to describe the situations of mixtures of Ytterbium isotopes and a mixture of ^{87}Rb and ^{41}K. It is shown that the interaction between static breathers of different species can produce symbiotic breathers composed of both species or can change one of the static ones into a travelling one,

depending on the initial distance between the two breathers. Collisions between static and travelling breathers composed of different species are then investigated and separated into four regimes that depend on the interspecies interaction. These regimes range from elastic when the interspecies interaction is large and attactive to mutual destruction with a large, repulsive interaction. Finally, collisions of travelling lattice solitons in the continuous GP equation are investigated that support the results found in the DNLS equation.

Chapter 2

Theoretical Models

In this chapter, the theoretical models used in the thesis to describe BECs in optical lattices are introduced. First of all, the Gross-Pitaevskii equation is examined. A normalised, one-dimensional version of the Gross-Pitaevskii equation is then derived. The band structure and examples of localisation in this model from the literature are briefly discussed. Finally, the Discrete Nonlinear Schrödinger equation is derived and examples of localisation, along with methods used to induce this, are discussed.

2.1 The Gross-Pitaevskii Equation with a Periodic Potential

The many-body Hamiltonian for N interacting bosonic atoms with atomic mass m and unnormalised spatial coordinates $\mathbf{r} = (X, Y, Z)$ in the second quantisation is [22]:

$$\hat{H} = \int d\mathbf{r}\hat{\Psi}^{\dagger}(\mathbf{r}) \left[-\frac{\hbar}{2m}\nabla^2 + V_{\text{ext}}(\mathbf{r}) \right] \hat{\Psi}(\mathbf{r}) + \frac{1}{2} \int d\mathbf{r} d\mathbf{r}' \hat{\Psi}^{\dagger}(\mathbf{r}) \hat{\Psi}^{\dagger}(\mathbf{r}') V(\mathbf{r} - \mathbf{r}') \hat{\Psi}(\mathbf{r}') \hat{\Psi}(\mathbf{r}) \tag{2.1}$$

where $\hat{\Psi}^{\dagger}(\mathbf{r})$ and $\hat{\Psi}(\mathbf{r})$ are the boson creation and annihilation field operators respectively, V_{ext} is the confining potential, and $V(\mathbf{r}' - \mathbf{r})$ is the two-body interatomic potential.

Making use of a mean-field description based on the Bogoliubov approximation [23], the bosonic field operator $\hat{\Psi}(\mathbf{r})$ is given as:

$$\hat{\Psi}(\mathbf{r}, T) = \Psi(\mathbf{r}, T) + \hat{\Psi}'(\mathbf{r}, T) \tag{2.2}$$

Here, $\Psi(\mathbf{r}, T)$ is described as the"macroscopic wavefunction of the condensate", at unnormalised time T, defined as the expectation value of the field operator (i.e. $\Psi(\mathbf{r}, T) = \left\langle \hat{\Psi}(\mathbf{r}, T) \right\rangle$). The remaining operator, $\hat{\Psi}'(\mathbf{r}, T)$, represents the non-condensate part, and is assumed to be negligible. Then, from the Heisenberg equation of motion $i\hbar\partial\hat{\Psi}/\partial T = [\hat{\Psi}, \hat{H}]$ for the field operator, we obtain

$$i\hbar \frac{\partial \hat{\Psi}(\mathbf{r}, T)}{\partial T} = \left[-\frac{\hbar}{2m}\nabla^2 + V_{\text{ext}}(\mathbf{r}) + \int d\mathbf{r}' \hat{\Psi}^{\dagger}(\mathbf{r}', T) V(\mathbf{r}' - \mathbf{r}) \hat{\Psi}(\mathbf{r}', T) \right] \hat{\Psi} \tag{2.3}$$

In the case of a dilute ultracold gas with binary collisions at low energy, the interatomic potential can be described by a delta-function interaction potential, $V(\mathbf{r}' - \mathbf{r}) = g\delta(\mathbf{r}' - \mathbf{r})$, where

$$g = 4\pi\hbar^2 a/m \tag{2.4}$$

with a being the s-wave scattering length [22]. Employing this and replacing $\hat{\Psi}$ with the classical field Ψ, Eq. (2.3) becomes

$$i\hbar\frac{\partial\Psi(\mathbf{r},T)}{\partial T} = \left[-\frac{\hbar}{2m}\nabla^2 + V_{\text{ext}}(\mathbf{r}) + g|\Psi(\mathbf{r},T)|^2\right]\Psi \tag{2.5}$$

which is the Gross-Pitaevskii equation. In a typical optical lattice experiment, the external potential $V_{\text{ext}}(\mathbf{r})$ is given by

$$V_{\text{ext}}(\mathbf{r}) = E_0\sin^2\left(\frac{\pi X}{L}\right) + \frac{1}{2}m\left(\omega_X^2X^2 + \omega_\perp^2(Y^2+Z^2)\right) \tag{2.6}$$

in which the first term describes the periodic potential arising from the optical lattice with E_0 as the potential depth and L as the lattice period, and the second term describes the harmonic trapping potential, with ω_X and $\omega_\perp$ the trap frequencies in the X direction and Y-Z directions respectively.

Assuming that the external potential V_{ext} is constant, the GP equation conserves both the number of particles N:

$$N = \int|\Psi(\mathbf{r},T)|^2 d\mathbf{r}, \tag{2.7}$$

and the energy of the system E:

$$E = \int d\mathbf{r}\left[\frac{\hbar}{2m}|\nabla\Psi|^2 + V_{\text{ext}}|\Psi|^2 + \frac{1}{2}g|\Psi|^4\right]. \tag{2.8}$$

In Eq. (2.8), the three terms on the right hand side represent, from left to right, the kinetic energy, the potential energy and the interaction energy.

2.2 Scattering length and Feshbach resonances

Assuming the BEC is dilute, binary collisions dominate, defined by the s-wave scattering length a. This may have both negative and positive values, representing attractive or repulsive interactions respectively. ^{87}Rb, ^{23}Na, ^{168}Yb, ^{170}Yb and ^{174}Yb are examples of atomic species that form repulsive BECs, while ^{85}Rb, ^{7}Na and ^{176}Yb form attractive ones.

However, it is possible to control the atomic interactions by applying an external magnetic field B. Atoms can form bound states, or molecules, during the collisions. The external magnetic field can be used to control the energy difference between the atomic and molecular states providing their magnetic moments are different. The energies of the molecular and atomic states are equal at a so-called Feshbach resonance (see [24, 25] for a review).

Due to this, the s-wave scattering length can be varied by changing the external magnetic field. The value of the scattering length as a function of the external field B is given as [26, 27]:

$$a(B) = \widetilde{a}\left(1 - \frac{\Delta}{B - B_0}\right) \tag{2.9}$$

where $\widetilde{a}$ is the scattering length far from resonance, Δ is the width of the resonance and B_0 is the resonance position.

2.3 The 1D Gross-Pitaevskii Equation - The Continuous Model

The Gross-Pitaevskii equation can be reduced so that it is effectively one dimensional. With $\omega_\perp \gg \omega_X$, the trap is elongated in the X direction, providing what

can be referred to as a "cigar-shaped BEC". The wavefunction is separated into longitudinal (in the X direction) and transverse (in the Y-Z plane) components and expressed as

$$\Psi(X,Y,Z;T) = U(Y,Z)\psi(X,T) \tag{2.10}$$

Due to the tight confinement in the Y-Z plane, it is assumed that $U(Y,Z) = A_\perp \exp\left[-\frac{m\omega_\perp}{2\hbar}(Y^2+Z^2)\right]$, which is the ground state of the two-dimensional quantum harmonic oscillator.

Substituting Eq.(2.10) and Eq.(2.6) into Eq.(2.5) gives

$$\begin{aligned} i\hbar U\frac{\partial\psi}{\partial T} &= -\frac{\hbar}{2m}U\frac{\partial^2\psi}{\partial X^2} - \frac{\hbar}{2m}\psi\nabla_\perp^2 U \\ &\quad + E_0\sin^2\left(\frac{\pi X}{L}\right)U\psi + \frac{1}{2}m\omega_X^2X^2U\psi + \frac{1}{2}m\omega_\perp^2(Y^2+Z^2)U\psi \\ &\quad + g|U|^2|\psi|^2U\psi \end{aligned} \tag{2.11}$$

where $\nabla_\perp^2 = \partial^2/\partial Y^2 + \partial^2/\partial Z^2$ is the transverse Laplacian operator.

From the expression for $U(Y,Z)$ we get:

$$\begin{aligned} \nabla_\perp U &= \frac{\partial U}{\partial Y} + \frac{\partial U}{\partial Z} \\ &= -\frac{m\omega_\perp}{\hbar}(Y+Z)U\,, \end{aligned} \tag{2.12}$$

$$\begin{aligned} \nabla_\perp^2 U &= -\frac{m\omega_\perp}{\hbar}\left(U + \frac{\partial U}{\partial Y} + U + \frac{\partial U}{\partial Z}\right) \\ &= -\frac{2m\omega_\perp}{\hbar}U + \frac{m^2\omega_\perp^2}{\hbar^2}(Y^2+Z^2)U\,, \end{aligned} \tag{2.13}$$

$$\Rightarrow -\frac{\hbar^2}{2m}\nabla_\perp^2 U + \frac{1}{2}m\omega_\perp^2(Y^2+Z^2)U - \hbar\omega_\perp U = 0 \tag{2.14}$$

Then, applying the transformation $\psi \to \psi \exp(-i\omega_\perp T)$ and using Eq. (2.14), Eq. (2.11) becomes:

$$\begin{aligned} i\hbar U\frac{\partial\psi}{\partial T} &= \left(-\frac{\hbar^2}{2m}\nabla_\perp^2 U + \frac{1}{2}m\omega_\perp^2(Y^2+Z^2)U - \hbar\omega_\perp U\right)\psi \\ &\quad -\frac{\hbar}{2m}U\frac{\partial^2\psi}{\partial X^2} + E_0\sin^2\left(\frac{\pi X}{L}\right)U\psi + \frac{1}{2}m\omega_X^2X^2U\psi \\ &\quad +g|U|^2|\psi|^2U\psi \\ &= -\frac{\hbar}{2m}U\frac{\partial^2\psi}{\partial X^2} + E_0\sin^2\left(\frac{\pi X}{L}\right)U\psi + \frac{1}{2}m\omega_X^2X^2U\psi \\ &\quad +g|U|^2|\psi|^2U\psi \end{aligned} \tag{2.15}$$

The resulting equation is then mutliplied through by $U^* = U$ and integrated over the Y and Z directions, while assuming $\iint_{-\infty}^{\infty}|U|^2\,\mathrm{d}Y\,\mathrm{d}Z = 1$, to obtain:

$$\begin{aligned} i\hbar\frac{\partial\psi}{\partial T} &= -\frac{\hbar}{2m}\frac{\partial^2\psi}{\partial X^2} + E_0\sin^2\left(\frac{\pi X}{L}\right)\psi + \frac{1}{2}m\omega_X^2X^2\psi \\ &\quad +g|\psi|^2\psi\iint_{-\infty}^{\infty}|U|^4\,\mathrm{d}Y\,\mathrm{d}Z \end{aligned} \tag{2.16}$$

Since $|U|^2 = A_\perp^2\exp\left[-\frac{m\omega_\perp}{\hbar}(Y^2+Z^2)\right]$, and using the definite integral $\int_{-\infty}^{\infty}\exp(-aX^2)\,\mathrm{d}X = \sqrt{\pi/a}$,

$$\begin{aligned} \iint_{-\infty}^{\infty}|U|^2\,\mathrm{d}Y\,\mathrm{d}Z &= A_\perp^2\int_{-\infty}^{\infty}\exp\left(-\frac{m\omega_\perp}{\hbar}Y^2\right)\mathrm{d}Y\int_{-\infty}^{\infty}\exp\left(-\frac{m\omega_\perp}{\hbar}Z^2\right)\mathrm{d}Z \\ &= A_\perp^2\frac{\pi\hbar}{m\omega_\perp} = 1 \\ &\Rightarrow \quad A_\perp = \sqrt{\frac{m\omega_\perp}{\pi\hbar}} \end{aligned} \tag{2.17}$$

which allows us to work out

$$\begin{aligned}\iint_{-\infty}^{\infty} |U|^4 \,\mathrm{d}Y \,\mathrm{d}Z &= A_\perp^4 \int_{-\infty}^{\infty} \exp\left(-\frac{2m\omega_\perp}{\hbar}Y^2\right) \mathrm{d}Y \int_{-\infty}^{\infty} \exp\left(-\frac{2m\omega_\perp}{\hbar}Z^2\right) \mathrm{d}Z \\ &= \frac{m\omega_\perp}{2\pi\hbar} \end{aligned} \tag{2.18}$$

Substituting this into Eq.(2.16), and assuming that the lattice momentum $2\pi/L$ is much greater than the trapping frequency ω_X, allows us to obtain a 1D GP equation, expressed as:

$$i\hbar\frac{\partial\Psi(X,T)}{\partial T} = \left(-\frac{\hbar}{2m}\frac{\partial^2}{\partial X^2} + E_0 \sin^2\left(\frac{\pi X}{L}\right) + g_{1D}|\Psi|^2\right)\Psi\,, \tag{2.19}$$

where the one-dimensional atom-atom interaction parameter is given by $g_{1D} = g\frac{m\omega_\perp}{2\pi\hbar} = 2\hbar\omega_\perp a_s$.

In this thesis, for convenience, we use dimensionless variables. Equation 2.19 is rewritten by normalising $u = \sqrt{L/2N}\Psi$, $x = 2X/L$, $t = T/T_0$ and $V_0 = E_0/E_r$, where $T_0 = mL^2/4\hbar$, $E_r = 4\hbar^2/mL^2$ is the recoil energy and N is the number of atoms (see [11] for similar normalisations). The resulting equation is given by:

$$i\frac{\partial u(x,t)}{\partial t} = \left(-\frac{1}{2}\frac{\partial^2}{\partial x^2} + V_0 \sin^2\left(\frac{\pi x}{2}\right) + \beta|u|^2\right)u\,. \tag{2.20}$$

The nonlinear parameter $\beta = N\omega_\perp a_s mL/\hbar$ is positive for repulsive condensates and negative for attractive ones. In this thesis, only repulsive BECs ($\beta > 0$) such as ^{87}Rb are considered. We will see that they generate bright lattice solitons.

2.3.1 Band Structure of BECs in the Continuous Model

Before introducing nonlinear features such as solitons in the continuous model, it is useful to discuss the linear theory of a non-interacting atoms in periodic potentials. A single atom in a periodic potential $V(x) = V(x+d)$ is governed by the Schrödinger equation:

$$\left(-\frac{1}{2}\frac{\partial^2}{\partial x^2} + V(x)\right)\psi(x) = E\psi(x) \tag{2.21}$$

in our normalised units.

From Bloch's theorem [28], the solutions to Eq. (2.21) can be written as a product of a plane wave and a function with the same periodicity as the potential $V(x)$:

$$\psi_{n,q}(x) = e^{iqx}u_{n,q}(x) \tag{2.22}$$

where

$$u_{n,q}(x) = u_{n,q}(x+d) \tag{2.23}$$

Indices n and q refer to band index and quasimomentum, respectively. Waves of the form of $\psi_{n,q}(x)$ in Eq. (2.22) are known as Bloch waves, with $u_{n,q}(x)$ as Bloch functions. Substituting Eq. (2.22) into Eq. (2.21) gives a Schrödinger equation for $u_{n,q}(x)$ like so:

$$-\frac{1}{2}\left(-q^2 + 2iq\frac{\partial}{\partial x} + \frac{\partial^2}{\partial x^2}\right)u_{n,q}(x) + V(x)u_{n,q}(x) = E_{n,q}u_{n,q}(x) \tag{2.24}$$

Since $u_{n,q}(x)$ and $V(x)$ are periodic, they can be expressed as Fourier series:

$$u_{n,q}(x) = \sum_l c_{l,n,q} e^{ilGx} \tag{2.25}$$

$$V(x) = \sum_r U_r e^{irGx} \tag{2.26}$$

where $G = 2\pi/d$ is the reciprocal lattice vector. Substituting these expressions into Eq. (2.24) allows us to rewrite the kinetic term as

$$-\frac{1}{2}\left(-q^2 + 2iq\frac{\partial}{\partial x} + \frac{\partial^2}{\partial x^2}\right) u_{n,q}(x) = \sum_l \frac{1}{2}\left(q + lG\right)^2 c_{l,n,q} e^{ilGx} \tag{2.27}$$

and the potential term as

$$V(x)u_{n,q}(x) = \sum_l \sum_r U_r e^{i(l+r)Gx} c_{l,n,q} \tag{2.28}$$

For an optical lattice, the potential can be expressed as

$$V(x) = V_0 \sin^2(\pi x/d) = V_0/2 - V_0/4e^{iGx} - V_0/4e^{-iGx} \tag{2.29}$$

From this, one can see that there are only 3 non-zero terms in Eq. (2.26), which are $U_{0,n,q} = V_0/2$ and $U_{1,n,q} = U_{-1,n,q} = V_0/2$. Using these expressions into Eq. (2.24) allows the Schrödinger equation to be written in matrix form as

$$H_{l,l'} c_{l,n,q} = E_{n,q} c_{l,n,q} \tag{2.30}$$

where $H_{l,l'}$ is an l by l tridiagonal matrix with the terms

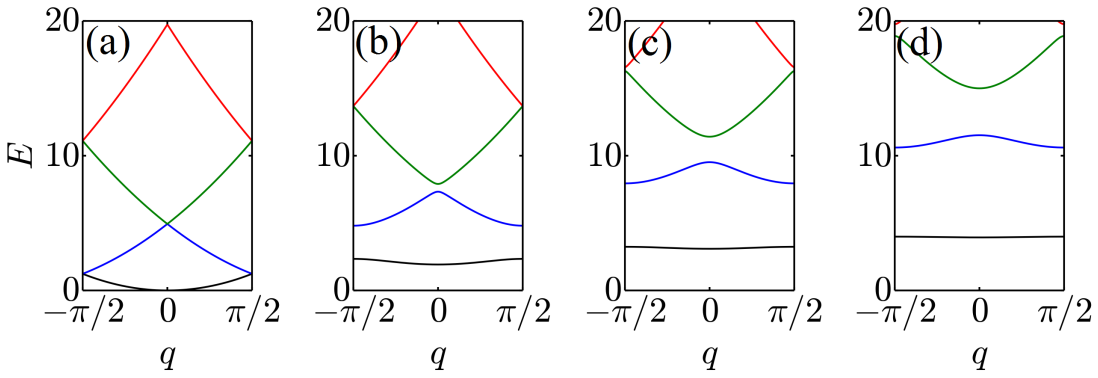

FIGURE 2.1: Plot of energy band structure of an optical lattice with (a)$V_0 = 0$, (b)$V_0 = 5$, (c)$V_0 = 10$ and (d)$V_0 = 15$. The energies of the Bloch bands $E_{n,q}$ are plotted against quasimomentum q in the first Brillouin zone (from $-\pi/2$ to $\pi/2$ in our normalisation) for different band numbers n.

$$H_{l,l'} = \begin{cases} \frac{1}{2}\left(q + lG\right)^2 + \frac{V_0}{2}, & \text{if } l = l' \\ -\frac{V_0}{4}, & \text{if } |l - l'| = 1 \\ 0, & \text{otherwise} \end{cases} \tag{2.31}$$

For a given value of q, the eigenvalues of $H_{l,l'}$ give the eigenenergies $E_{n,q}$ in the nth energy band. Solving this numerically allows the eigenenergies to be plotted against q. The lowest energy bands are plotted in Fig. 2.1 for different values of potential depth V_0. For $V_0 = 0$ (i.e. no lattice), there are no gaps between the energy bands as the particle is "free". As V_0 is increased, the size of the band gaps increases and the size of the energy bands decreases.

2.3.2 Localisation of BECs in Optical Lattices: the Continuous Model

With an optical lattice, bright solitons can be formed in both repulsive and attractive BECs. In this thesis, only repulsive atom-atom interactions are used (i.e.

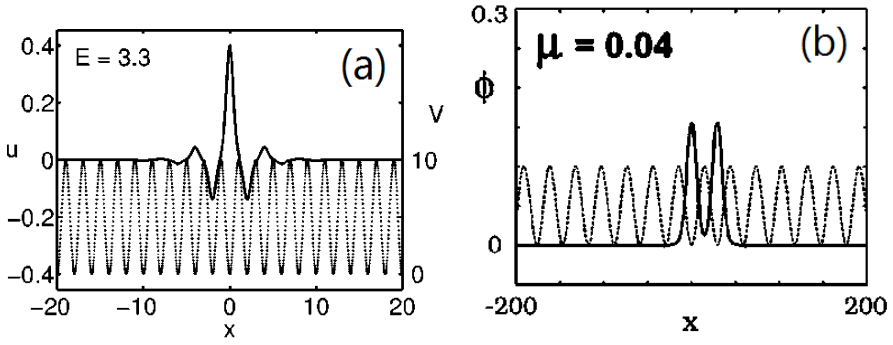

FIGURE 2.2: Examples of lattice soliton solutions found in the first bandgap (ie between the first two bands) of the energy-band structure. (a) is taken from [11], and (b) is taken from [10]. In (b), μ represents the frequency and ϕ the wavefunction of the BEC, with the different normalisations from [10].

$\beta > 0$). In the case of optical lattices, solitons can exist with energies in the band gaps shown in Fig. 2.1. For this reason, they are referred to as "gap solitons" in the literature. In this thesis, the more general term, "lattice solitons", is used for cases of localised modes in the GP equation (continuous model). Time oscillating solutions of Eq.(2.20) at frequency E are of the form $u(x)\exp(-iEt)$. Examples of this type of solution, found in [11] and [10], are shown in Fig. 2.2. It should be noted that the solutions presented in Fig. 2.2 represent the real components at $t = 0$. The real and imaginary components of the solutions oscillate with frequency E, while the density distribution should remain constant. The spatial amplitude $u(x)$ can be obtained from the equation

$$Eu = \left[-\frac{1}{2}\frac{\partial^2}{\partial x^2} + V_0 \sin^2\left(\frac{\pi x}{2}\right) + \beta|u|^2\right] u \tag{2.32}$$

In the band gaps, if one imposes that $u(x)$ decreases exponentially at the boundaries, or ends, of the lattice, the lattice soliton solutions can be obtained numerically via a simple relaxation method.

With an added momentum, lattice solitons can travel across the lattice. In [29], it was shown that as long as the soliton does not have an amplitude that is above a

critical value, it can move freely across the lattice. An approximation of a moving lattice soliton in the repulsive case was given in [29] as:

$$u(x) \quad = \quad 1.291 \quad A \exp\left[i\frac{p(x-c)}{2}\right] \cos\left[\frac{\pi(x-c)}{2}\right] \operatorname{sech}\left[\frac{A(x-c)}{2}\right] \quad (2.33)$$

with A as the amplitude, p the momentum and c the location of the centre of the soliton.

2.4 Discrete Model: The Discrete Nonlinear Schrödinger Equation

Another model often used to describe BECs in optical lattices is the discrete nonlinear Schrödinger equation (DNLSE), which is valid if the potential wells are deep and well-separated. It is assumed that the wavefunctions are well confined into the potential minima and only the first energy band is considered. The following *ansatz* [30] can be used in the GP equation:

$$\Psi = \sum_n \psi_n(T)\phi(\vec{r} - \vec{r}_n)\,, \quad (2.34)$$

where ϕ is an on-site wavefunction and $\vec{r}_n$ is the location of the n-th lattice site. When the atomic interactions are weak, the on-site ground state wavefunction can be replaced by the ground state harmonic oscillator wavefunction in the off-axis direction and a Wannier function [31] of the lowest band in the axial direction to account for tunneling. Consequently, $|\psi_n(T)|^2$ may be interpreted as the number of atoms in the n-th lattice site as a function of time and $\sum_n |\psi_n|^2 = N$.

Substituting the *ansatz* (Eq. 2.34) into the GP equation (Eq. 2.5) and dropping all terms mixing different lattice sites except for the ones that describe tunneling between neighbouring sites (see [30]), one obtains

$$i\hbar\dot{\psi}_n = -J\left(\psi_{n-1} + \psi_{n+1}\right) + \left(\lambda|\psi_n|^2 + \epsilon_n\right)\psi_n \tag{2.35}$$

where $J = \int \mathrm{d}^3\vec{r}\phi(\vec{r} - \vec{r}_n)\left(\frac{-\hbar^2}{2m}\nabla^2 + V\right)\phi(\vec{r} - \vec{r}_{n+1})$ is the hopping integral describing the tunneling of the atoms and is proportional to the intersite tunneling rate $\gamma = J/\hbar$, while $\epsilon_n = \int \mathrm{d}^3\vec{r}\phi(\vec{r} - \vec{r}_n)\left(\frac{-\hbar^2}{2m}\nabla^2 + V\right)\phi(\vec{r} - \vec{r}_n)$ is the on-site chemical potential, and $\lambda = g\int \mathrm{d}^3\vec{r}|\phi(\vec{r})|^4$ describes the atom-atom interaction.

A scaled model for use in simulations can be found by defining:

$$z_n = \sqrt{\frac{1}{N}}\psi_n^* \exp\left(-i\frac{\epsilon\tau}{\hbar\gamma}\right) \tag{2.36}$$

$$\tau = \gamma T \tag{2.37}$$

to obtain:

$$i\frac{d}{d\tau}z_n = \Lambda|z_n|^2 z_n - \left(z_{n-1} + z_{n+1}\right)\,, \tag{2.38}$$

which is known as the one-dimensional Discrete Nonlinear Schrödinger (DNLS) equation, where

$$\Lambda = \frac{\lambda N}{\hbar\gamma}\,. \tag{2.39}$$

Here the atomic distribution over the lattice is normalized to unity:

$$\sum_n |z_n|^2 = 1\,. \tag{2.40}$$

2.4.1 Discrete Breathers in DNLS

Self-localisation also occurs in the discrete model. The discrete counterpart of lattice solitons are known as discrete breathers. They have the name "breather" due to the oscillation of the real and imaginary parts, which also occur in the continuous lattice solitons, as discussed earlier. In the literature, there are two methods of forming these that are relevant to this thesis. One of which is evolution from an initially Gaussian wavepacket [30] of the form

$$z_n = \sqrt{\frac{1}{\sqrt{2\pi\sigma^2}}} \exp\left(-\frac{(n-\bar{n})^2}{4\sigma^2}\right) \quad e^{ipn} \tag{2.41}$$

where σ is the width, p the momentum and $\bar{n}$ the centre site of the wavepacket. Other initial conditions that are sufficiently close to a localised solution would also work. For example, in [32], initial conditions of all atoms placed in one site evolve towards breather states. In this thesis, just the Gaussian wavepacket is used.

Since a breather has exponential rather than Gaussian tails, during the reshaping process, atoms are expelled from the wavepacket, sometimes creating a noisy background.

This was investigated in [30], in which the dynamical phase diagram was studied. Three different regimes were found characterised by the values of the momentum p and nonlinearity Λ of the wavepacket: the diffusive regime, in which the wavepacket spreads across the lattice, the self-trapping regime, where the wavepacket stays localised, and one in which moving breathers are formed which travel along the lattice. Very different results have been obtained in [33] and a new dynamical phase diagram was obtained in [34]. Nonetheless, for wavepackets with large initial widths σ, one of the boundaries between the regimes in [30]

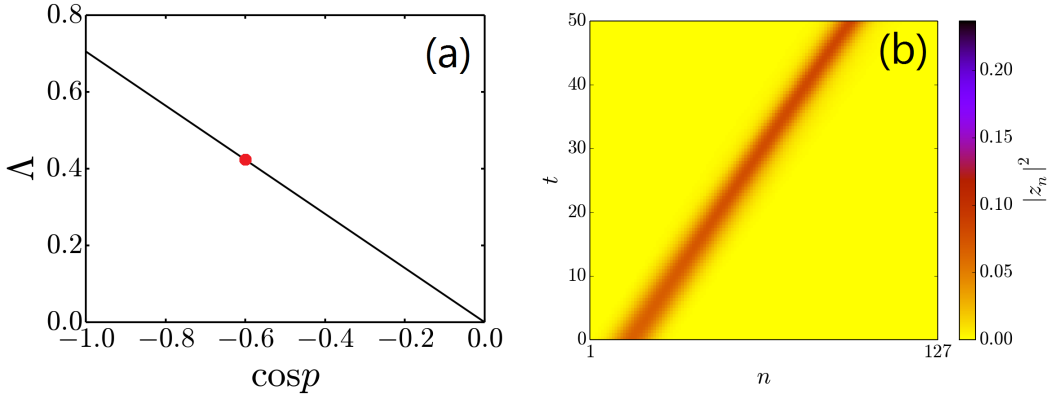

FIGURE 2.3: (a) Plot of Λ_s for $\sigma = 5$, as defined in Eq. (2.42). This is the relation between nonlinearity Λ and momentum p which gives a travelling breather that loses almost no energy in its reshaping process. An example of this is shown in (b), with $\Lambda = 0.423$ and $\cos p = -0.6$ (represented by the red dot in (a)).

was found to give mobile breathers that lose almost no energy when reshaping from the initial Gaussian [33]. This is when the nonlinearity and momentum are related like so:

$$\Lambda_s = -\frac{2\sqrt{\pi}}{\sigma} \exp\left(-\frac{1}{2\sigma^2}\right) \cos p \tag{2.42}$$

This line is plotted in Fig. 2.3 for $\sigma = 5$, along with an example of a moving breather formed with this relation. It is seen that since the reshaping is minimal, the resulting breather has a very small background.

One way of removing or cleaning up the backgound is by applying atomic dissipations at the boundaries of the lattice, as in [35] and [33]. For a lattice with M sites, the DNLS with boundary dissipations is given as:

$$i\frac{d}{d\tau}z_n = \Lambda|z_n|^2 z_n - (z_{n-1} + z_{n+1}) - i\gamma z_n(\delta_{n,1} + \delta_{n,M}) \tag{2.43}$$

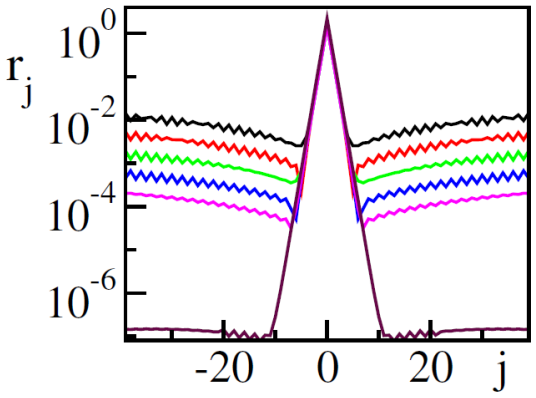

FIGURE 2.4: Example of discrete breather formed from an initial condition of a Gaussian wavepacket, taken from [33], showing amplitude r_j at site j. The wavepacket evolves according to Eq. 2.43. The top five lines show the evolution of a Gaussian wavepacket without dissipation and show the density profile at times, from top to bottom, 100 (black), 200 (red), 400 (green), 800 (blue) and 1600 (purple). The line at the bottom of the image shows the density profile at time 80000 with dissipation acting on the lattice boundaries, in this case at $j = \pm 4000$

where γ is the dissipation rate which acts on sites 1 and M. Localised dissipation has been demonstrated experimentally in [93] in which an electron beam was used. In that experiment, the electron beam was pointed at a specific site to remove atoms from it.[1]

In the case of Eq. 2.43, with stationary breathers generated from Gaussian wavepackets, the mass that is shed from the initial wavepacket is removed at the boundaries so that it does not stay in the background [33]. With the breather far away from the dissipations, the effect of the losses gets less with time as the system progresses towards a clean breather solution. See for example Fig. 2.4, taken from [33], in which a breather is shown to survive for long time-scales while dissipation is still acting on the lattice. The breather is not removed by the dissipation because it is far away from the boundaries that the dissipation acts on.

[1] An investigation of using this localised dissipation to produce localised structures for attractive BECs in an optical lattice was presented in [94]. In this thesis, we focus on repulsive BECs.

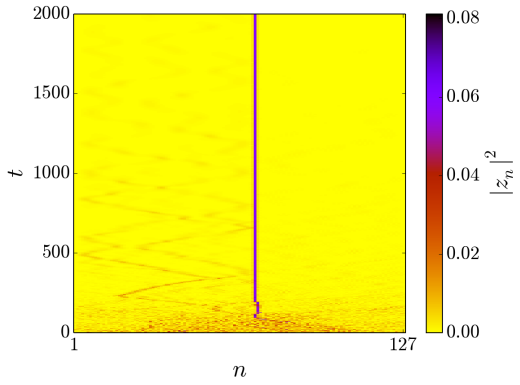

FIGURE 2.5: Example of discrete breather formed from boundary dissipation. Initially, all sites have the same amplitude with phases randomly distributed between 0 and 2π. After a transient time of 500 time-steps (not shown), dissipation is turned on at $\tau = 0$. The nonlinearity is set to $\Lambda = 80$ and the dissipation rate at the boundaries is given by $\gamma = 0.8$

For travelling breathers, the dissipation should be placed at the site in the lattice furthest from the breather. In this case, the dissipation site will change as the breather moves along the lattice. This has a similar effect to the stationary breather in that the background is lowered due to this.

Breathers have also been shown to be formed when applying dissipation to random distributions or initially flat condensates with random phase variables [33, 35]. Both stationary and mobile breathers have been shown to form from this. An example is shown in Fig. 2.5. Here we can see the formation of a stationary breather from this method. In this example, a travelling localized structure with a lower density peak also forms to the left of the stationary one. This is eventually removed by the dissipation and the final solution is a single stationary breather.

Chapter 3

Effect of Local Dissipations on Stationary and Travelling Lattice Solitons in Ring Bose-Einstein Condensates

3.1 Continuous Model with Localized Dissipations

The situation investigated in this chapter is that of a BEC in an optical lattice in a one-dimensional ring trap, as realised for example in [36–39] (see Fig. 3.1(a)). Experimentally, a ring optical lattice can be achieved by superposing two counter-rotating orbital angular momentum beams, creating an "optical ferris wheel" [36] or by using counter-propagating laser beams in a circular wave-guide.

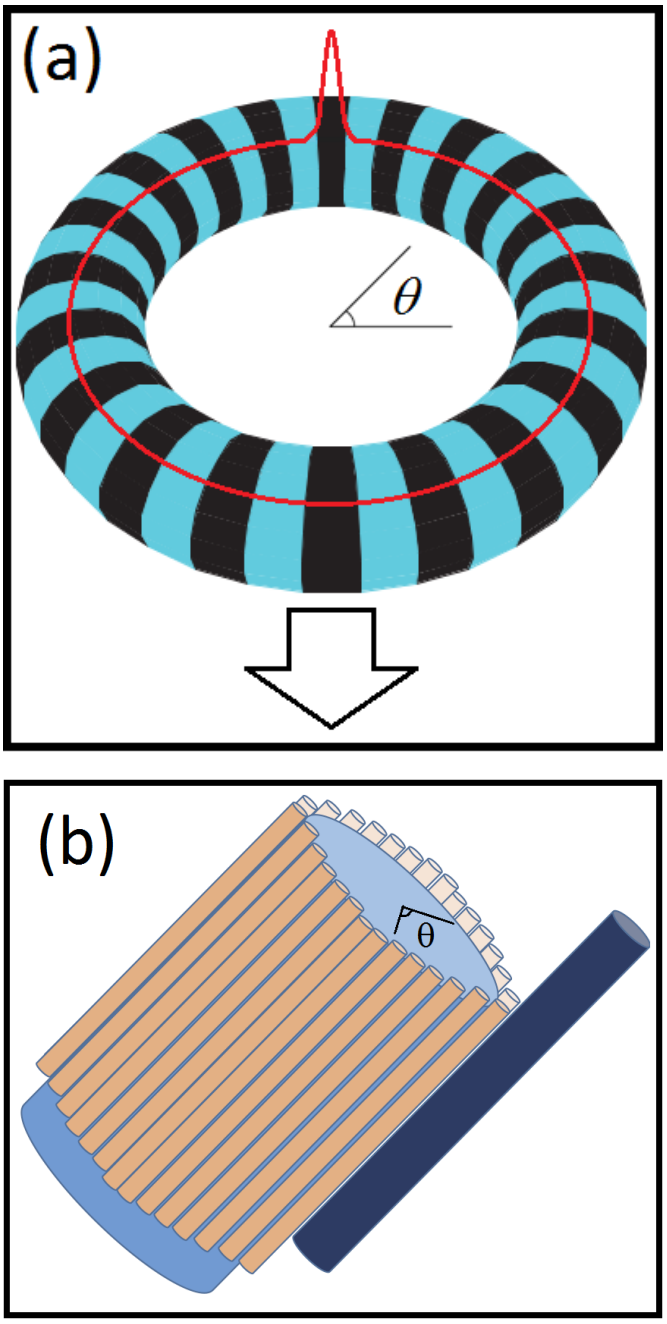

FIGURE 3.1: (a) BEC lattice soliton in an optical lattice ring-trap. The arrow identifies the position where localized losses are applied. (b) An array of optical waveguides in a ring configuration. The dark cylinder represents an output coupler capable of removing light from the array.

As said in the introduction, many of the results in this thesis can be extended to the purely optical case of light travelling through arrays of optical waveguides.

The equivalent case in nonlinear optics to the ring lattices is a cylindrical array of optical waveguides (see Fig. 3.1(b)).

For this chapter, the scaled values introduced in Section 2.3 are used, as in Eq. 2.20. In the case of a ring lattice, the length scale x is changed to that of the ring angle $\theta = 2\pi x/ML$ ranging from 0 to 2π radians, with M being the number of potential wells in the ring along the azimuthal direction. Using this in Eq. 2.20 gives the following expression:

$$i\frac{\partial u(\theta,t)}{\partial t} = \left(-\frac{\pi^2}{2M^2}\frac{\partial^2}{\partial\theta^2} + V_0\sin^2\left(\frac{M\theta}{2}\right) + \beta|u|^2 - i\rho(\theta)\right)u\,, \tag{3.1}$$

with the term $\rho(\theta)$ added to account for the loss due to atomic dissipation, which has been used in the discrete case to generate breathers or lower the background [35]. As said in Chapter 2, extremely precise methods for removing atoms in a particular position of a BEC in optical lattices have been implemented with the use of narrow electron beams [93]. The intensity of such electron beams can control the number of atoms that are removed from one or more potential wells of the optical lattice. In our examples, the dissipation is applied at the furthest point in the ring (i.e. an angular distance of π radians) from the intensity peak of the lattice soliton. For example, with the stationary solitons that are generally generated at $\theta = \pi$, the dissipation is applied at $\theta = 0 = 2\pi$. In the optical case (see Fig. 3.1(b)), the equation is the same but the time variable t is replaced by the propagation variable z.

Equation 3.1 is normalised so that at $t = 0$, before any atoms are lost due to dissipation,

$$\int |u(t=0)|^2 d\theta = 1\,. \tag{3.2}$$

The chapter is structured as follows. In Section 3.2, the generation of stationary lattice solitons (SLS) as well as the effect of dissipation on them is detailed and compared to solutions found by other numerical methods in [10, 11]. Travelling lattice solitons (TLS) are generated and investigated in Section 3.3. Finally, collisions between travelling and stationary lattice solitons in a ring trap are investigated in Section 3.4 while collisions between two travelling lattice solitons are studied in 3.5.

3.2 Lattice Solitons with Stationary Localized Dissipations

As discussed in chapter 2, it has been shown in the DNLS that stationary and moving breathers can be formed from initially Gaussian wavepackets [30, 33]. For the model in this chapter, the following general form is used:

$$u = \frac{M^2}{\gamma^{1/2}\pi^{9/4}} \exp\left\{\left(-\frac{(\theta-\theta_c)^2}{2\gamma^2}\right)\right\} \tag{3.3}$$

with θ_c being the position of the centre of the wave-packet and γ the width. With the nonlinear coefficient fixed at $\beta = 1$, the initial width was changed and several localised solutions were found in the case of zero losses (i.e. the conservative case).

Typically, the Gaussian wavepacket would reshape into a solitonic shape. The atomic mass expelled from the wavepacket forms a noisy backround. The peak fluctuates in height as it interacts with the background. As the width is increased, the background becomes more "noisy", sometimes with a smaller amplitude "soliton" appearing close to the main one. The small amplitude peaks however do

not survive in the long term. A typical example of this, with $\gamma = 1$, is shown in Fig. 3.2. The profile of the solution is shown in Fig. 3.2(a), with the localised peak in the centre and a noisy background, and the fluctuation of the peak is shown in (b). Due to the fluctuation of the height and noisy background, this is not technically a soliton because the shape is not perfectly preserved. Nonetheless, the localised peak survives for very long time scales. The example shown in Fig. 3.2 still maintains its average height by $t = 1000000$. When the width of the initial Gaussian condition is too large, no soliton is formed and the condensate disperses on the background. Similarly, if the width is too small (smaller than a single potential well), there is no self-localisation either.

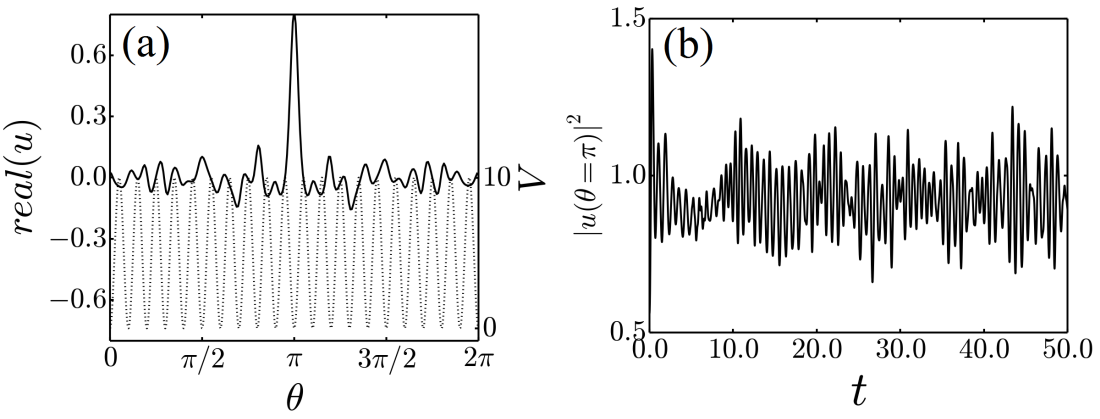

FIGURE 3.2: (a) Localised mode formed from initital Gaussian wavepacket with $\gamma = 1$ and with no dissipations. The dotted line is the lattice V with $V_0 = 10$ (see scale on right). The peak oscillates as it interacts with the nonvanishing background. The oscillation of the central peak is shown in (b)

With dissipation applied to the above situation, we get less noisy backgrounds, since the mass expelled from the packet escapes at the location of the losses. In all the examples in this section, the dissipation acts on ~ 4 potential wells with the maximum loss 0.5 at $\theta = 0 = 2\pi$. Here, we find much more stable soliton solutions, many of which are very similar to that shown in [11] but found with very different numerical methods. In Fig. 3.3, an SLS generated from a Gaussian

of unit width ($\gamma = 1$) is presented. An image of a similar soliton solution from [11] was shown in Fig. 2.2(b).

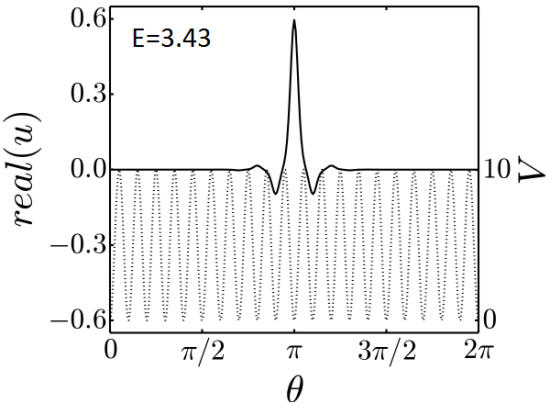

FIGURE 3.3: Stationary lattice soliton formed from applying dissipation to an initially Gaussian wavepacket. The dotted line is the lattice V with $V_0 = 10$ (see scale on right). The shape of the soliton is very similar to ones shown in [11], one of which was presented in Fig. 2.2(a).

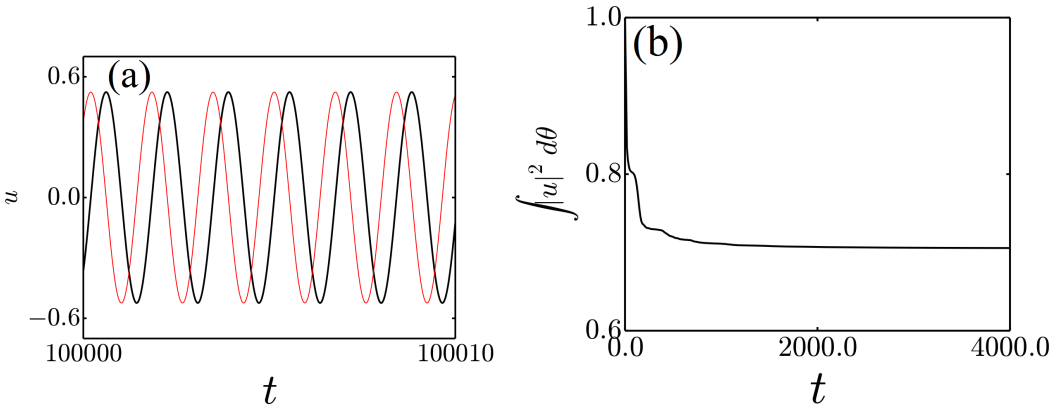

FIGURE 3.4: (a) Real (black) and imaginary (red) parts of peak of SLS $u(x = \pi)$ against time. Oscillations are sinusoidal with frequency E and a $\pi/2$ phase difference so that $u(x,t) = u(x)\exp(-iEt)$. (b) Atomic density of u against time with dissipation. The atomic density decreases until the effects of dissipation are negligible.

This SLS is of the usual form $u(x,t) = u(x)\exp(-iET)$, with the real and imaginary parts sinusoidally oscillating, or "breathing", with frequency E. This is shown in Fig. 3.4(a), with the real and imaginary parts oscillate with a phase

difference of $\pi/2$ (i.e. sine and cosine). This is the continuous analog to the results in the discrete model [33, 35], in which solutions of the conservative system are produced via dissipation. A reason for this is shown in Fig. 3.4(b), in which the total density $\int |u|^2 d\theta$ is plotted against time t. Here, it is shown that, after decreasing as expected initially, the atomic density eventually becomes constant so that the effect of the dissipation is negligible. This is because the density at the area where the dissipation acts on (in this case ~ 4 potential wells around $\theta = 0 = \pi$) has been removed, and, with $\rho(x)u \approx 0$, Eq. (3.1) is virtually the conservative GP equation.

The effect of dissipation on the soliton and background can be seen clearly in Fig. 3.5, which shows the decay of the backround leading to the typical exponential tails associated with lattice solitons. In the larger lattice, this effect is less obvious, due to the distance from the dissipation to the soliton (see Fig. 3.5 (b)). Making the dissipation broader so that it acts on most of the potential wells in the lattice (in this case ~ 150 out of 160) can help to reveal the SLS tails faster (see green line in Fig. 3.5 (b)).

The eventual shape and frequency of the soliton is affected by changing the initial width of the Gaussian γ: the wider the Gaussian, the more atoms are lost due to dissipation and the lower the final peak amplitude of the resulting lattice soliton. The frequency of the oscillations of the real/imaginary parts of the solitons, along with the gradient of the exponential tails of the soliton, is larger if the number of atoms (or peak amplitude) is larger. For example, the soliton from [11] in Fig. 3.3(b) has a smaller frequency than the soliton in Fig. 3.3(a) and thus has a smaller peak amplitude. The peak intensity, gradient and frequency of lattice soliton generated from Gaussians of various widths with localised dissipations are presented in Table 3.1.

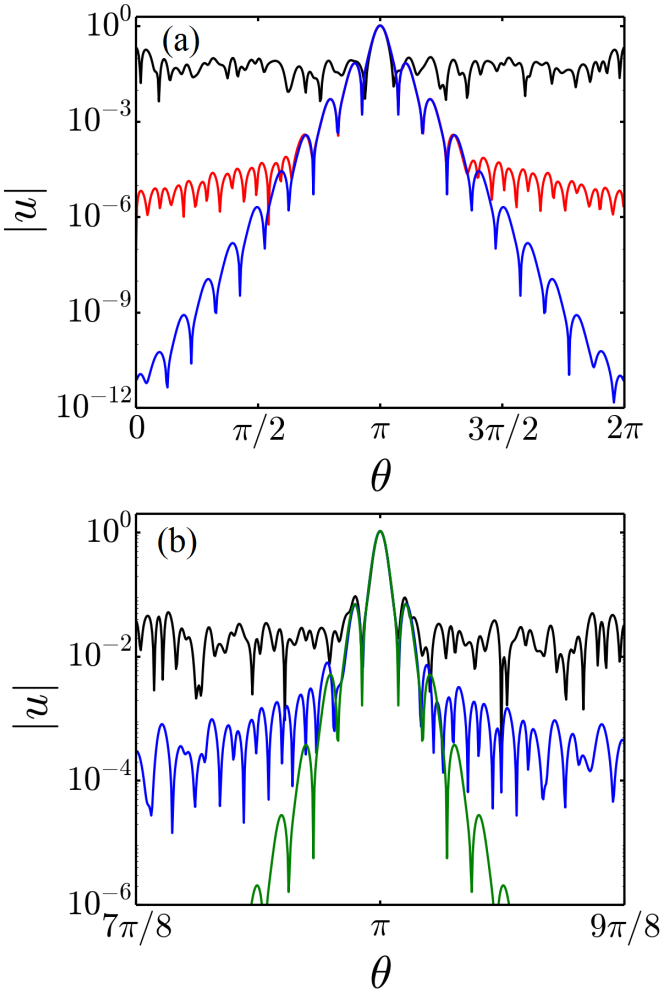

FIGURE 3.5: Intensity distribution of stationary lattice solitons obtained from initial single Gaussian wavepackets with localised dissipation to get rid of excess noise. The curves correspond to t=0 (black), t=20000 (red), and t=100000 (blue) in a lattice of 20 potential wells (a) and 160 potential wells(b). Time t=0 is the point at which dissipation is turned on. In (b), we also show the intensity distribution after increasing the number of potential wells where the dissipation acts on from $\sim$ 4 to $\sim$ 150 at t = 100000 and then running the simulation for another 100000 time units (green).

Sometimes, different types of soliton solutions are formed. For example, with $\gamma = 1.3$ and $\gamma = 1.8$, the result is that of asymmetric lattice solitons with two high-peaks next to each other. An example is shown in Fig. 3.6, with $\gamma = 1.3$. The intensity of each peak oscillates, as is shown in Fig. 3.6(b). The oscillations of the real/imaginary parts of each of the two peaks have different frequencies -

TABLE 3.1: Values of parameters used in the simulations

γ	Peak Intensity	Gradient of tails	Frequency	Nature of Solution
0.5	1.258	0.420	4.05	SLS
0.7	1.167	0.410	3.97	SLS
0.9	1.012	0.398	3.89	SLS
1.0	0.923	0.392	3.83	SLS
1.2	0.765	0.367	3.72	SLS
1.3	0.651	0.355	3.62	QLS
1.6	0.539	0.332	3.55	SLS
1.8	0.377	0.289	3.46	QLS
2.0	0.362	0.287	3.43	SLS

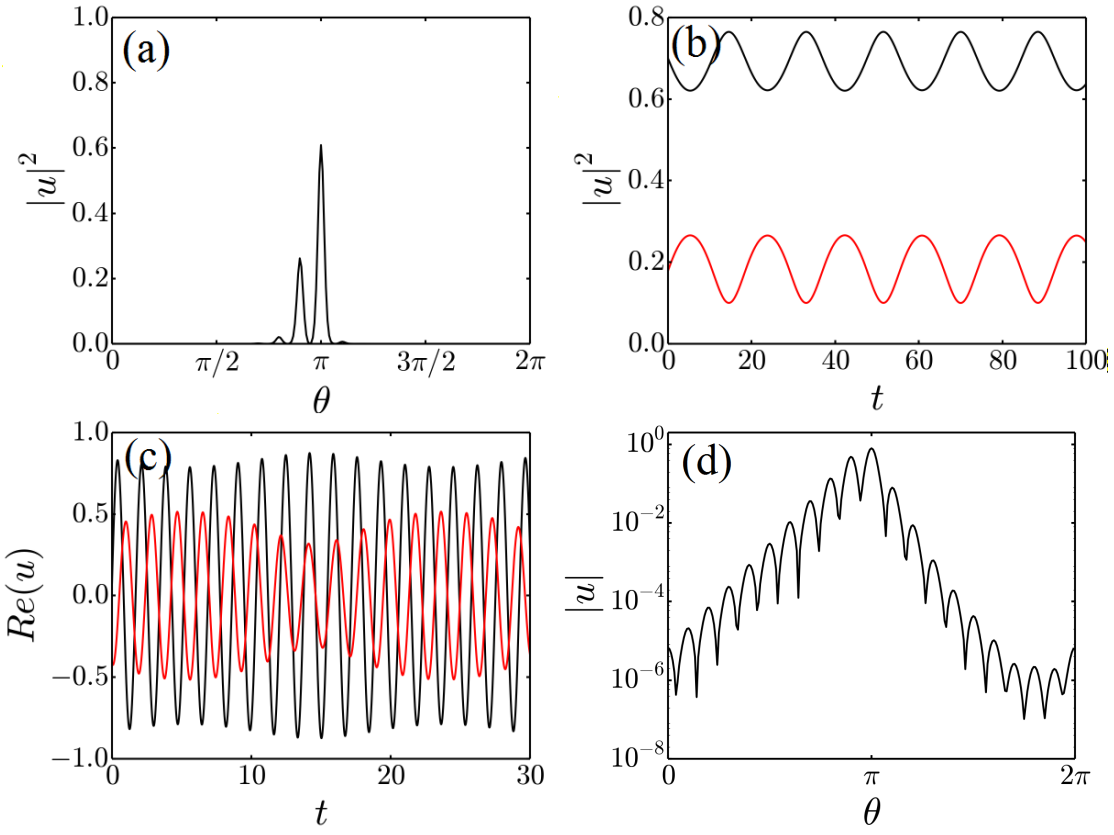

FIGURE 3.6: (a) Quasiperiodic lattice soliton generated by applying dissipation to an initial Gaussian with width $\gamma = 1.3$. (b) Variation in time of intensity of smaller peak (red line) and larger peak (black line). (c)Variation in time of real part of peak of larger amplitiude (black line) and smaller amplitude (red line). (d) Logarithmic plot of same solution in (a).

the oscillations of the real part of each peak is plotted in Fig. 3.6(c). As well as this, the gradients of the exponential tails on each side are also different. This is shown in Fig. 3.6(d), with the logarithmic plot of the same solution. The values of peak intensity, frequency and gradient of the tails of the quasiperiodic lattice solitons (QLS) in Table 3.1 are those associated with the highest peak in each case. Note that this is similar to the quasiperiodic discrete breathers obtained in the DNLSE (see [40]).

Another type of solution, shown in Fig. 3.7, is a symmetric one with two main peaks (as in [10]). The two peaks are in-phase with each other, oscillating at the same frequency, as opposed to the previous quasiperiodic example in Fig. 3.6. This lattice soliton has been found by using localized dissipations and by shifting the initial wavepacket by $L/2$ (half a potential well). This is the equivalent of using a potential of $V = V_0 \cos^2(M\theta/2)$ (rather than $V = V_0 \sin^2(M\theta/2)$) so that the initial gaussian wavepacket is centered between two potential wells. The nonlinearity is set to a higher value of $\beta = 10$, corresponding to a higher number of atoms or a larger scattering length. With $\beta = 1$, the double peak relaxes to the single peak solution quickly.

Another initial condition that can be used in analogy with what has been done in the DNLSE (see [33, 35] and the example in Fig. 2.5) is that of a homogenous distribution of atoms across the optical lattice with random phases. In the example shown in Fig. 3.8, the code runs a transient without dissipations for 1000 time-steps. After this, dissipation is turned on. There is a first localisation to two peaks, (see Fig. 3.9(a)). The amplitudes of the peaks fluctuate and eventually, at long time scales (around $t = 35000$), the peak on the left moves closer to the other so that only one potential well separates them (see Fig. 3.9(b)). To observe this behaviour, the nonlinearity has been increased to $\beta = 50$.

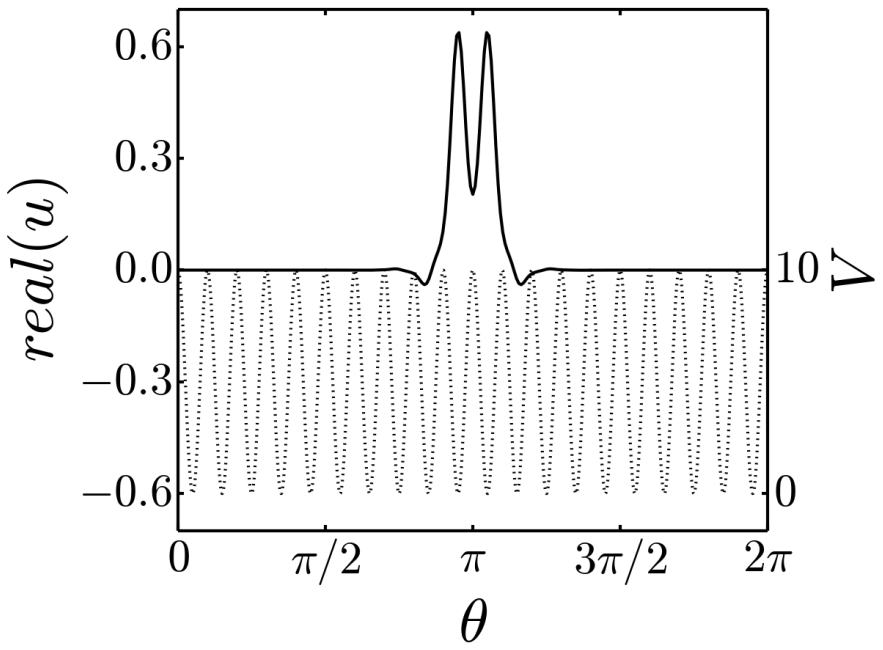

FIGURE 3.7: A higher order soliton solution with two peaks, similar to one shown in Fig. 2.2(b) from [10]

3.3 Lattice Solitons with Traveling Localized Dissipations

As discussed earlier, in the discrete model, traveling breathers have been shown to be formed from initially Gaussian wavepackets with an additional momentum [30, 33, 34]. To replicate this in the continuous case and stabilise a travelling lattice soliton (TLS), an initial distribution made of a "Gaussian of Gaussians" is used (see Fig. 3.10 (a)). In the DNLSE where each potential well corresponds to a single lattice point, this distribution would reduce to a normal Gaussian shape (see dashed line in Fig. 3.10 (a)). Since this is the continuous model, each of these points is represented by a Gaussian in each potential well. With the addition of an initial momentum p (here set to $\cos(p) = -0.95$), a travelling peak is formed in the continuous model. Dissipation is applied to this at the point in the ring furthest away from this, similar to what is described in [33]

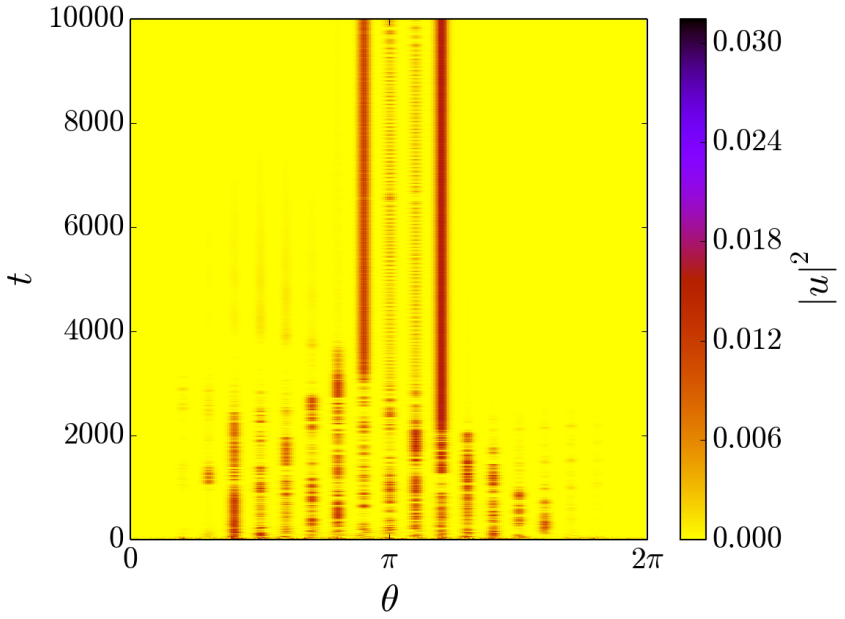

FIGURE 3.8: Space-time evolution of atomic density $u(x,t)$ with $\Lambda = 50$ and dissipations set so the maximum loss is 0.5. The initial condition is that of a "flat" equal amplitude wavefunction with random phases.

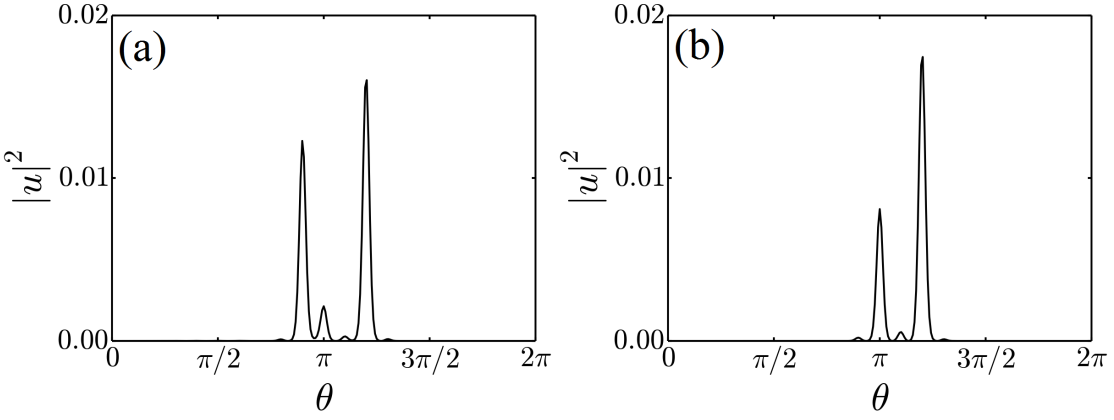

FIGURE 3.9: Intensity distribution of localised solution obtained from applying dissipation to an initially flat wavefunction at $t = 10000$ (a) and $t = 100000$ (b).

for the DNLSE. Since the atomic density peak is travelling, the point at which dissipation is applied moves too.

In the example shown in Figures 3.10 and 3.11, we have $\beta = 1.0$, $V_0 = 10$,

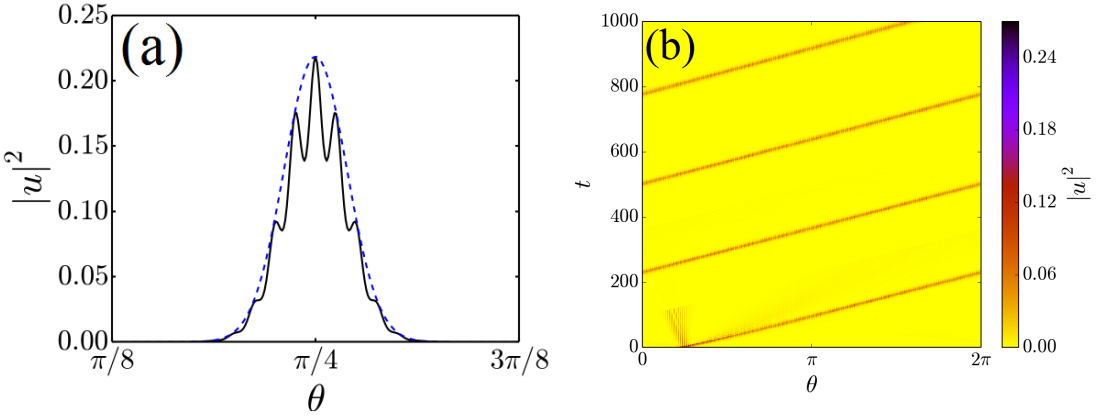

FIGURE 3.10: (a) Initial condition of TLS. Note that this would be an ordinary Gaussian shape in the discrete model (shown by the blue dashed line) (b) Space-time evolution of atomic density $u(x,t)$ of TLS with $\beta = 1$.

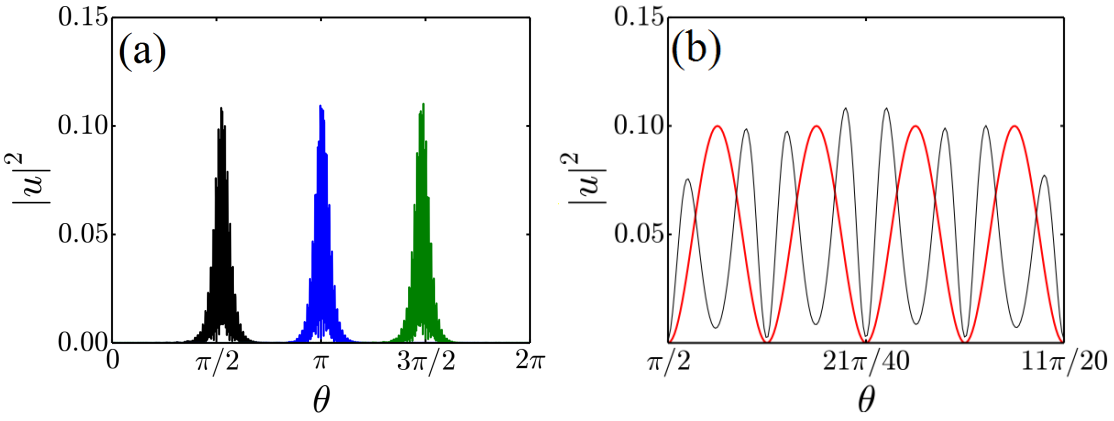

FIGURE 3.11: (a) Intensity distribution of TLS at $t = 10150$ (black), $t = 10220$ (blue) and $t = 10290$ (b) Close-up of intensity distribution at $t = 10150$ (black, thin) with the periodic potential (red, thick), showing the two peaks-per-potential well.

and $\cos(p) = -0.95$ and dissipations given by $\rho = 0.5$ over 4 lattice wells. At the beginning of the simulation, a certain amount of atoms remain stationary after the travelling peak is formed. This can be seen in Fig. 3.10 (b), with the high amplitude stationary part of the wavefunction visible until $t \approx 100$, when these atoms are removed due to the moving dissipation. At long time scales, the peak shapes into a TLS and travels at a constant speed (shown in Fig. 3.11(a)). Without the dissipation, the atoms that do not travel with the moving peak

eventually spread across the lattice, giving a larger background noise. As the moving peak travels and interacts with the background, it gets smaller in height as it loses atoms to the background. By $t \approx 1600$, the height has decreased by half. In contrast, with the dissipation the TLS survives to longer time scales, still at the same height by $t \approx 40,000$. The fact that dissipation helps instead of hinders the formation of a TLS is even more surprising since, at difference with the stationary lattice solitons, TLS require the presence of a background in order to overcome the unavoidable Peierls-Nabarro barriers [33, 41][1]. The presence of the localized dissipation is then twofold: on one side it removes enough stationary background noise to help with the localization of the TLS and on the other it moves with the traveling background thus maintaining it to the level necessary for the motion and stability of the TLS.

Using the same initial condition shown in Fig. 3.10(a), simulations were run for different values of potential depth V_0. For each of the values of V_0, a different TLS is formed, with a different peak amplitude, width and speed. What is found is that, for lower values of V_0, the resulting TLS is smaller in height, larger in width and travels with a higher velocity. The opposite is true for higher values of V_0. The values of peak intensity, full width at half maximum (FWHM) and velocity (measured in number of potential wells per unit t) of the TLSs found are shown in Table 3.2.

The TLSs formed from this are "higher-order" ones, with two peaks per potential well (see Fig. 3.11(b)). Due to this shape, they have no equivalent solution in the discrete model.

If dissipations are turned off after a certain amount of time (in the examples here, they are turned off at $t \approx 20000$), the background noise begins to grow again and

[1]The Peierls-Nabarro barrier is an effective potential generated by the discreteness of the lattice and can be interpreted as the energy needed for the localised modes to travel.

TABLE 3.2: Attributes of TLSs with two peaks per potential well found for different values of V_0

V_0	Peak Intensity	FWHM/potential wells	Velocity/potential wells per unit t
7.0	0.043	13.4	0.711
7.5	0.055	11.5	0.703
8.0	0.070	10.1	0.688
8.5	0.083	7.50	0.656
9.0	0.095	6.56	0.625
9.5	0.106	5.47	0.582
10.0	0.114	0.547	0.547

the TLS either slows to a halt or is absorbed into the background. In the example in Fig. 3.12, with $\beta = 1.0$, $V_0 = 11$, and $\cos(p) = -0.95$, the TLS slows to a halt. When stationary, there is a break in symmetry of the two peaks (Fig. 3.12(a)), with one gradually becoming bigger than the other until there is only one peak in the central potential well (Fig. 3.12(b)). This process takes place over a timescale of $t \approx 7000$.

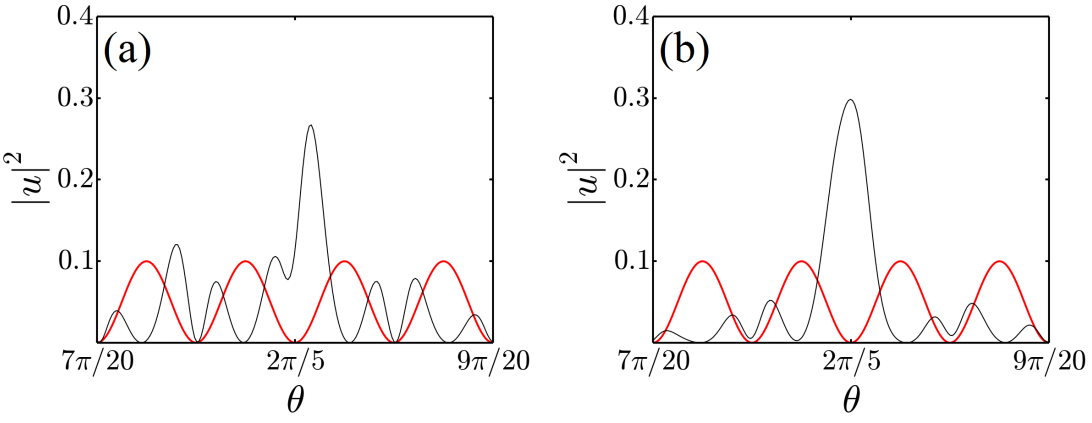

FIGURE 3.12: Intensity distribution (black, thin) of TLS slowed to a halt with periodic potential (red,thick). At $t = 17000$ (a) the symmetry of the two peaks is broken, with one much bigger than the other. At $t = 20000$ there is only one peak in the central potential well.

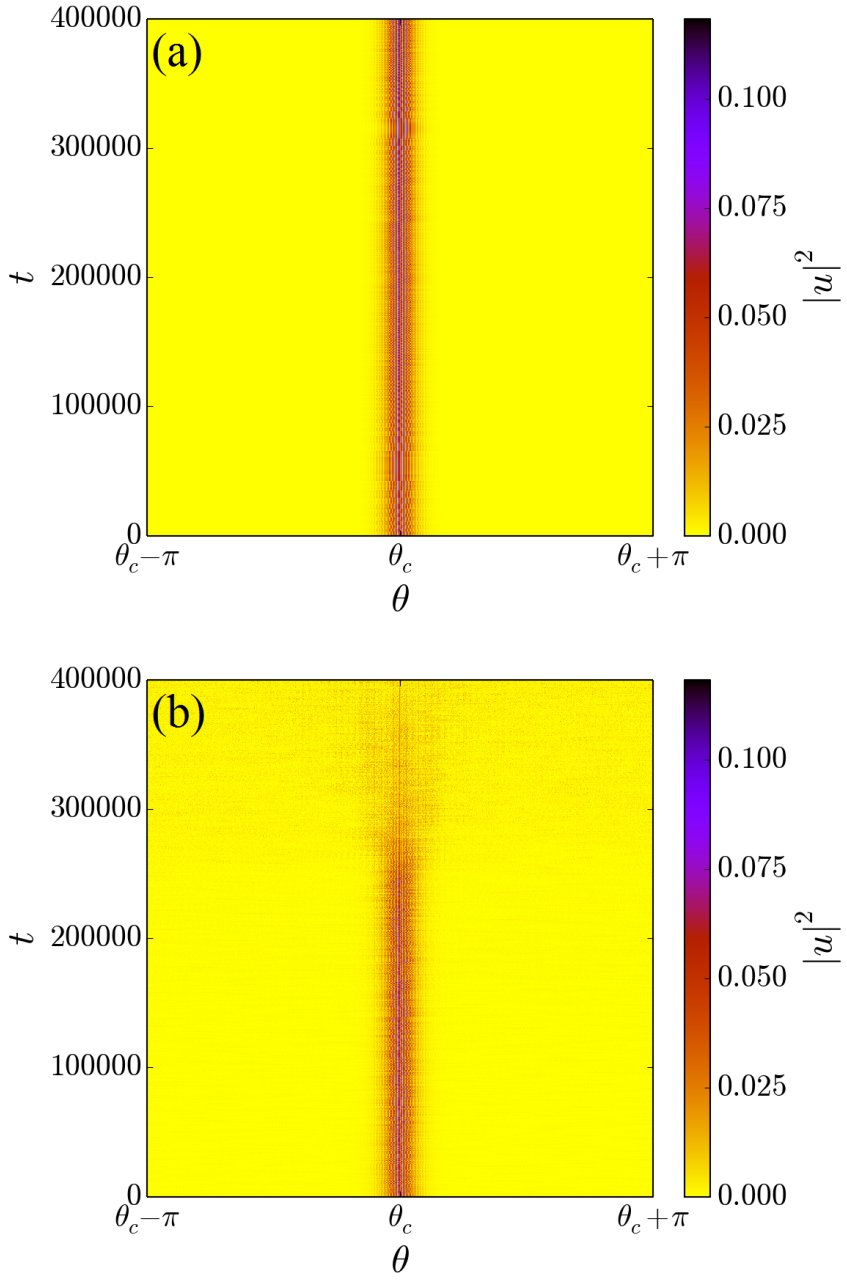

FIGURE 3.13: Temporal evolution of the intensity distribution of the TLS initiated via (3.4) for the case with localized, moving dissipations ($\rho = -0.4$) (a) and without dissipations ($\rho = 0$) (b). Note that TLS is traveling along the ring but each distribution has been shifted so to have the TLS maximum at the same angular location).

An approximate form of the amplitude of the TLS displayed in Fig. 3.10 and Fig. 3.11 can be used as initial condition at time $t = 0$ and is given by

$$\begin{aligned} u(\theta) &= -7.66 \; A \exp\left[i\frac{pM(\theta-\pi)}{2\pi}\right] \\ &\quad \sin\left[M(\theta-\pi)\right] \operatorname{sech}\left[AM(\theta-\pi)\right] \end{aligned} \tag{3.4}$$

where A is a parameter that depends on the width of the TLS. For $A = 1/(7.5\pi)$ and $p = -0.4$ we obtain a fit of the TLS in Fig. 3.11 as accurate as few percent. Having determined the approximate TLS shape in Eq. (3.4), one can use it as an initial condition for the formation of the double peak TLS in the presence or absence of dissipations. With dissipations $\rho = 0.5$, it is verified that the TLS of Fig. 3.11 forms much faster when using the wavepacket (3.4) as the initial condition instead of the Gaussian wavepacket. Figure 3.13 (a) shows that this TLS survives for extremely long time scales with an extremely small loss of atomic density or energy. The steady loss due to dissipation is so small that after one million time units, the atomic density only decreases by 0.21%. This is similar to what happens to the stationary lattice solitons in Section 3.2 when boundary losses approached irrelevance at the tails of the lattice soliton.

Without localized dissipations, a traveling peak starting from (3.4) survives for a long time (see Fig. 3.13 (b)). However, in the absence of dissipations, the background noise eventually grows and absorbs the peak as shown in the last stages of Fig. 3.13(b). These features demonstrate that localized dissipations are necessary for both the formation and the stability of the double peak TLS when starting from wavepacket distributions of atoms in the lattice with a given momentum.

Localized traveling dissipation can be applied to TLS with one peak per potential well by using the analytical approximation of [29]

$$u(\theta) = 8.11\ A \exp\left[i\frac{pM(\theta-\pi)}{2\pi}\right] \cos\left[\frac{M(\theta-\pi)}{2}\right] \operatorname{sech}\left[AM(\theta-\pi)\right] \tag{3.5}$$

with A and p being the amplitude and the momentum of the TLS respectively. These parameters are set to $A = 0.3/(2\pi)$ and $p = -0.5$ and the amplitude of the initial condition (3.5) and its temporal evolution in the ring are shown in Fig. 3.14 (a) and (b), respectively. It is important to note that with or without dissipation, the inital condition (3.5) quickly develops a noisy background on which the TLS travels while remaining well approximated by (3.5) in the potential wells where atomic localization takes place. The dissipation clears up stationary noise, but does not destroy the TLS with one peak per potential well. The atomic density is only slightly affected by the dissipation, which decreases by $\sim 0.12\%$ after one million time units, even slower than the higher-order TLS.

As with the double-peaked TLSs, different TLSs with one peak per potential well can be found with different values of V_0. The values of peak intensity, full width at half maximum (FWHM) and velocity of these TLSs found are shown in Table 3.3. As with the double-peaked TLSs, for higher (lower) values of the potential depth, the TLS is smaller (larger) in height, larger (smaller) in width and has a higher (smaller) velocity. The single-peaked TLSs are larger in height and travel at much smaller (over ten times) velocities than the equivalent double-peaked TLSs with the same potential depth.

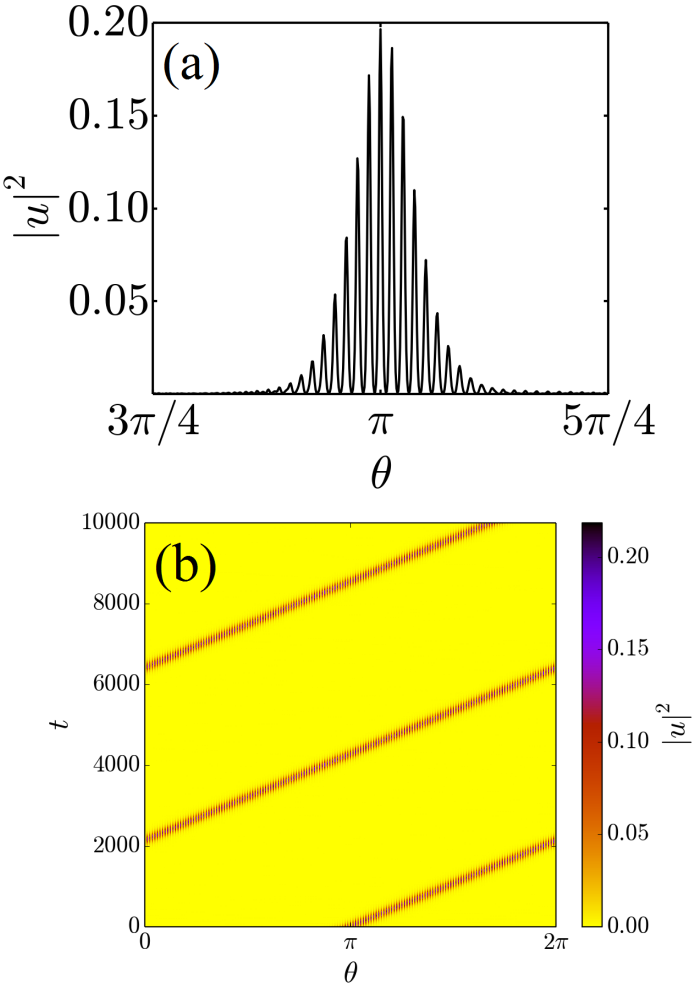

FIGURE 3.14: (a) Initial condition of TLS with one peak per potential well. (b) Space-time evolution of atomic density $u(x,t)$ of this TLS with $\beta = 0.04$.

3.4 Collisions of Travelling and Stationary Lattice Solitons

In this section, the collisions of SLSs and TLSs with two peaks per potential well are investigated. The SLSs are generated with the same method as the ones in Section 3.2. The height of the soliton is varied by changing the width γ of the initial Gaussian. The amount of atoms that pass through the SLS is dependent on its height. The TLS used is the one generated for $V_0 = 10$.

TABLE 3.3: Attributes of TLSs with one peak per potential well found for different values of V_0

V_0	Peak Intensity	FWHM/potential wells	Velocity/potential wells per unit t
9.0	0.147	6.09	0.0469
9.5	0.164	6.09	0.0414
10.0	0.195	5.08	0.0375
10.5	0.223	4.14	0.0336
11.0	0.243	4.14	0.0305

The temporal evolution of the atomic density of both lattice solitons at successive collisions in the ring is shown in Fig. 3.15 for zero dissipation. In both examples in this figure, the TLS starts at $\theta \approx \pi/2$ and the SLS is placed at $\theta \approx 3\pi/2$, which is as far apart from each other as possible in the ring. The amount of atomic density that passes through the stationary lattice soliton at each collision is determined by its height. The higher the stationary lattice soliton, the less atomic density passes through, as shown in the examples of Fig. 3.15. When the amplitude of the SLS is low (≈ 0.45, shown in Fig. 3.15 (a)), the majority of the atomic density in the TLS passes through the SLS at the point of collision ($t \approx 150$), with only a small amount being reflected. Every time there is a collision, the atomic density that is reflected interferes with the TLS that had passed through the SLS previously. This makes the TLS weaker and weaker as time goes on. When the amplitude of the SLS is high (≈ 0.95 in Fig. 3.15 (a)), the majority of the atoms in the TLS reflect off of the stationary one while a small amount tunnels through. The small amount of atoms that tunnel through seem to have no major effect on the TLS, which manages to survive longer than in the previous example.

In the discrete model, collisions between a stationary and travelling breather were investigated in [42]. In that paper, the travelling breather survives bouncing off of the stationary one multiple times, similar to our example in Fig. 3.15(b).

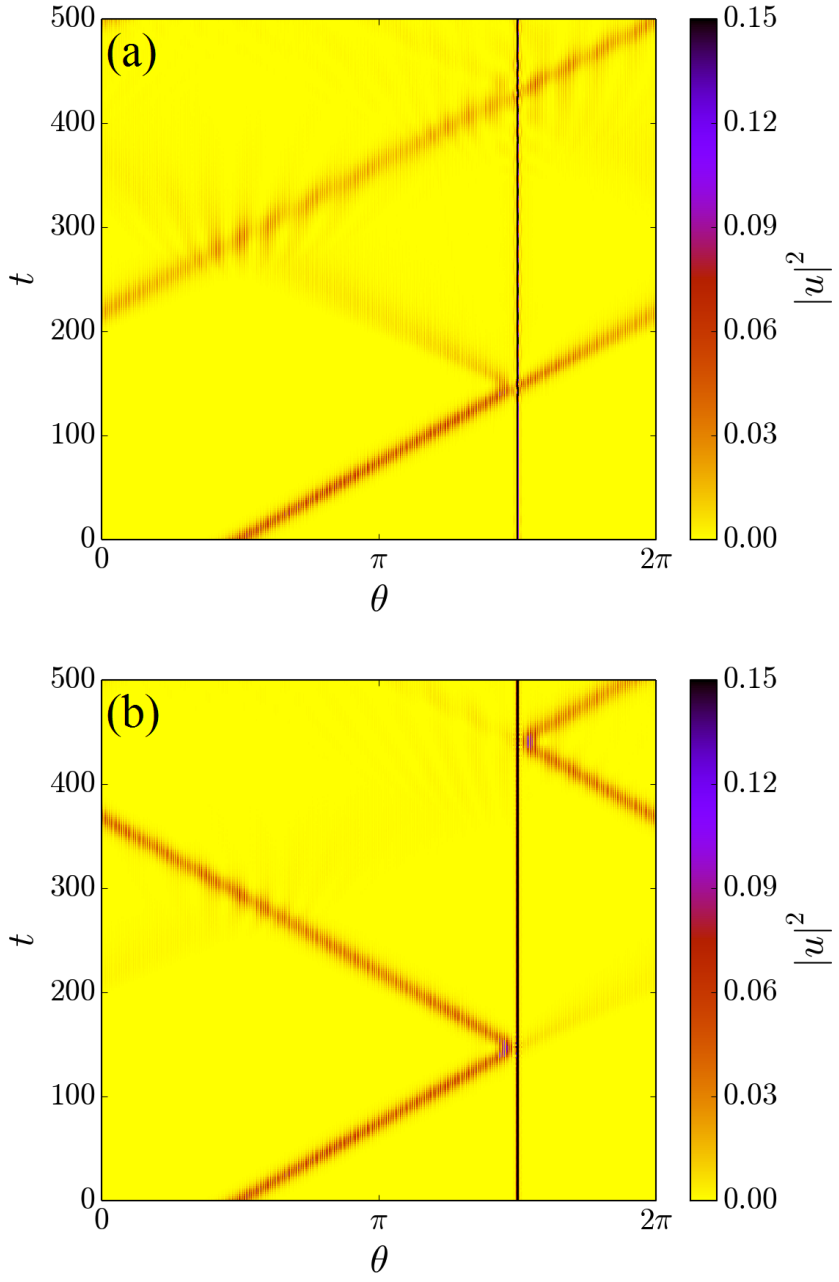

FIGURE 3.15: TLS colliding with SLS with amplitude ≈ 0.45 (a) and ≈ 0.95 (b). Note that although the intensity of the SLS is the scale for the intensity only goes up to 0.15, even though the intensity of the SLS is ≈ 0.45 in (a) and ≈ 0.95 in (b). This was done to show the TLS in more detail.

3.5 Collisions of Travelling Lattice Solitons

Here, the collisions of two TLSs circling in the ring are investigated. In the first example, in Fig. 3.16, the TLS with two peaks per potential well as described in Section 3.3 and with $\beta = 1$ and $V_0 = 10$ is used. Two identical TLSs are positioned at opposite sides of the ring ($\approx \pi$ radians apart), are made to travel in the opposite directions ($p = 0.5$ and $p = -0.5$, respectively) and then collide. Since dissipations would interfere with the process of collisons, dissipations are set to $\rho = 0$ for both TLS. As demonstrated in Fig. 3.13 (b), the TLS with no dissipations survives for a long time during which more than a hundred collisions can take place. Here, the first couple of collisions are focused on to establish the nature of the interaction of the TLS at short distances and for interferometric properties. The collision from the two TLS results in two seemingly identical TLS at the output (see Fig. 3.16 (a)).

In order to find out if the TLS have gone through one another or have reflected each other, the wavefunction can be split in two by substituting $u = u_1 + u_2$, where u_1 represents the atoms of one TLS and u_2 in the other, into Eq. (3.1) to get:

$$\begin{aligned} i\frac{\partial u_1(\theta,t)}{\partial t} &= \left(-\frac{\pi^2}{2M^2}\frac{\partial^2}{\partial\theta^2} + V_0\sin^2\left(\frac{M\theta}{2}\right) + \beta|u_1+u_2|^2\right)u_1 \\ i\frac{\partial u_2(\theta,t)}{\partial t} &= \left(-\frac{\pi^2}{2M^2}\frac{\partial^2}{\partial\theta^2} + V_0\sin^2\left(\frac{M\theta}{2}\right) + \beta|u_1+u_2|^2\right)u_2 \end{aligned} \tag{3.6}$$

It is found that, when the TLSs collide, some of the atomic density from each TLS passes through the other while the remaining part is reflected. When this happens, the reflected atomic density of each TLS merges with the transmitted part of the other one. This happens in such a way that the two TLS that result

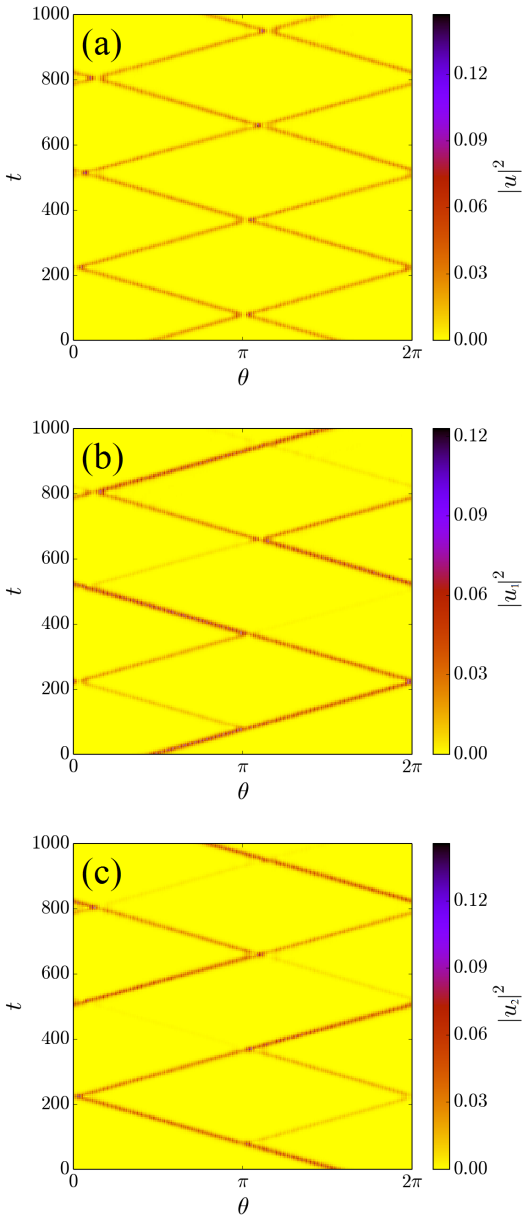

FIGURE 3.16: Collision of "double-peaked" TLSs. The total density profile of the collisions is shown in (a) while the density profile of the atoms from each initial TLS is plotted in (b) and (c).

from the collision have approximately the same shape as the original ones, despite containing a mixture of the atomic density from each of them. The results of the numerical simulations of Eqs. (3.6) reproduce exactly those of the simulations of Eq. (3.1) when cosidering $u = u_1 + u_2$. In this particular example, $\sim 79.5\%$ of

the atomic density of each TLS passes through the other one at each collision. The evolution of the atomic density distributions of each initial TLS are plotted in Fig. 3.16 (b) and (c) respectively, showing how each TLS splits at each collision. The transmitted/reflected fractions of atomic density of the two TLS in the collisions does not change when starting the collision process from a different intial lcoation of the TLS. However, these fractions change with the depth of the lattice potential as reported in Table 3.4.

TABLE 3.4: Percentage of atomic density reflected and transmitted in collisions between 2 TLS with two peaks per potential well

V_0	reflection	transmission
7.0	11.8	88.4
7.5	12.6	87.4
8.0	13.7	86.3
8.5	15.1	85.0
9.0	16.8	83.2
9.5	18.6	81.5
10.0	20.4	79.6

Similar results of collisons occurs with the TLS with just one peak per potential well. In Fig. 3.17, collisions of these TLS for $V_0 = 10$ and $\beta = 0.041$ are shown. Again, the TLS "swap" atomic density at each collision, with the shape of the resulting TLS largely unchanged. Here, $\sim 77.0\%$ of the atomic density in each TLS stay with the "original" one at each collision, while the rest join the other ones. Table 3.5 shows the dependence of the transmitted/reflected fractions of atomic density in the collisions of TLS with a single peak per potential well when changing the depth of the optical lattice.

Similar collisions of discrete breathers in the DNLS equation were investigated in [42]. In this case, the lattice was not a ring lattice and the boundaries were reflective. However, like here, the localised structures were allowed to collide repeatedly and the result of each collision was two identical breathers. Whether

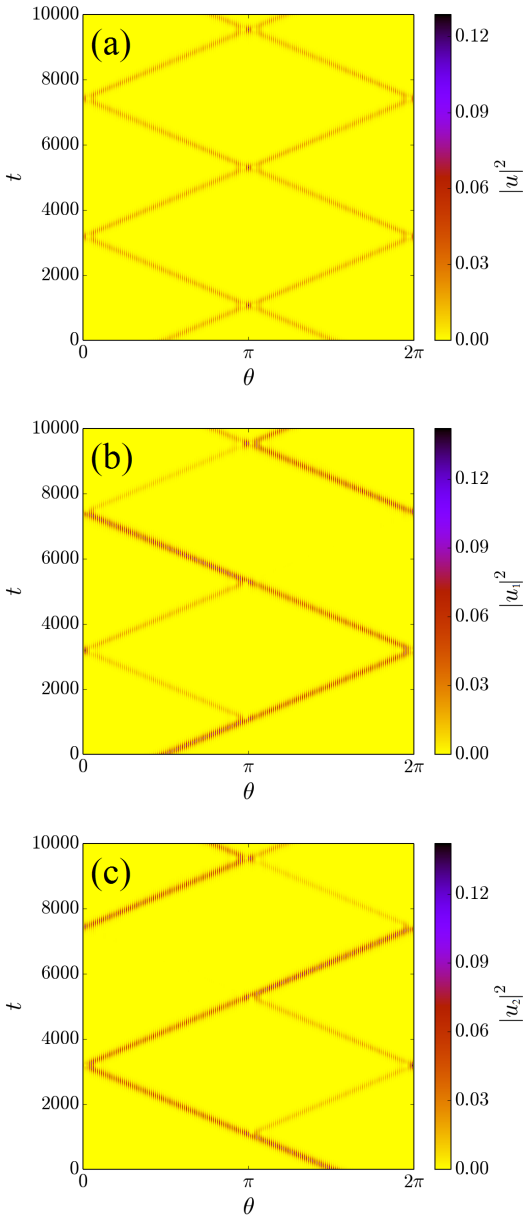

FIGURE 3.17: Collision of the normal "single-peaked" TLSs. The total density profile of the collisions is shown in (a) while the density profile of the atoms from each initial TLS is plotted in (b) and (c).

the breathers passed through each other or reflected off of one another was not investigated.

TABLE 3.5: Percentage of atomic density reflected and transmitted in collisions between 2 TLS with one peak per potential well

V_0	reflection	transmission
9.0	14.7	85.3
9.5	18.3	81.7
10.0	23.0	77.0
10.5	29.5	70.5
11.0	38.2	61.8

3.6 Conclusions

The effect of local dissipation on a BEC in a ring lattice was studied. It was found that the dissipation can both generate and stabilize stationary and traveling lattice sollitons. A TLS with two intensity peaks per potential well was introduced that does not have a counterpart in the DNLSE. This can be generated, via an initial Gaussian wavepacket (as in the discrete model) with dissipation. This does not survive without losses in the long term, either being absorbed by the background or slowing to a halt. Collisions of this TLS with different SLSs were shown and it was found that the interaction and survival of the TLS depends on the amplitude of the SLS. The collisions of two TLS in the ring was also analyzed. It was found that some of the atoms in each TLS merge with the colliding one while some are reflected in such a way that the shape of the resulting TLS' intensities stays the same. This collisional property depends on the potential depth of the lattice. The amount of atoms that are transmitted (reflected) during the collision is smaller (larger) in deeper lattices and larger (smaller) in shallower lattices.

A possible application of travelling solitons is interferometry. This was first suggested in [42] in the presence of optical lattices and with the DNLSE. The possibility of interferometry in the case of attractive BECs in a ring was proposed and investigated in [43–45], in which the solitons collided with potential barriers. In

the case of an optical lattice, collisions of TLSs with additional potential barriers is investigated in the next chapter.

Chapter 4

Reflections of Moving Lattice Solitons and Discrete Breathers off of a Potential Barrier

4.1 Model

This chapter considers the collision of travelling lattice solitons (TLSs) and discrete breathers (DB) with a Gaussian potential barrier. In Chapter 3, two types of TLS were studied: one with one intensity peak per potential well, defined in Eq. 3.5, and one with two, defined in Eq. 3.4. In this chapter, collisions of both of these in the continuous model, and of DBs in the discrete model, with a potential barrier are investigated. The potential barriers can be either positive (i.e. a potential wall) or negative (i.e. a potential well) relative to the lattice.

When colliding with a barrier, atoms can either be reflected, transmitted or trapped by the barrier. Without a lattice and with attractive BECs, it has been shown that it is possible to produce two outgoing solitons from collisions with

narrow barriers , similar to a beam splitter splitting the light of an optical interferometer [43, 46, 47]. In the case of a ring trap [43–45] or a harmonic trap [44, 48, 49] with a barrier, a Mach-Zehnder interferometer has been considered in which the outgoing solitons can recombine at the barrier. With negative barriers (i.e. potential wells), trapping can occur, as well as, counter-intuitively, reflection [50, 51].

Optical lattices allow for the use of repulsive BECs to sustain travelling solitons. With optical lattices and repulsive BECs, it has been shown that trapping of atoms can occur for barriers with a positive height [52]. This is because a negative effective mass soliton sees this barrier as a potential well rather than a wall. In the regime of a wide barrier in a shallow optical lattice, the amount of atoms reflected, transmitted and trapped by the barrier was measured against the height of the barrier in [52]. Repeated regions of reflection, transmission and trapping were found for positive heights of the barrier[1]. Similar results were found in the discrete model with a wide barrier and an attractive nonlinearity [53].

In this chapter, we investigate the situation of a ring lattice with a Gaussian potential barrier of the form

$$V_b = \alpha \exp\left(-\frac{(\theta-\pi)^2}{\gamma}\right), \tag{4.1}$$

with height α and width γ. We simulate the collisions of TLSs in the GPE and of discrete breathers in the DNLSE against a barrier of this form. The GPE model we use here is the same as that of Chapter 3 but with the extra Gaussian potential term:

[1]The same was also found for attractive lattice solitons with positive effective mass and for negative heights of the potential barrier in the same paper, but in this chapter we again only concentrate on repulsive BECs.

$$i\frac{\partial u(\theta,t)}{\partial t} = \left(-\frac{\pi^2}{2M^2}\frac{\partial^2}{\partial\theta^2} + V_0 sin^2\left(\frac{M\theta}{2}\right) + \alpha\exp\left(-\frac{(\theta-\pi)^2}{\gamma}\right) + \beta|u|^2\right)u\,. \tag{4.2}$$

Note that there is no dissipation used in the simulations in this chapter.

4.2 Collision of single-peaked TLSs with a potental barrier

First we investigate the collision of single-peaked TLSs, defined in Eq. 3.5 (from [29]), with the potential barrier V_b. Eq. 4.2 is numerically integrated for different values of the barrier height α. The atoms in the TLS can do one of three things as a result of the collision: bounce off the barrier (reflection), pass through the barrier (transmission) or be trapped in the barrier (trapping). The fraction of atoms that do each of these things is measured as R, T and S respectively. For a deep lattice ($V_0 = 10$) and thin barrier ($\gamma = 0.3$), R, T and S are plotted against barrier height α in Fig. 4.1.

For $\alpha = 0$ (i.e. when there is no barrier), $R = S = 0$ and all the atoms pass through as one would expect. Full reflections occur for higher magnitudes of α. An example of full reflection is shown in Fig. 4.2. When the TLS reflects off of the barrier, it keeps its shape and velocity afterwards. The density distribution of the TLS at $t = 0$ is shown in Fig. 4.2(a), while (b) shows the density distribution after the collision (at $t = 3850$). Comparing the two, it can be seen that the TLS keeps its shape after the collision. The evolution of the intensity in time, shown in Fig. 4.2(c), shows that the TLS survives for multiple collisions of the barrier, and that it does not change its velocity.

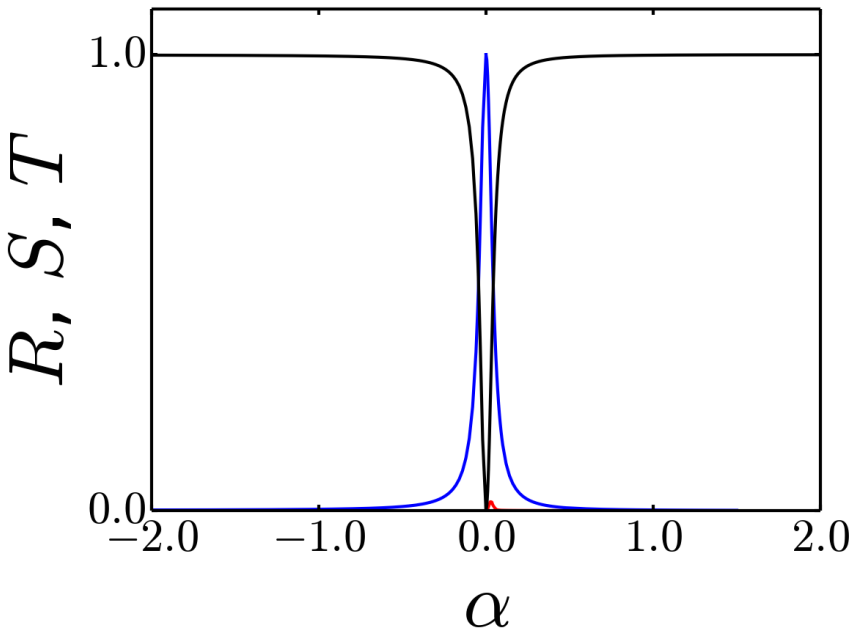

FIGURE 4.1: Ratio of atoms reflected (R, black line), transmitted (T, blue line) and trapped (S, red line) by Gaussian potential barrier V_b with height α.

From Fig. 4.1, it can be seen that, between the regions of total reflection or transmission, there are regions with partial reflection and transmission. For these regions, the TLSs "split" at the barrier, as in [43, 46, 47], forming two outgoing TLSs. In Fig. 4.3, the aftermath of collisions which result in partial reflection and transmission are shown. In the example with $\alpha = 0.035$ (Fig. 4.3(a)), the collision has resulted in two TLSs of different size, along with a small amount of trapped atoms at the barrier. Trapping of atoms only happens for positive values of α. As in [52], this is because of the TLSs negative effective mass. In Fig. 4.3(b), with $\alpha = -0.045$, we have a split in which the resulting two TLSs are around the same size, and there is no trapping since $\alpha < 0$.

Using a ring lattice allows us to consider a Mach-Zehnder interferometer, as in [43–45]. The time evolution of the example in Fig. 4.3(b) is shown in Fig. 4.4, in which the split TLSs are allowed to collide again at the barrier. Fig. 4.4 shows

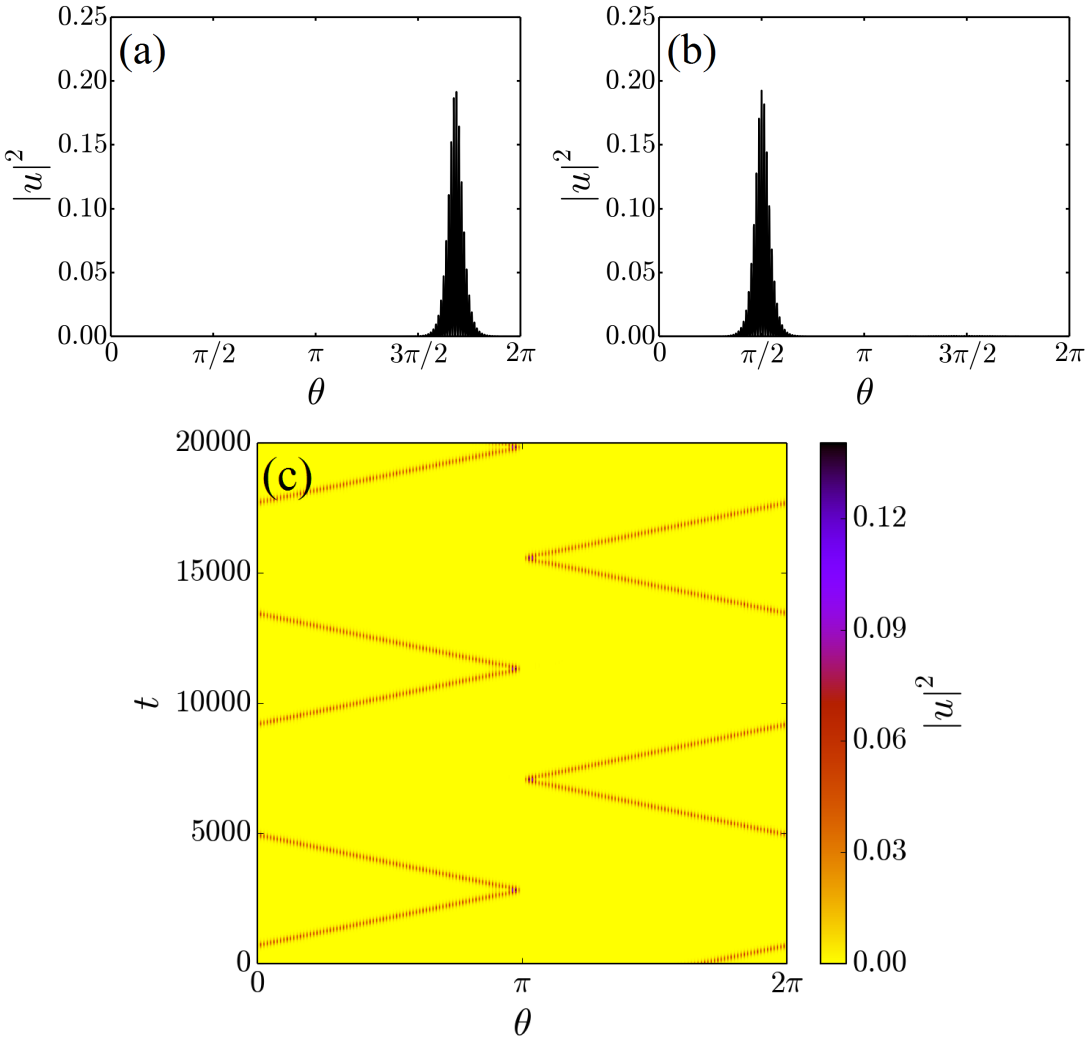

FIGURE 4.2: (a) Initial condition of TLS travelling in positive θ direction. (b) TLS after collision with barrier at $t = 3850$. Here, it is seen that the TLS has kept its shape after the collision. (c) Evolution of intensity distribution of same collision. Here, it can be seen that the TLS survives multiple collisions without changing velocity.

the time evolution of the example in Fig. 4.3(b). First, the TLS collides with the barrier at $\theta = \pi$ at $t \approx 2700$, splitting into two TLSs of approximately the same height. Then, the TLSs continue to travel in opposite directions around the ring, passing through each other at $\theta = 0 = 2\pi$ and $t \approx 5000$, and then colliding with the barrier again at $t \approx 7000$. At this second collision, the TLSs recombine,

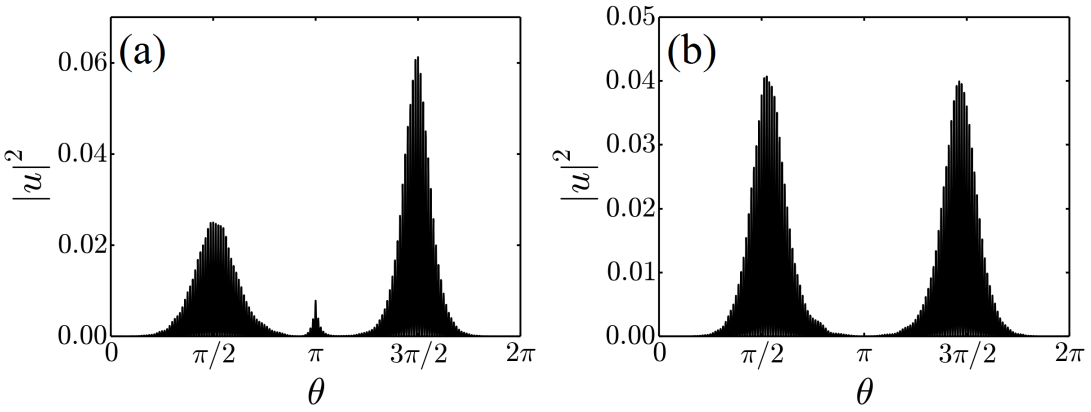

FIGURE 4.3: Results of collisions in which the TLS is split so that there is partial reflection and partial transmission. In (a), with a potential barrier of height $\alpha = 0.035$, the two resulting TLSs are of different size. Both TLSs are travelling away from the barrier so that the smaller one on the left is moving in a negative θ direction and the larger one on the right is moving in a positive θ direction. In the center, at $\theta = \pi$, there is a small amount of trapping, which is stationary. In (b), with $\alpha = -0.045$, the two resulting TLSs are of approximately the same size. Again, both are travelling away from the barrier. There is no trapping here, since $\alpha < 0$.

producing a single TLS travelling in the opposite direction from the original one. The TLSs lose atomic density to the background, so the resulting TLS from this is not as large as the original. As it travels around the ring, however, it does pick up more density from the background. This is shown in Fig. 4.4(b) and (c). In Fig. 4.4(b), the TLS is shown soon after the collision at $t = 8300$. The peak intensity is only ≈ 0.075, which is small compared to the original TLSs peak intensity of ≈ 0.2. By $t = 10100$ (in Fig. 4.4(c)), the peak has almost doubled in size.

For a shallower lattice of depth $V_0 = 2.5$, there are a few differences. The fraction of atoms reflected (R), transmitted (T) and trapped (S) by the potential barrier with various heights (α) is plotted in Fig. 4.5. As before, there is only trapping for positive values of α. For this shallower lattice, however, the amount of atoms that are trapped is much larger. The highest amount of atoms trapped is for $\alpha = 0.06$, which is shown in Fig. 4.6. A very large amount of atoms are trapped

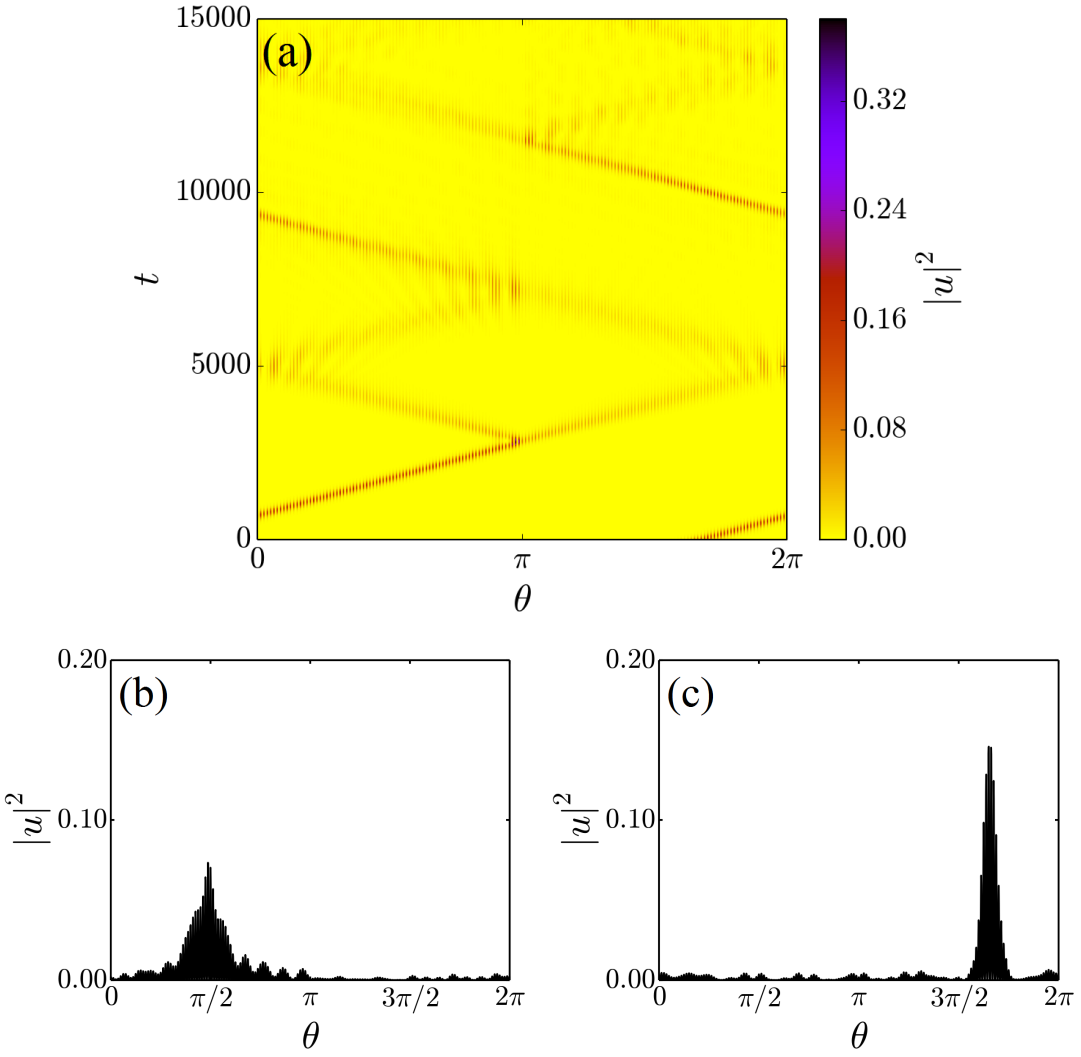

FIGURE 4.4: Multiple collisions with a barrier of height $\alpha = -0.045$. In (a), it is seen that the TLS splits in two at the first collision with the barrier. The two resulting TLSs are close to equal in size (distribution of this is shown in Fig. 4.3(b)) and pass through each other before colliding again and recombining at the barrier. In (b), is it seen that just after the collision, at $t = 8300$, that the TLS produced at the second collision is smaller than the original, with more background noise. It absorbs more density as it travels, becoming larger in height, as seen in (c), at $t = 10100$.

at the barrier during the collision. The TLS is trapped there for long time-scales, as seen in Fig. 4.6(a). Some atoms are released into the background, but most of the atoms remain with the TLS, as seen in Fig. 4.6(b), which shows the initial

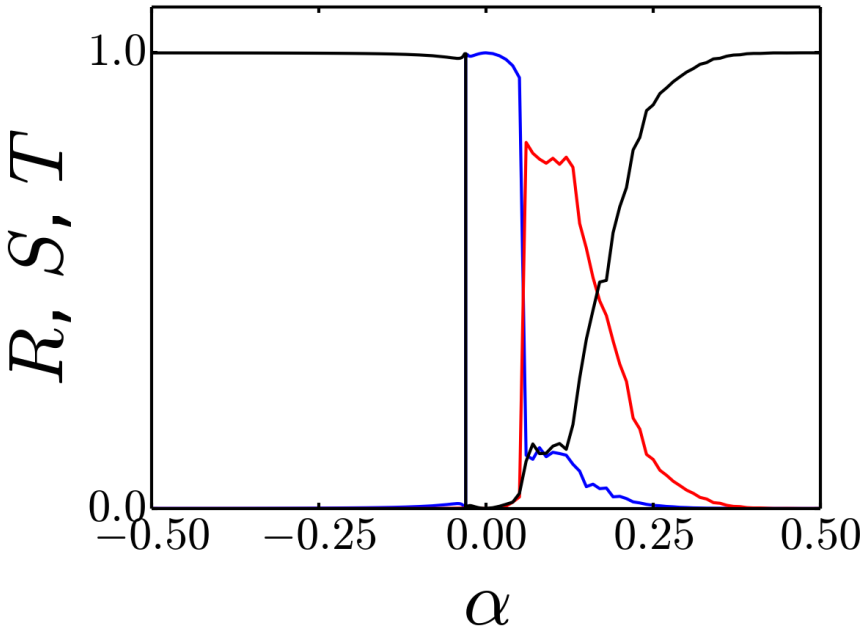

FIGURE 4.5: Fractions of atoms from TLS with one peak per potential well reflected by (R, black line), transmitted by (T, blue line) and stuck in (S, red line) a potential barrier with height α and $\gamma = 0.3$. Potential depth of optical lattice is $V_0 = 2.5$.

condition, and Fig. 4.6(c), which shows the TLS after it has been trapped for a long time.

For negative values of α, the collisions are much simpler, with the TLS completely (or mostly) transmitting the atoms for smaller values of α, and then completely (or mostly) reflecting after a "cutoff" value, rather than the smooth transition that is shown for the $V_0 = 10$ plot in Fig. 4.1. A possible reason for this is the higher nonlinearity of the TLS used for $V_0 = 2.5$ ($\beta = 0.59$), compared to the one for $V_0 = 10$ ($\beta = 0.04$). The higher nonlinearity could mean that the atoms are held together more strongly, making a split more difficult (as in [48] and [44]). As α approaches this value (from both sides), the TLS stays in the centre for a short amount of time before being reflected or transmitted. This is shown in Fig. 4.7, where the collision is shown for $\alpha = 0.03028$ (in (a)) and $\alpha = 0.03030$ (in (b)).

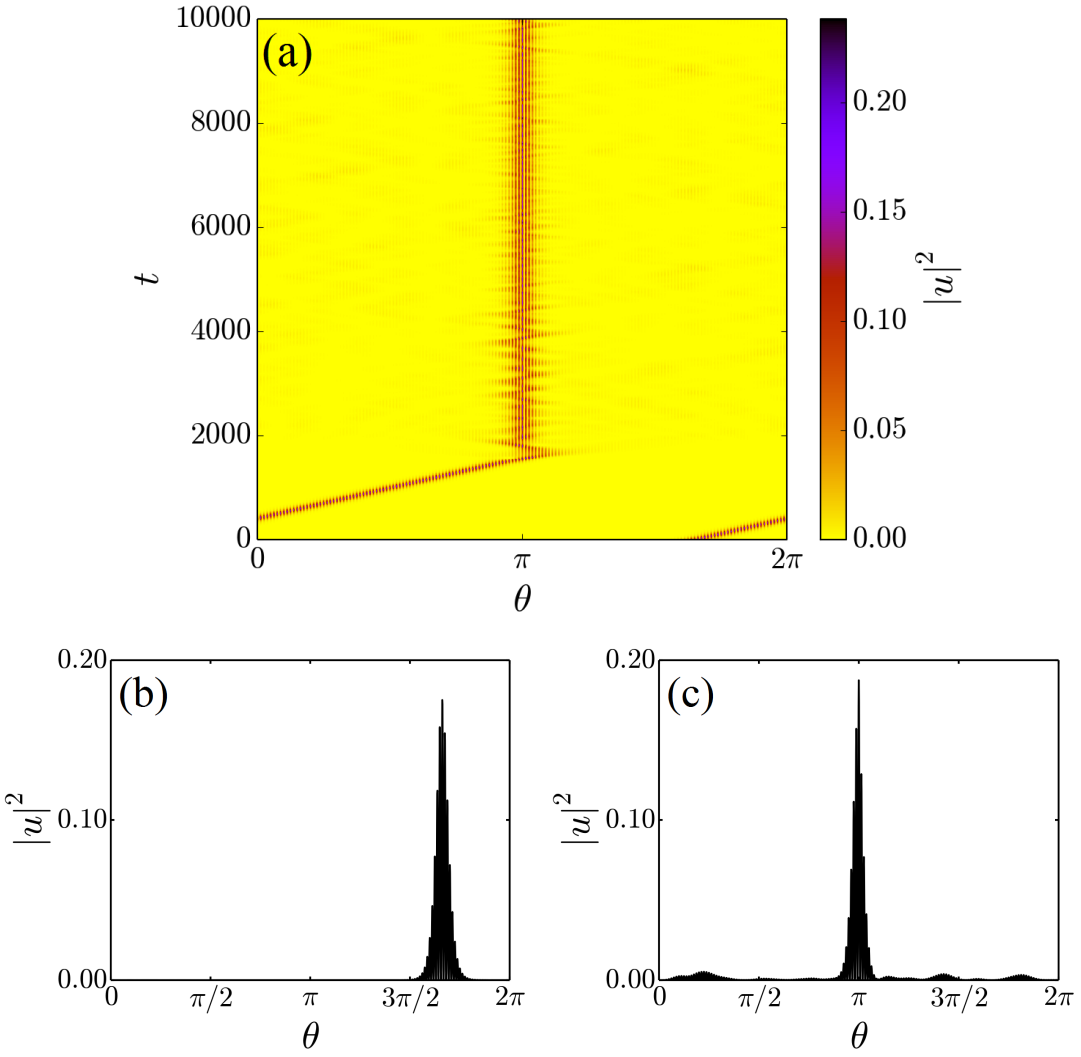

FIGURE 4.6: Collision of single-peaked TLS with potential barrier with $\alpha = 0.06$ and $\beta = 0.3$. (a) shows the time evolution. The TLS is trapped in the barrier and stays there for the duration of the simulation. The intensity distribution is shown at $t = 0$ in (b), and $t = 9960$ in (c), showing that almost the full TLS is trapped, with some atoms going into the background.

4.3 Collision of discrete breathers with a potential barrier

For the discrete model, we use the DNLSE with a Gaussian potential:

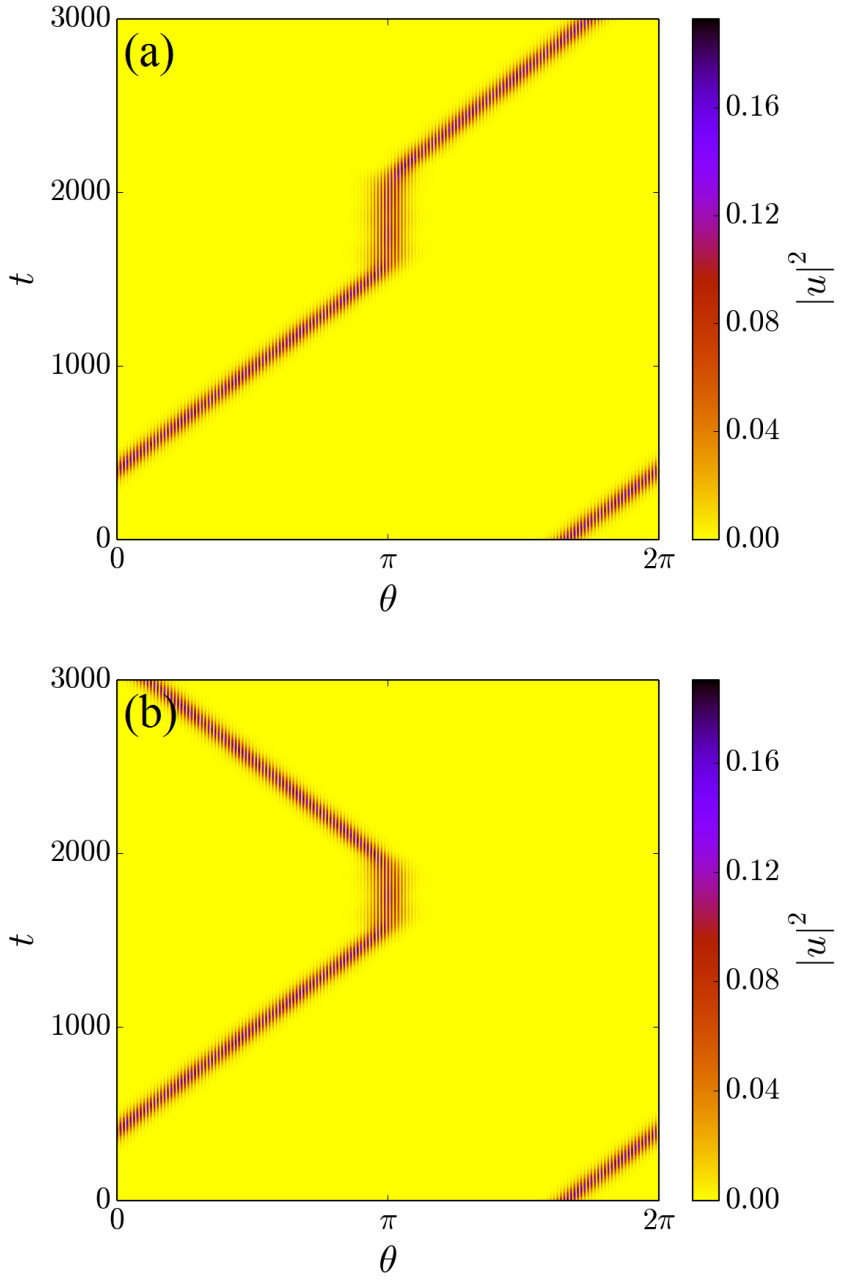

FIGURE 4.7: Collision of single-peak TLS with potential barrier with (a) $\alpha = -0.03028$ and $\beta = 0.3$, and (b) $\alpha = -0.03030$ and $\beta = 0.3$. In both cases, the TLS stays in the centre for a short time before either completely transmitting (a) or reflecting (b).

$$i\frac{d}{d\tau}z_n = \Lambda|z_n|^2 z_n - (z_{1,n-1} + z_{1,n+1}) + \alpha \exp\left(-\frac{(n-n_c)^2}{\gamma}\right) \tag{4.3}$$

where again α is the height of the barrier, γ a measure of the width, and n_c is the location of the centre of the barrier, which here is set to $n_c = 64$.

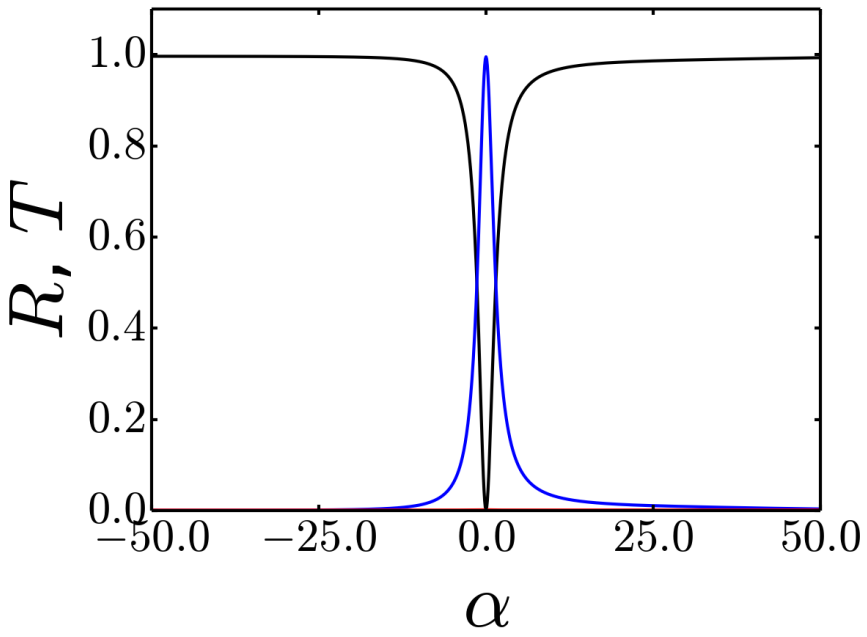

FIGURE 4.8: Ratio of atoms reflected and transmitted off Gaussian potential with height α

For discrete breathers, the results are very similar to those of the single-peaked TLS, their counterpart in the continuous model. The plot of fraction of atoms reflected (R) and transmitted (T) against height (α) shows this (Fig. 4.8). Again for large values of α, there is complete reflection. An example of this is shown in Fig. 4.9. Like the single-peaked TLS, the DB maintains its shape after the collision. This is shown in Fig. 4.9(a) and (b), in which the intensity distibution is shown after the first collision (in (a)) and after the second collision (in (b)) with the barrier. In (c), the evolution of the intensity is presented, showing that the DB maintains its velocity too.

One major difference between the results of this DB and the earlier single-peaked TLS is that there appears to be either no or a very small amount of trapping here. Although trapping has been observed for attractive nonlinearities [53], this

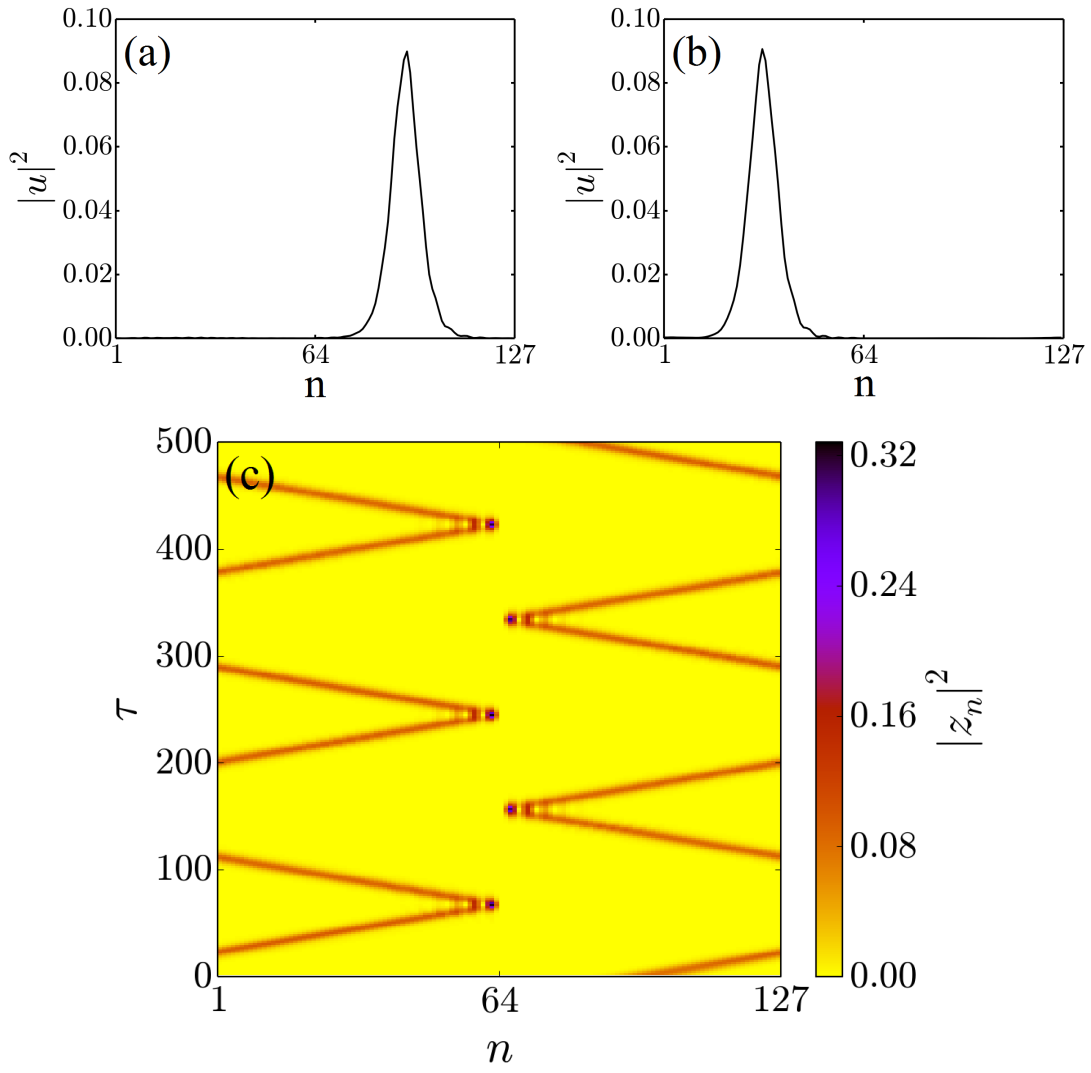

FIGURE 4.9: Full reflection of discrete breather with barrier with height $\alpha = 30.0$. In (a), the breather is shown at $\tau = 0$, travelling in the positive θ direction. In (b), the breather is shown at $\tau = 88$, just after the collision. The time evolution is shown in (c), in which it is seen that the breather survives multiple collisions, maintaining its velocity.

is somewhat expected. The discrete model is obtained in the limit of large V_0. For larger values of V_0 in the continuous model, there is very little trapping of atoms from single-peaked TLSs, the continuous counterpart of DBs. See, for example, Fig. 4.1, with $V_0 = 10$. One can imagine that for even larger values of V_0, there would be no trapping.

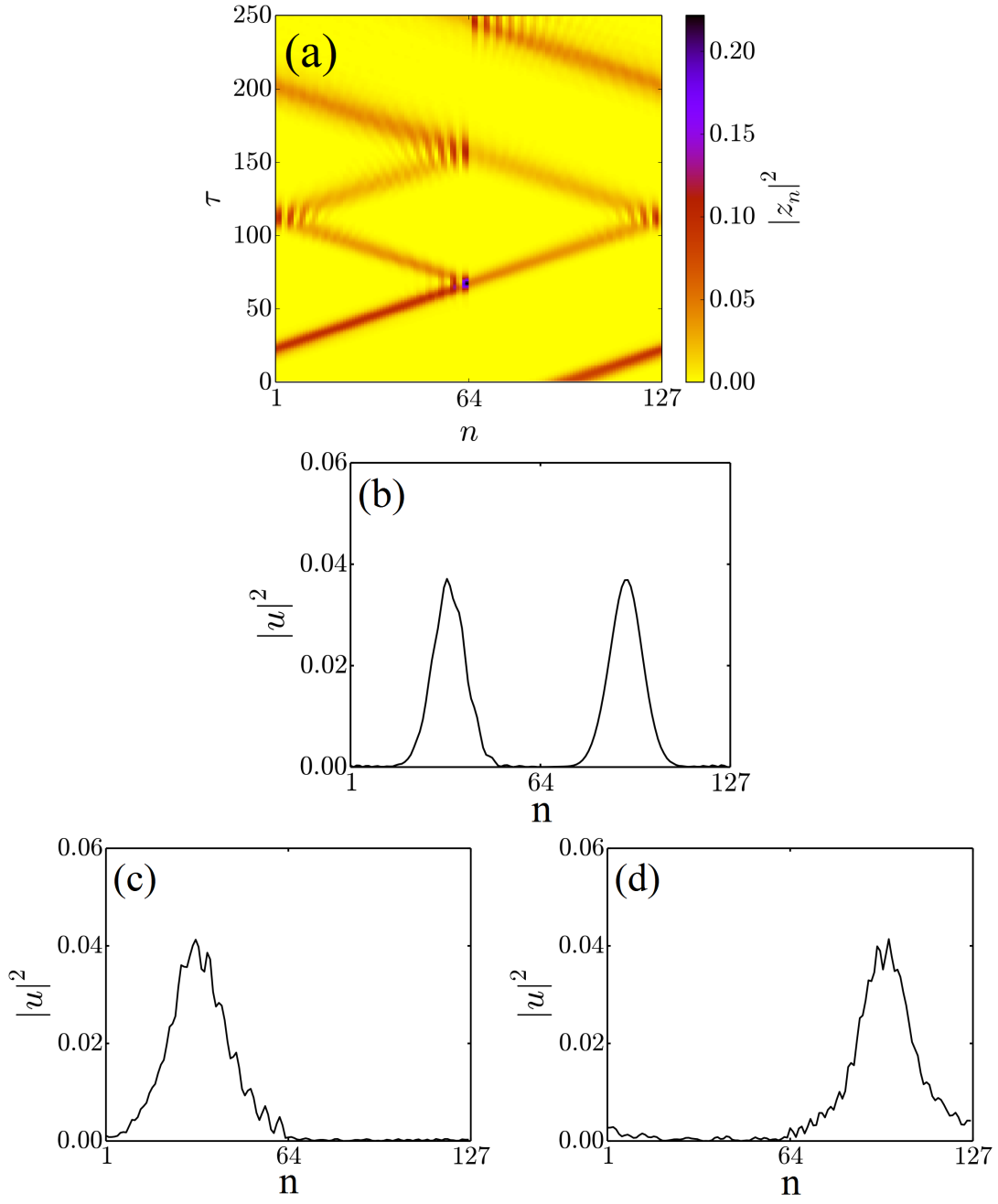

FIGURE 4.10: Collision of discrete breather with barrier of height $\alpha = 1.345$. The time evolution is displayed in (a), in which it can be seen that the breather splits into two. The two outgoing breathers pass through each other before colliding at the barrier, where they recombine. (b) shows the two outgoing breathers at $\tau = 88$, which are approximately the same size. The recombined breather is shown at $\tau = 178$ in (c) and $\tau = 222$ in (d).

Again like the single-peaked TLS, there are regions with partial reflection and transmission where the TLS is split. In Fig. 4.10, a case is presented, where like the TLS in Fig. 4.4, the DB splits into 2 DBs roughly equal in height, before recombining at the barrier (see evolution of intensity in Fig. 4.4(a)). Again, like before the DB(s) lose density to the background during these collisions, so that the resulting DB is smaller than the original one (see Fig. 4.4(b) and (c)).

4.4 Collision of double-peaked TLSs with a potental barrier

In this section, the collision of TLSs with two intensity peaks per potential well (as shown in the previous chapter) with the potential barrier are investigated for $V_0 = 10$. The dependence of the number of atoms reflected (R), transmitted (T) and trapped (S) after the collision on the height α of the barrier is shown in Fig. 4.11. The results of the collisions here are clearly different from the previous examples. For one thing, there is trapping for both positive and negative α. Also, full reflection of the TLS only occurs for positive values of α. For $\alpha < 0$, there are repeated regions of transmission and reflection. The reason for this behaviour is unclear but we believe that it is the unusual form of the double peaked soliton with a minimum in the centre that interferes with the potential barrier.

For the cases of full reflection, the TLS maintains its shape and velocity as before. This is shown in Fig. 4.12. Again, in (a) and (b), the intensity distribution is plotted before and after the collision and in (c), multiple collisions are shown in which the TLS maintains its speed.

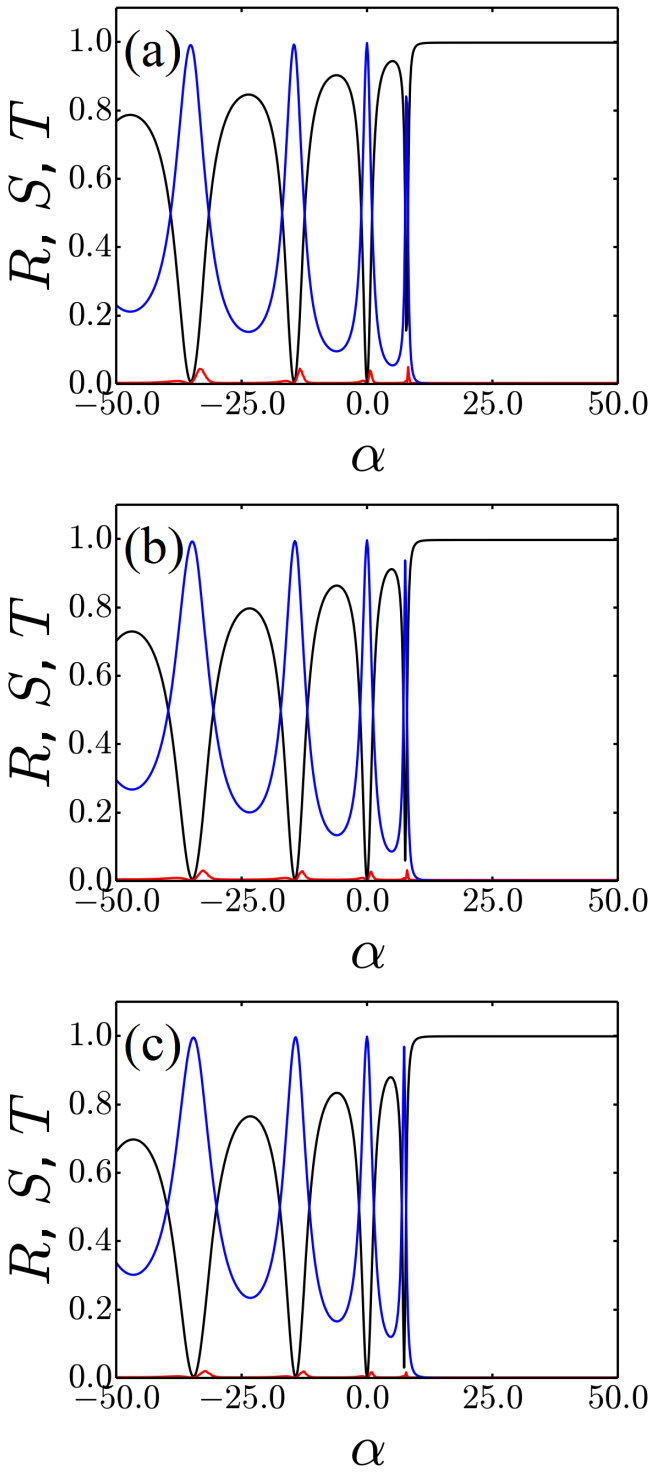

FIGURE 4.11: Fractions of atoms from TLS with two peaks per potential well reflected by (R, black line), transmitted by (T, blue line) and stuck in (S, red line) potential barrier with height α and $\gamma = 0.3$. Potential depths of optical lattice are $V_0 = 10$ (a), $V_0 = 9$ (b) and $V_0 = 8$ (c).

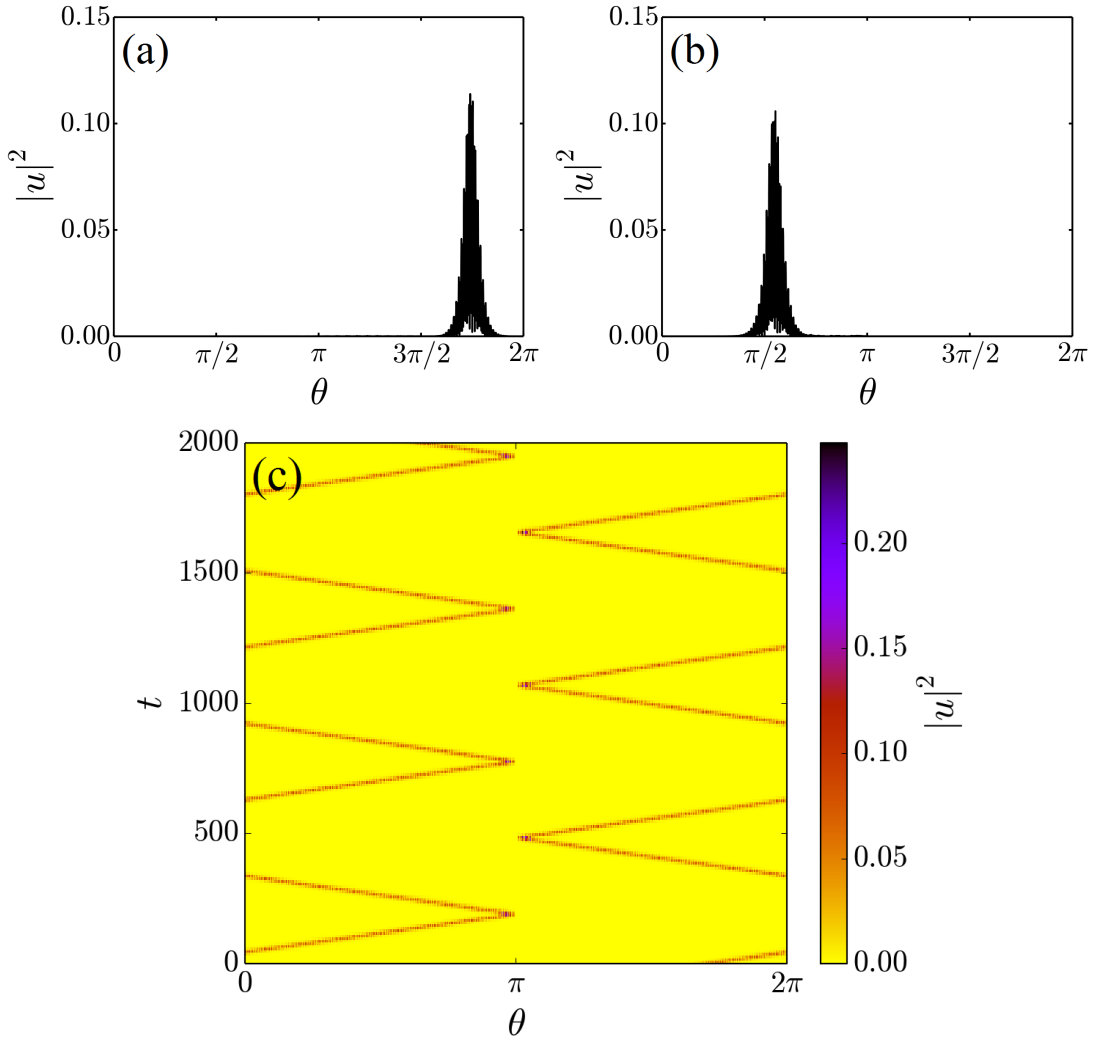

FIGURE 4.12: (a) Initial condition of double-peaked TLS travelling in positive θ direction. (b) TLS after collision with barrier at $T = 250$. As with the previous examples, the TLS has kept its shape after the collision. (c) Evolution of intensity distribution of same collision.

As with the previous examples, there are cases in which the TLS is only partially reflected, splitting into two. In some of these cases, atoms are also trapped in the centre (see Fig. 4.13, with $\alpha = 8.2$). As with the other examples with deep potentials, the amount of trapping is not significantly large. For an example with no trapping, see Fig. 4.14, where, as before, the TLS is split into two TLSs of nearly equal size which then recombine at the barrier. As before, the recombined

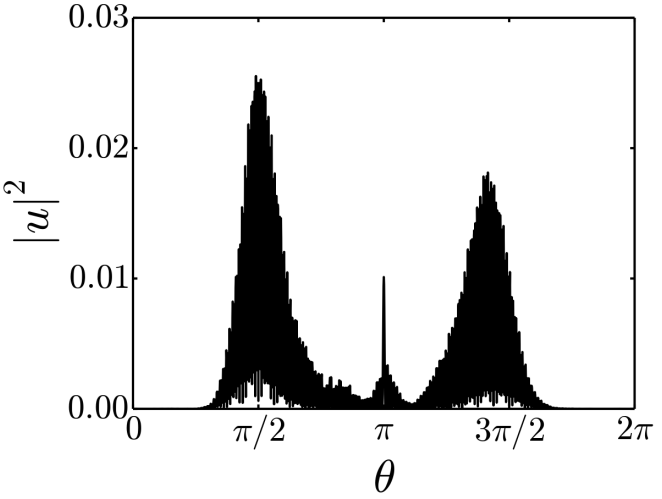

FIGURE 4.13: Partial reflection and transmission after collision with $\alpha = 8.2$. A small amount of atoms are stuck in the barrier at the centre.

TLS is not as large in amplitude as the original, but grows as it travels along the lattice, picking up atoms from the background.

4.5 Conclusions

In this chapter we have investigated collisions of TLSs and DBs with a potential barrier in the form of a Gaussian and the dependence of the collision on the height α of the barrier. First, the collision of the single-peaked TLS with the barrier was investigated in a ring lattice with a deep periodic potential of $V_0 = 10$. For both positve and negative α, there was a smooth transition from complete transmission to complete reflection, with small amounts of trapping for positive α. Inbetween, the TLS was split into two outgoing ones, which allows us to investigate them recombining at the barrier, like a Mach-Zehnder interferometer. For the single-peaked TLS with $V_0 = 2.5$, much more trapping is observed for positive α, with almost the whole TLS being trapped in the barrier. Also, the

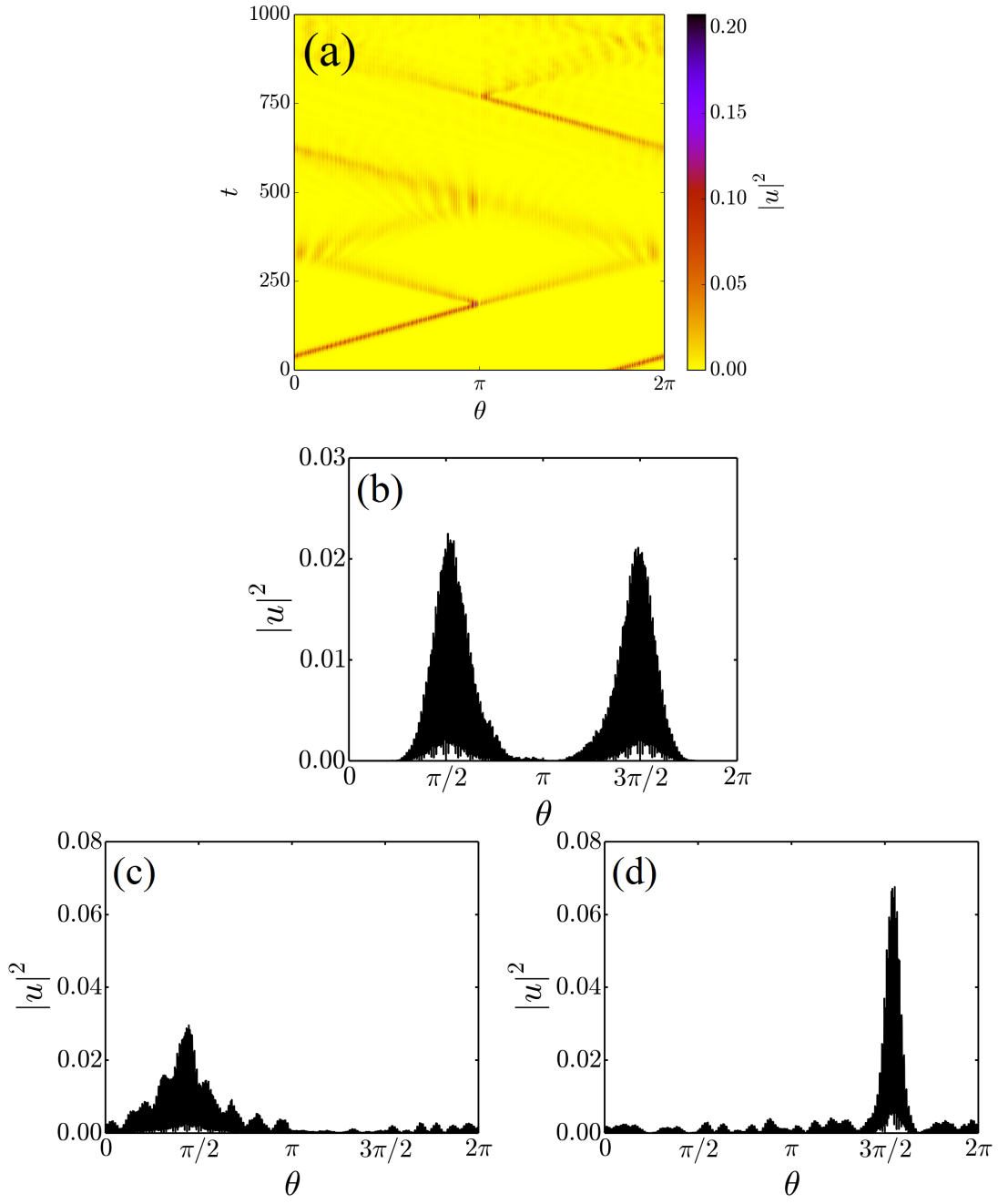

FIGURE 4.14: Multiple collisions of double-peaked TLS with a barrier of height $\alpha = -16.98$. The evolution of the intensity distribution in time is shown in (a). The TLS is split in two at the first collision. The intensity of the two resulting TLSs is shown in (b) at $T = 256$. They pass through each other and then collide again, recombining at the barrier. As seen in (c) at $T = 560$, the TLS formed at this second collision is smaller and fatter than the original. As it travels, it absorbs more density from the background, becoming larger in height. This is seen in (d), at $T = 690$. long survival

transition from complete transmission to complete reflection in much sharper for negative α, possibly due to the larger nonlinearity.

The discrete breather had similar behaviour to the single-peaked TLS, but with little to no trapping as expected for very deep lattice wells.

The double-peaked TLS had unusual behaviour, including repeated regions of trapping, transmission and reflection for negative α, and complete reflection for positive but not negative α. This behaviour is possibly due to the peculiar shape of the double-peaked TLS which presents a minimum of the atomic density in its centre. It is this minimum that interacts and interferes with the potential barrier thus inverting some of the reflection/transmission behaviours observed for the single-peaked TLS with respect to the sign of the barrier height.

Chapter 5

Discrete Breathers in Two-Species Bose-Einstein Condensates

In this chapter, the dynamics of discrete breathers in two-species Bose-Einstein condensates is studied. The analogue to this in the optical case, is light of two different wavelengths propagating through waveguide arrays but as with the rest of the thesis, we focus on BECs in optical lattices here. With a second atomic species in a BEC, there is a nonlinear interaction between atoms of different species as well as ones of their own, leading to richer physics. The interaction between the two species (henceforth described as the "interspecies interaction") has been shown to have many interesting effects, including phase separation [54, 55], and influence on the transport properties of a BEC in a lattice [56, 57]. With repulsive interspecies interactions, *symbiotic* lattice solitons [58–60], i.e. two-species solitons localized together in the same spot of the lattice, can be formed.

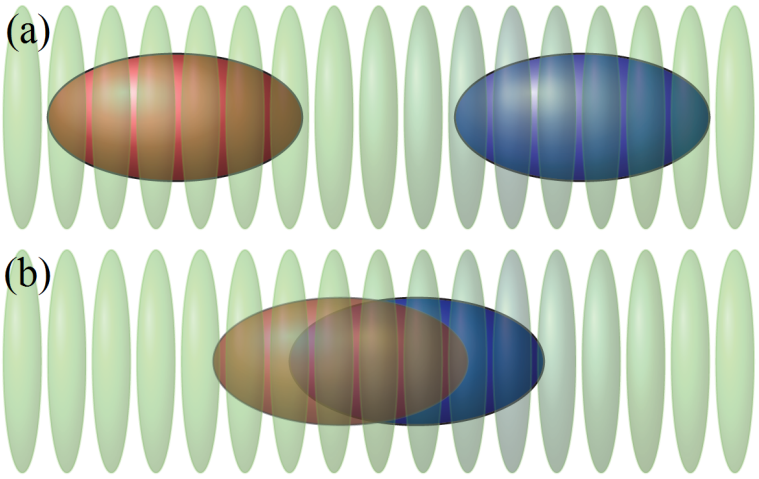

FIGURE 5.1: (a) Two single-species breathers, far apart in the lattice. (b) Two single-species breathers, overlapping in the centre of the lattice, giving rise to the interspecies interaction.

There has been much work on symbiotic solitons and their stability [58–66]. An interesting discovery is that an attractive interspecies interaction can split the two solitons, rather counterintuitively [61]. They have been shown to form through collisions of single-species solitons without a lattice [67], and collisions between symbiotic breathers have also been studied [68].

In this chapter, we study the collisions of two single-species breathers, starting far apart from each other in the lattice (as in Fig. 5.1(a)). The interaction of two stationary breathers in close proximity to one another (as in Fig. 5.1(b)), each of a different species, is also studied. The simulations are performed using experimentally reachable conditions, with specific reference to two feasible experiments of two-species BECs in optical lattices.

The first of these experiments of interest has been performed in Kyoto where BECs of Yb atoms have been obtained separately with isotopes ^{174}Yb [69], ^{170}Yb [70] and ^{168}Yb [71]. A stable mixture of the isotopes ^{168}Yb and ^{174}Yb was obtained [71], as well as a ^{174}Yb and ^{176}Yb mixture [72] which is unstable due to the negative scattering length of the ^{176}Yb component (see also [73]). The intra- and

interspecies scattering lengths of ytterbium isotopes have been measured using data from one- [74] and two-color photoassociation spectroscopy [75] and are now well established. The rich isotope structure of ytterbium enables mass tuning of the scattering length. It has been shown that, unlike in alkali-metal species in which the resulting atom loss is significant, optical Feshbach resonances can be used to effectively change the intraspecies scattering length [76–78]. This raises hope for optical control of interactions between different isotopes, especially now that their positions are known from inter-isotope photoassociation spectroscopy [79]. Three bosonic isotopes of ytterbium, namely ^{168,170,174}Yb, have positive intraspecies scattering lengths of the order of a few nanometers leading to similar stable condensates. Since the isotope shifts are small compared to the detuning of the far off resonant trap (FORT), the potential seen by different isotopes is basically identical. Consequently, given the mass ratios also close to one, this will result in very similar tunneling rates.

Even though these three isotopes are similar in terms of the single-species scattering length, the interspecies interactions of different pairs of isotopes differ dramatically. The interaction between a ^{170}Yb and ^{174}Yb atoms is described by a large negative scattering length of -27.3 nm, while for ^{168}Yb and ^{170}Yb it is positive and equal to 6.2 nm. Halfway between these two is the case of ^{168}Yb and ^{174}Yb characterized by a negligible scattering length of 0.13(18) nm, where the two condensate species should essentially ignore each other.

Another interesting mixture of heteronuclear BECs has been obtained in an experiment of Thalhammer et al. [80], where ^{41}K and ^{87}Rb atoms are condensed together in an optical lattice. A remarkable property of this mixture is that the interspecies scattering length $a_{1,2}$ describing the effective interaction of colliding potassium and rubidium atoms can be tuned over a wide (both positive and negative) range using a magnetic Feshbach resonance, while the single-species

scattering length remains positive for either species. This mixture is an example of one with a large tunneling rate ratio, in contrast to the ytterbium mixtures, where this ratio is close to one.

The structure of this chapter is as follows. In Section 5.1 the derivation of the model and an estimate of the parameters are provided. Interaction of stationary breathers in close proximity to each other is described in section 5.2. Collisions of traveling breathers and trapped states are described in Section 5.3 as a function of the interspecies coupling parameter. Section 5.4 provides an explanation of the different kind of collisions observed in the numerical simulations where inelastic behavior is found in the mutually-repulsive case and elastic in the mutually-attractive case. Finally, section 5.5 shows that the main results of the breather collisions and interactions are robust to survive in a model where the spatial variable is continuous rather than discrete.

5.1 Two Coupled Discrete Nonlinear Schrödinger Equations

We follow the treatment described in [57] to study the behavior of the two-species Bose gas with the use of the tight-binding approximation. With the addition of a second atomic species in the lattice, the time-dependent Gross-Pitaevskii equations describing the dynamics of the two species' order parameters Ψ_i (where $i = 1, 2$) read

$$i\hbar\dot{\Psi}_i(\vec{r}) = \left(-\frac{\hbar^2}{2m_i}\nabla^2 + U(\vec{r}) + \sum_{j=1,2} g_{i,j}|\Psi_j(\vec{r})|^2 \right) \Psi_i(\vec{r}) \,, \tag{5.1}$$

where the coefficients $g_{i,j}$ describe the effective mean-field intra- and interspecies interactions and are given by

$$g_{i,j} = \frac{4\pi\hbar^2 a_{i,j}}{2\mu_{i,j}}\,, \tag{5.2}$$

where $\mu_{i,j} = (m_i^{-1} + m_j^{-1})^{-1}$ is the reduced mass of the atomic pair and $a_{i,j}$ is the scattering length relevant in the scattering properties of the species' atoms.

The external potential confining the BECs is due to two overlapping and counter-propagating laser beams that create a standing wave in the axial direction and, as a result, a periodic potential of depth $V_{0,i}$. The Gaussian profile of the two laser beams gives rise to an approximately harmonic off-axis confinement described by the frequencies $\omega_{r,i}$. Thus the external potential reads

$$V_i = V_{0,i}\sin^2(kX) + \frac{1}{2}m_i\omega_{r,i}^2(Y^2 + Z^2)\,. \tag{5.3}$$

Note that real optical lattices also have a shallow harmonic potential superimposed in the axial direction, which we here assume to have negligible effects. We also introduce the lattice strengths $s_i = V_{0,i}/E_{R,i}$, where $E_{r,i} = \hbar^2k^2/2m_i$ is the recoil energy calculated for the lattice wavelength. The axial on-site frequency of the lattice is then $\omega_i = \sqrt{s_i}\hbar k^2/m_i$.

Both order parameters obey the normalization condition $\int \mathrm{d}^3\vec{r}|\Psi_i|^2 = N_i$, where N_i denotes the total number of atoms of the i-th species in the lattice.

If the lattice is strong enough, i.e. the trap depth is sufficiently large, the condensate is well localized around potential minima. As in Section 2.4, for each of the mixture's order parameters we use the following *ansatz* [30, 57]:

$$\Psi_i = \sum_n \psi_{i,n}(T)\phi_i(\vec{r} - \vec{r}_{i,n})\,, \tag{5.4}$$

where ϕ_i is an on-site wavefunction and $\vec{r}_{i,n}$ is the location of the n-th lattice site seen by the i-th species. As before, if the atomic interactions are weak, the on-site ground state wavefunction can be replaced by the ground state harmonic oscillator wavefunction in the off-axis direction and a Wannier function [31] of the lowest band in the axial direction to account for tunneling. With two species, $|\psi_{i,n}(T)|^2$ can be defined as the number of i-th species atoms in the n-th lattice site as a function of time, with $\sum_n |\psi_{i,n}|^2 = N_i$.

As in Section 2.4, we substitute this *ansatz* into the Gross-Pitaevskii equations (see [30, 57]) and get

$$\begin{aligned} i\hbar\dot{\psi}_{i,n} &= -J_i\left(\psi_{i,n-1} + \psi_{i,n+1}\right) \\ &\quad + \left(\lambda_{i,i}|\psi_{i,n}|^2 + \lambda_{1,2}|\psi_{3-i,n}|^2 + \epsilon_{i,n}\right)\psi_{i,n} \end{aligned} \tag{5.5}$$

where

$$J_i = \int \mathrm{d}^3\vec{r}\phi_i(\vec{r} - \vec{r}_{i,n})\left(\frac{-\hbar^2}{2m_i}\nabla^2 + V_{\mathrm{i}}\right)\phi_i(\vec{r} - \vec{r}_{i,n+1}) \tag{5.6}$$

is the hopping integral describing the tunneling of the i-th species which is proportional to the intersite tunneling rate $\gamma_i = J_i/\hbar$, and $\epsilon_{i,n} = \int \mathrm{d}^3\vec{r}\phi_i(\vec{r} - \vec{r}_{i,n})\left(\frac{-\hbar^2}{2m_i}\nabla^2 + V_i\right)\phi_i(\vec{r} - \vec{r}_{i,n})$ is the on-site chemical potential. The self- and mutual interaction is described by the parameters $\lambda_{i,i} = g_{i,i}\int \mathrm{d}^3\vec{r}|\phi_i(\vec{r})|^4$ and $\lambda_{1,2} = g_{1,2}\int \mathrm{d}^3\vec{r}|\phi_1(\vec{r})|^2|\phi_2(\vec{r})|^2$, respectively.

5.1.1 Normalization

Similarly to Section 2.4, in order to move towards a more standard and computationally efficient form of two coupled discrete nonlinear Schrödinger equation

(DNLSE), we introduce

$$z_{i,n} = \sqrt{\frac{1}{N_i}}\psi^*_{i,n}\,\exp\left(-i\frac{\epsilon_i\tau}{\hbar\gamma_1}\right) \tag{5.7}$$

$$\tau = \gamma_1 T \tag{5.8}$$

to obtain:

$$\begin{aligned} i\frac{d}{d\tau}z_{1,n} &= \Lambda_{1,1}|z_{1,n}|^2 z_{1,n} + \Lambda_{1,2}\frac{N_2}{N_1}|z_{2,n}|^2 z_{1,n} \\ &- z_{1,n-1} - z_{1,n+1} \end{aligned} \tag{5.9}$$

$$\begin{aligned} i\frac{d}{d\tau}z_{2,n} &= \Lambda_{2,2}|z_{2,n}|^2 z_{2,n} + \Lambda_{1,2}|z_{1,n}|^2 z_{2,n} \\ &- \frac{\gamma_2}{\gamma_1}\left(z_{2,n-1} + z_{2,n+1}\right). \end{aligned} \tag{5.10}$$

In Eqs. (5.9-5.10) we have defined the following parameters:

$$\Lambda_{i,i} = \frac{\lambda_{i,i}N_k}{\hbar\gamma_1} \qquad \Lambda_{1,2} = \frac{\lambda_{1,2}N_1}{\hbar\gamma_1}. \tag{5.11}$$

Thus the atomic distribution of each species over the entire lattice is normalized to unity:

$$\sum_n |z_{i,n}|^2 = 1. \tag{5.12}$$

To ensure that the energy and density in the system are conserved, we use a symplectic fourth-order integrator of the Yoshida type [81, 82] (see Appendix A.2). In these simulations of the discrete model we consider that lattice sites outside the condensate are empty resulting in traveling breathers to "bounce" off at reflective boundaries. This is realized experimentally by fixing the size of the condensate with external magnetic fields. This "bouncing" could also be realised with a potential barrier, as in Chapter 4. The energy and density are both conserved up to 9 decimal places at each integration time step.

TABLE 5.1: Values of parameters used in the simulations

Pair	s_1	s_2	γ_2/γ_1	$\Lambda_{1,1}$	$\Lambda_{2,2}$	$\Lambda_{1,2}$
^{168}Yb + ^{170}Yb	3.19	3.27	0.96	5.28	1.368	2.51
^{170}Yb + ^{174}Yb	3.27	3.43	0.91	1.368	2.486	–12.24
^{87}Rb + ^{41}K	7	3.03	6.97	12.31	5.89	(free)

5.1.2 Estimate of the calculation parameters

In Sections 5.2, 5.3 and 5.4 we present results that model different Bose gas mixtures, notably mixtures of ytterbium isotopes and that of ^{41}K+^{87}Rb. At present, the only ytterbium isotope mixture BEC obtained so far is that of ^{174}Yb+^{176}Yb where, however, the ^{176}Yb part instantly collapses because of its negative scattering length [72]. Thus we focus on ytterbium mixtures of isotopes whose scattering length is positive, namely ^{168}Yb, ^{170}Yb and ^{174}Yb. The latter two have already reached BEC separately [69, 70] while the major technical difficulty in reaching a ^{168}Yb BEC is its low natural abundance of 0.13%.

To calculate the self nonlinear parameter, $\lambda_{i,i}$, it is sufficient to approximate the on-site wavefunction $\phi_{i,n}(\vec{r})$ with a harmonic oscillator ground state, which is basically a Gaussian, to yield

$$\lambda_{i,i} = a_{i,i}\sqrt{\frac{2\hbar m\omega_r^2\omega}{\pi}} \tag{5.13}$$

In the case of ytterbium mixtures the mutual interaction parameter $\lambda_{1,2}$ can also be estimated from the above formula as the masses of the two isotopes are very similar and the two wavefunctions are well overlapped.

In the case of the ^{41}K+^{87}Rb mixture the two wavefunctions are differently shaped (one is narrower than the other due to the difference in masses). The scattering length of ^{87}Rb is 5.25 nm [83] while for ^{41}K it is 3.1 nm [84, 85]. The interspecies

scattering length can be changed by the use of a convenient magnetic Feshbach resonance [86] so that $\lambda_{1,2}$ can be considered as a free parameter.

To estimate the tunneling rates γ_i, it is not sufficient to approximate the on-site wavefunctions with Gaussians and one has to use the Wannier wavefunctions. This is because the tunneling rate is mostly determined by the wings of the on-site wavefunction which have an oscillatory-exponential rather than a Gaussian tail. In this case the tunneling rate can be approximated as [87]

$$J_i = \hbar\gamma_i = \frac{4}{\sqrt{\pi}} E_{r,i} s_i^{3/4} \exp(-2\sqrt{s_i})\,. \tag{5.14}$$

The parameters for the ytterbium isotopes considered here are as follows. The lattice laser wavelength is 532 nm; the lattice frequencies for both species are $\omega_r = 2\pi \times 100$ Hz and $\omega = 2\pi \times 15$ kHz which are close to the experimental realizations. For the sake of simplicity, we consider $N_1 = N_2 = O(10^3)$ as it is difficult to find initial conditions that would lead to a *clear* traveling breather at larger densities. This is a general property of lattice solitons [88]. The results apply, however, to larger values of N_i up to 10^5.

In the case of the ^{87}Rb and ^{41}K mixture we consider a lattice wavelength of 1064 nm and we take the (tunable) lattice depth to be $V_0 = 7E_{r,1}$ for rubidium so that the same parameter for potassium is around $V_0 \approx 3E_{r,2}$. This is done to ensure that we can still use the tight-binding approximation (i.e. tunneling rates to further sites are at least an order of magnitude smaller than γ_i, see table I in [87]). On the other hand the tunneling rate needs to be large enough for traveling breathers to exist.

The calculation parameters discussed above are shown in table 5.1.

5.2 Breather interaction

As said in Chapter 2.4.1, initially Gaussian wavepackets can evolve via the single species DNLSE into static breathers [30, 33, 34]. If the wavepacket is given a momentum in a certain direction, traveling breathers that translate across the lattice can also be formed. The general expression of the initial wavepacket is given by Eq.2.41. For two species BECs, the terms in this are given the index i to denote species, like so:

$$z_{i,n} = \sqrt{\frac{1}{\sqrt{2\pi\sigma_i^2}}} \exp\left\{\left(-\frac{(n-\bar{n}_i)^2}{4\sigma_i^2}\right)\right\} \; e^{ip_i n} \tag{5.15}$$

As before, σ_i is the initial width of the Gaussian cloud, and $\bar{n}_i$ is its position. For the single species case, low nonlinearity and values of $|p_i|$ between zero and $\pi/2$, corresponding to a positive $\cos p_i$, the cloud expands diffusively within the lattice. Localization into static breathers is then observed when increasing the repulsive self-interaction $\Lambda_{i,i}$. However, when the pseudomomentum crosses $\pi/2$ and the repulsive self-interaction $\Lambda_{i,i}$ is not too large, traveling breathers are formed (unless $\cos p_i$ is exactly 1, in which case the breather is stationary) [30, 33–35, 42, 89].

In this section, simulations are run starting from stationary breathers of ^{168}Yb and ^{170}Yb in separate positions. These are formed by running simulations of initially Gaussian wavepackets with $\Lambda_{1,2} = 0$ and letting them reshape with dissipation applied at the boundaries to get rid of the background (see [33] for a detailed description of the effects of dissipation). The final stable single-species breathers are of the "staggered" type and evolve in time as $z_{i,n}(\tau) = \exp\{(-i\mu_i\tau)\}(-1)^n v_{i,n}$

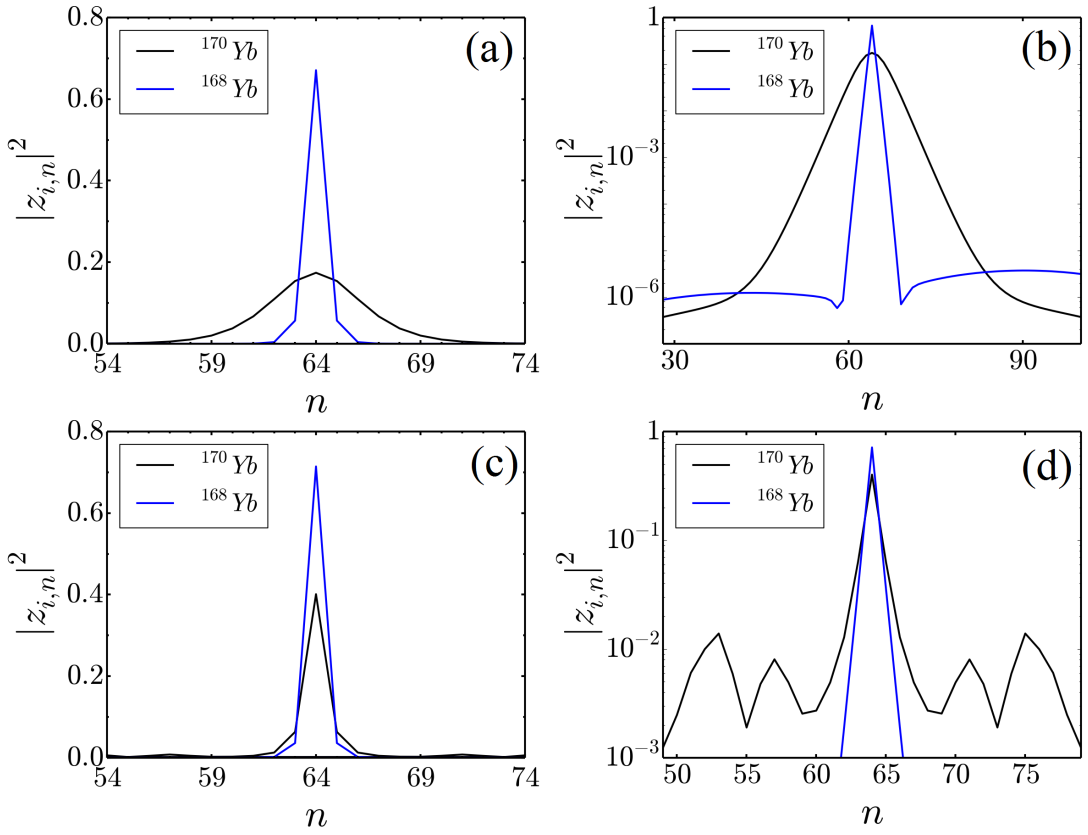

FIGURE 5.2: Density profiles of ^{170}Yb (black solid line) + ^{168}Yb (blue dashed line) mixture for $D = 0$. (a) Initial density profile of ^{170}Yb + ^{168}Yb breathers. (b) Logarithmic profile of this, which shows the exponential tails of the breathers. (c) Density profile of ^{170}Yb + ^{168}Yb breathers at $\tau = 1000$ after $\Lambda_{1,2}$ is switched on. Note that the density profiles have changed when forming the symbiotic breather. (d) Logarithmic profile of this, in which the background of the ^{170}Yb species can be seen more clearly.

where $\upsilon_{i,n}$ satisfies the stationary equations

$$\mu_1 \upsilon_{1,n} - (\upsilon_{1,n+1} + \upsilon_{1,n-1}) - \left(\upsilon_{1,n}^2 + \beta \upsilon_{2,n}^2\right) \upsilon_{1,n} = 0 \tag{5.16}$$
$$\mu_2 \upsilon_{2,n} - \tfrac{\gamma_2}{\gamma_1} (\upsilon_{2,n+1} + \upsilon_{2,n-1}) - \left(\alpha \upsilon_{2,n}^2 + \beta \upsilon_{1,n}^2\right) \upsilon_{2,n} = 0$$

with $\beta = \Lambda_{1,2}/\Lambda_{1,1}$ and $\alpha = \Lambda_{2,2}/\Lambda_{1,1}$. The breathers are spatially localized (Fig. 5.2 (b), in which the exponential tails of the breathers are seen clearly in a

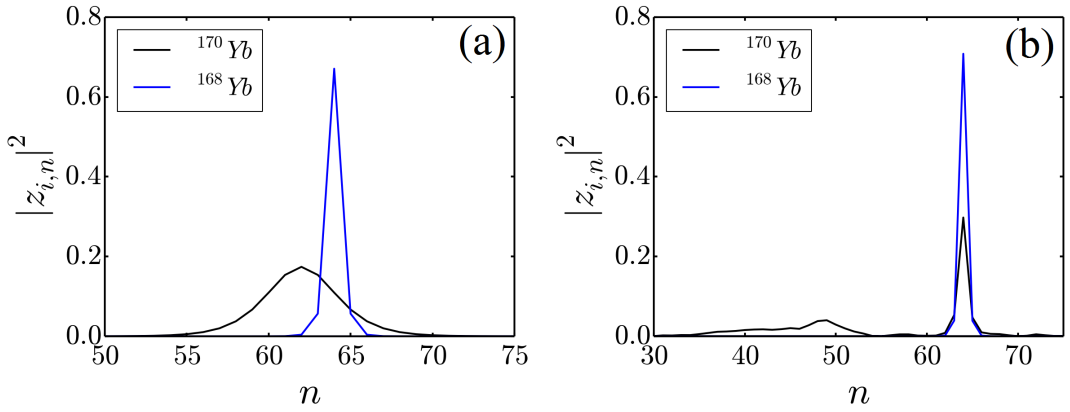

FIGURE 5.3: Density profiles of ^{170}Yb (black solid line) + ^{168}Yb (blue dashed line) mixture for $D = 2$. (a) Initial density profile of ^{170}Yb + ^{168}Yb breathers. The wavefunctions of the two species still overlap significantly. (b) Density profile of ^{170}Yb + ^{168}Yb breathers at $\tau = 1000$ after $\Lambda_{1,2}$ is switched on. Note that the ^{170}Yb is smaller and some of the background has become localized to the left of the main breather.

logarithmic scale). Substituting the exponential ansatz

$$v_{i,n} = A_i \exp\{(-q_i|n|)\} \tag{5.17}$$

into equations (5.16), as in [60], it is found that the decay rates q_i and frequencies μ_i of the breathers are related via:

$$\begin{aligned} q_1 &= \ln\left(\mu_1 + \sqrt{\mu_1^2 - 4}\right) \\ q_2 &= \ln\left(\tfrac{\gamma_2}{\gamma_1}\mu_2 + \sqrt{\left(\tfrac{\gamma_2}{\gamma_1}\mu_2\right)^2 - 4}\right) . \end{aligned} \tag{5.18}$$

Following again [60], an effective Lagrangian is given by

$$L = \frac{1}{2}\sum_n \left(\mu_1 v_{1,n}^2 - 2v_{1,n+1}v_{1,n} - \frac{1}{2}v_{1,n}^4 - \beta v_{1,n}^2 v_{2,n}^2 + \mu_2 v_{2,n}^2 - 2\frac{\gamma_2}{\gamma_1}v_{2,n+1}v_{2,n} - \frac{\alpha}{2}v_{2,n}^4\right) \tag{5.19}$$

Substituting the exponential ansatz Eq. (5.17) into Eq. (5.19) and carrying out the summation gives the effective Langrarian

$$\begin{aligned} 2L_{\text{eff}} = (\mu_1 - 2)A_1^2\text{coth}(q_1) + 2A_1^2\text{tanh}(q_1/2) - \tfrac{A_1^4}{2}\text{coth}(2q_1) \\ -\beta A_1^2 A_2^2\text{coth}(q_1+q_2) + (\mu_2 - 2\tfrac{\gamma_2}{\gamma_1})A_2^2\text{coth}(q_2) \\ +2\tfrac{\gamma_2}{\gamma_1}A_2^2\text{tanh}(q_2/2) - \tfrac{\alpha}{2}A_2^4\text{coth}(2q_2)\,, \end{aligned} \tag{5.20}$$

from which variational equations are obtained via $\partial L_{eff}/\partial(A_1^2) = \partial L_{eff}/\partial(A_2^2) = 0$, which give the relation

$$\begin{aligned} &A_1^2\ \text{coth}(2q_1) + \beta A_2^2\ \text{coth}(q_1+q_2) = 2\ \text{tanh}(q_1/2) + \\ &\quad(\mu_1 - 2)\ \text{coth}(q_1) \\ &\alpha A_2^2\ \text{coth}(2q_2) + \beta A_1^2\ \text{coth}(q_1+q_2) = \frac{2\gamma_2}{\gamma_1}\ \text{tanh}(q_2/2) + \\ &\quad\left(\mu_2 - \frac{2\gamma_2}{\gamma_1}\right)\ \text{coth}(q_2)\,. \end{aligned} \tag{5.21}$$

Solutions with both A_1 and A_2 different from zero and corresponding to symbiotic breathers may exist for $\beta > 0$. In contrast to [60], single-species staggered breathers exist in the uncoupled case of $\beta = 0$. For this reason the existence of symbiotic breathers for $\beta < 0$ cannot be excluded. It can however be stated that symbiotic breathers that are more localized than the original single-species interacting breathers, such as those generated in the numerical simulations below, do not exist for $\beta < 0$. In the case of increasing values of q_i, one can see from Eqs. (5.21) that the fastest growing terms are those containing μ_i that depends exponentially on q_i, while the intensities A_i^2 grow only linearly with q_i. Such growth can only be compensated by a positive term containing $\text{coth}(q_1+q_2)$ on the left hand sides of Eqs. (5.21) and corresponding to $\beta > 0$. It can then be concluded that no symbiotic breathers corresponding to further localization of the atomic density can form with negative β from the interaction of two staggered

single-species breathers.

In the simulations presented in this subsection, the frequencies of the single-species breathers for $\Lambda_{1,2} = \beta = 0$ are found to be $\mu_1 = 2.1$ and $\mu_2 = 4.1$. The decay rates are then calculated using equations (5.18) to get $q_1 = 0.3$ and $q_2 = 1.3$, respectively. Once the breathers are formed and the background noise has vanished, we turned the dissipations off and measured values of q_1 and q_2 within a few percents from the predictions of (5.18).

To study the interactions of these breathers, $\Lambda_{1,2}$ was set to the value of 2.51 and the initial distance D between the centers of two single-species breathers was changed. With the stationary breathers centered on the same site at the start of the simulation ($D = 0$), a symbiotic staggered breather is formed, with the ^{170}Yb breather moving atomic density into the background (see Fig. 5.2 — in (c) and (d) it is shown that the background of the ^{170}Yb breather has increased from around 10^{-6} to around 10^{-2}). The density profile of the symbiotic breather is then different from that of the two single-species breathers corresponding to $\Lambda_{1,2} = 0$. The presence of the interspecies interaction increases both the frequencies μ_i and the exponential slopes q_i of the breathers, making the breathers narrower and more localized. The frequencies are increased to $\mu_1 = 3.1$ and $\mu_2 = 5.3$ and the decay rates are both increased to $q_1 = 1.0$ and $q_2 = 1.6$. The measured values of μ_i, q_i and A_i satisfy the variational Eqs. (5.21) within less than one percent in spite of the approximations made.

This behaviour keeps occurring when the initial distance between the breathers is larger, but still small enough that the initial density profiles overlap significantly. An example of this behavior is shown in Fig. 5.3, for $D = 2$. Here, it is seen that less of the ^{170}Yb atoms join with the symbiotic breather and more are expelled into the background. A small traveling packet is then formed from the atoms in the background. The reshaping process of the ^{168}Yb breather is much the same

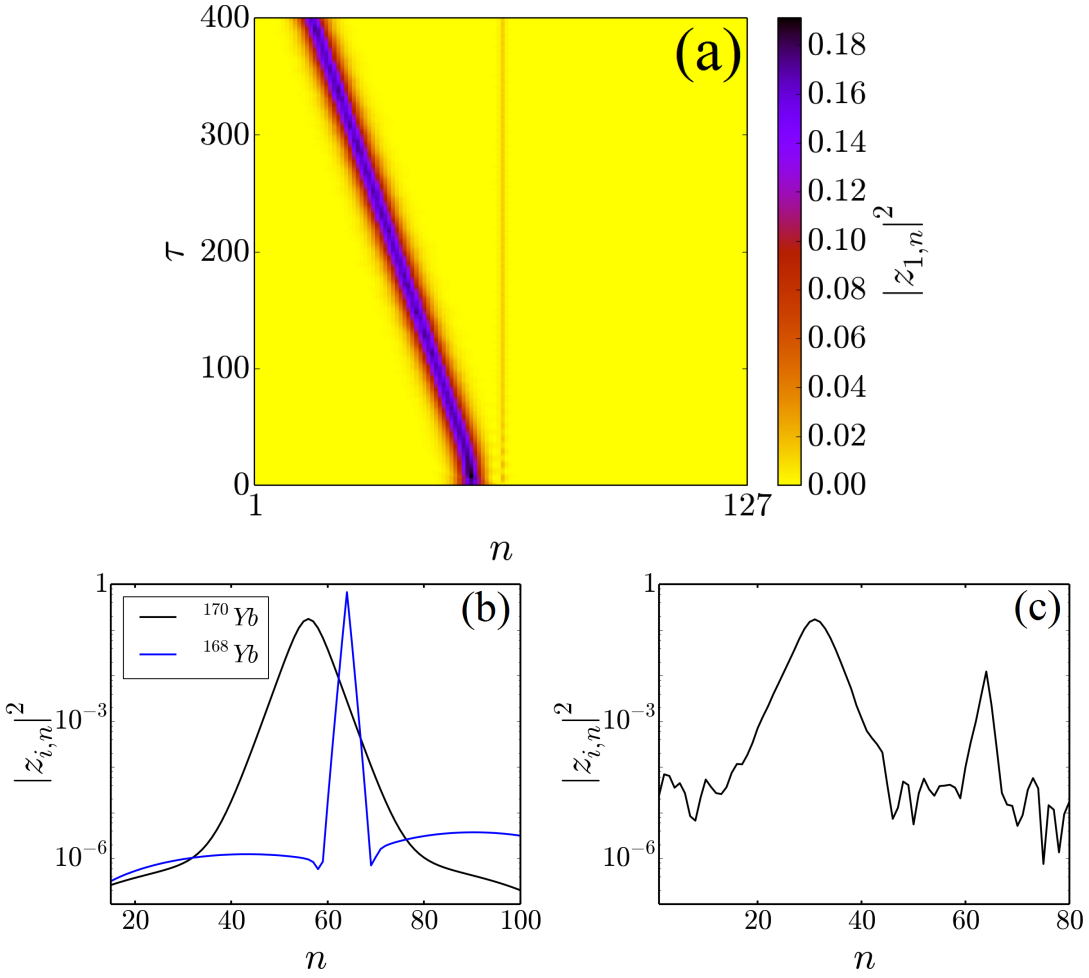

FIGURE 5.4: Interaction between initially stationary breathers in the ^{170}Yb (black solid line) + ^{168}Yb (blue dashed line) mixture for $D = 8$. (a) Evolution of ^{170}Yb part of the mixture. The majority of ^{170}Yb atoms forms a traveling breather while the remaining atomic density is absorbed by the ^{168}Yb breather to form a symbiotic breather. We only show the ^{170}Yb part of the mixture since the ^{168}Yb evolution is rather straightforward, with the breather highly localized in the center. (b) Density profile of the initial condition in a logarithmic scale, showing the overlap at the tails. (c) Density profile of the ^{170}Yb mixture at $\tau = 1000$. Note that the background is significantly higher than in the iniital condition, allowing the breather to travel.

as with $D = 0$. The formation and evolution of a traveling breather out of the interaction of two static breathers of separate species is presented in Fig. 5.4. With $D = 8$, the initial density profiles of the breathers only overlap at the tails (see Fig. 5.4(b)). The result of this is that only a small density of ^{170}Yb atoms

contributes to the symbiotic breather. As D is increased, more ^{170}Yb atoms go into the backeground to support the traveling breather and less in the symbiotic one. A nonzero background is required for the traveling breather to exist [33]. Fig. 5.4(c) shows the logarithmic profile of the ^{170}Yb condensate, in which it is clear that the background is significantly higher than that of the initial condition.

It is important to stress that the motion of the traveling breather made of ^{170}Yb atoms is due to the interaction of the two species via $\Lambda_{1,2}$ being different from zero. In the case of no interaction ($\Lambda_{1,2} = 0$) both breathers remain stationary at all times. No symbiotic breather has been observed to form via the interaction of two single-species breathers for $\Lambda_{1,2} < 0$.

5.3 Collision of traveling and stationary breathers

In this section, the collision of breathers of different atomic species is investigated. This is done by setting one or both of them in motion using the pseudomomentum p_i in the initial conditions given by (5.15). Experimentally, traveling breathers can be constructed by accelerating the lattice confining the condensate. Such accelerations were realized experimentally in [90] and were used to observe a lensing effect on the condensate cloud. In the case of two different species in the same lattice the difference in the masses will naturally lead to different pseudomomenta of the clouds after acceleration to the same group velocity, thus making collisions possible.

Fig. 5.5, shows three symplectic simulations of two colliding traveling breathers, with carefully chosen parameters so that there would be a minimal amount of sound-waves emitted from the initial Gaussian distributions. In all simulations presented in Fig. 5.5 the breathers start from the same initial conditions but with different values of the interspecies interaction parameter $\Lambda_{1,2}$. The color

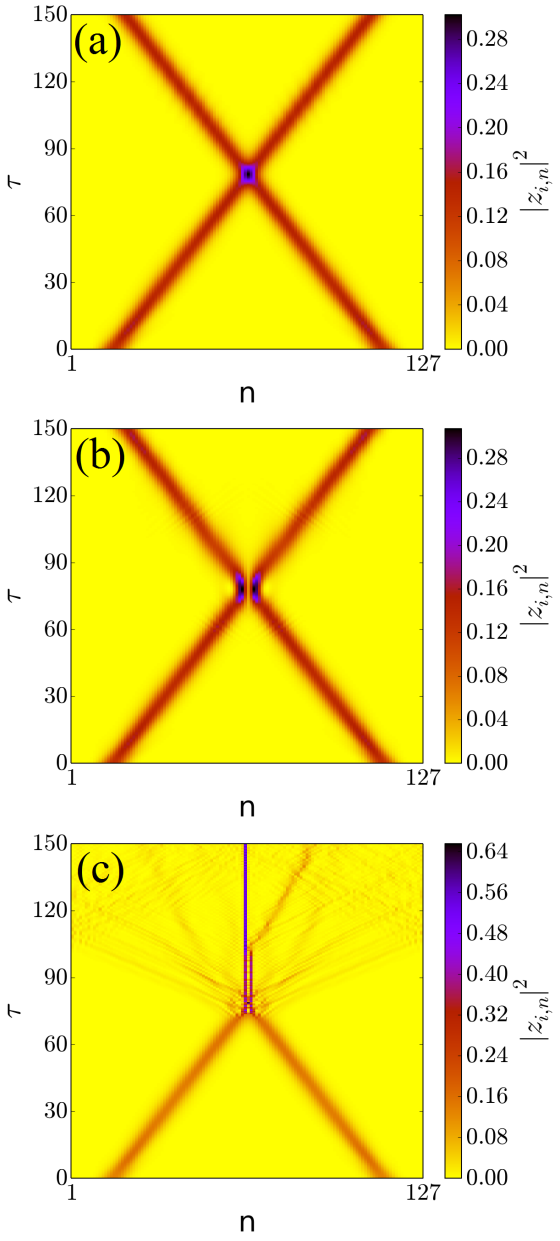

FIGURE 5.5: Collision of two "clean" traveling breathers, with minimal sound-waves. The initial conditions are $\Lambda_1 = \Lambda_2 = 1.1$, $\bar{n}_1 = 16$, $\bar{n}_2 = 112$, $\sigma_1 = \sigma_2 = 3$ and $\cos p_1 = \cos p_2 = -0.95$ for all panels. Note that $p_1 = -p_2$ and therefore the traveling breathers move in opposite directions. $\Lambda_{1,2}$ is set to: (a)0, (b)-20 and (c)30. In (a), the breathers ignore each other acting as if the other species was not present. In (b), the breathers collide elastically. In (c), the breathers are destroyed and a new symbiotic breather is created. The color here represents the total density of the two species, unlike the other figures.

represents the (normalized) atomic density $|z_{n,i}|^2$ with $i = 1$ for one species and $i = 2$ for the other. The simulations start with two Gaussian wavepackets of the form (5.15) with $\cos p_1 = \cos p_2 = -0.95$ and $p_1 = -p_2$ to form two colliding traveling breathers.

In Fig. 5.5(a) when the interspecies interaction parameter $\Lambda_{1,2}$ is set to zero, the breathers follow the dynamics of single-species condensates and pass through each other unaffected. When $\Lambda_{1,2}$ is a non-zero value, the two species affect each other when occupying the same lattice sites. This is shown in Fig. 5.5(b) and (c). At the beginning of the simulations, when the breathers are far apart from one another in the lattice, they follow the same path as in Fig. 5.5(a), until they collide. For large negative values of $\Lambda_{1,2}$, the breathers collide elastically, as shown in figure 5.5(b). In this example, $\Lambda_{1,2} = -20$ and the breathers become narrower when they collide. In Fig. 5.5(c), $\Lambda_{1,2}$ is changed to a positive value and the collision is not elastic. At the collision, the breathers explode, emitting a large amount of sound waves and a stationary symbiotic soliton composed of both species is formed.

It is worth noting that elastic collision occurs when the interspecies interaction parameter is negative, which would normally imply *attractive* interactions between the two species. Normally the two clouds try to achieve maximal overlap in order to minimize energy [67], while in this case the tendency is to minimize the overlap and retain separation of at least a few lattice sites. An explanation of this phenomenon by using the negative effective mass of the discrete breathers is provided in Section 5.4.1.

It should be noted that the single-species traveling breathers are not exact solutions of the DNLS equation due to the emission of sound waves [91]. Nevertheless, they survive well localized for extremely long timescales. For the simulations in

Fig. 5.5, the parameters have been carefully chosen so that the amount of sound-waves emitted from the breathers is minimal and find that, at the moment of collision, the breathers have only lost less than 0.47% of their densities. Without interactions between species, they also survive in simulations with timescales of $\tau \approx 10^6$, which is much higher than the collision times considered here.

The following simulations use parameter values chosen from table 5.1 to model mixtures of ytterbium isotopes and that of ^{41}K+^{87}Rb in realistic configurations. In these simulations, although the initial condition emits large amount of noise, it is found that the main dependance of the collision from the interaction parameter $\Lambda_{1,2}$ remains that displayed in Fig. 5.5.

Fig. 5.6 shows numerical simulations of two colliding breathers in the ^{170}Yb + ^{174}Yb mixture that display similar results to that of Fig. 5.5(b). Note that for all following simulations, the dynamics of each species is shown in separate panels, unlike Fig. 5.5. For example, the left column in Fig. 5.6 shows the ^{170}Yb species, while the right column shows the ^{174}Yb species. In Fig. 5.6(a), at about $\tau \approx 90$ the two breathers collide elastically, as in Fig. 5.5(b) since the interspecies scattering length is large and negative.

Figure 5.6(b) shows a similar situation, except that now one of the breathers (^{174}Yb) is at first stationary ($\cos p_2 = -1$). After the collision the initially traveling breather (almost) stops while the other, up to now stationary, starts traveling. One could argue that this is a manifestation of a form of conservation of momentum. Again, as in Fig. 5.5, the elastic behaviour occurs even though the ^{170}Yb and ^{174}Yb pair is described by a large negative scattering length of $a_{1,2} = -27.3$ nm, which, under normal circumstances, stands for *attraction* between the atoms of the two species.

Compared to the examples in Fig. 5.5, there is a much larger amount of sound waves emitted from the breathers in Fig. 5.6 due to the parameter values used

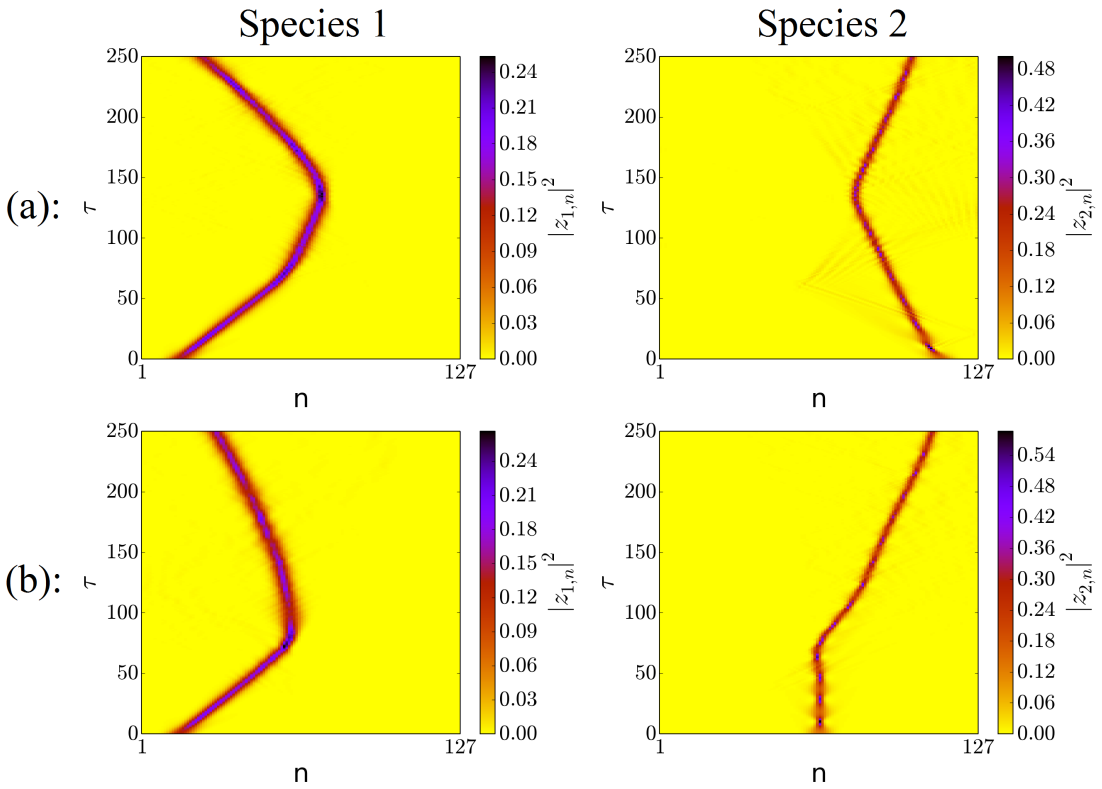

FIGURE 5.6: Collisions of two breathers in the ^{170}Yb (Species 1) + ^{174}Yb (Species 2) mixture characterized by a large negative interspecies scattering length of -27.3 nm. The Gaussian parameters for the initial condition in (a) are $\bar{n}_1 = 16$, $\bar{n}_2 = 112$, $\sigma_1 = \sigma_2 = 3$ and $\cos p_1 = \cos p_2 = -0.95$. For (b), the physical situation is the same as in Fig. 5.6 (a), except that $\bar{n}_2 = 64$ and $\cos p_2 = -1$ to make a stationary breather. In (a), 2 traveling breathers collide elastically. In (b).A traveling breather transfers large part of its (pseudo)momentum to a stationary one and nearly stops.

from Table 5.1. For example, in Fig. 5.6(a), the ^{170}Yb (^{174}Yb) breather loses 1.83% (15.5%) of its density from the sound waves. Small amplitude sound waves do not affect the main collision in a significant way since the central part of each breather acts as an effective barrier to the sound waves emitted by the breather of the other species. Sound waves that would normally expand over the entire lattice are now confined to a region limited by the central parts of the two breathers. The scattering of sound waves due to discrete breathers is investigated in detail in [91].

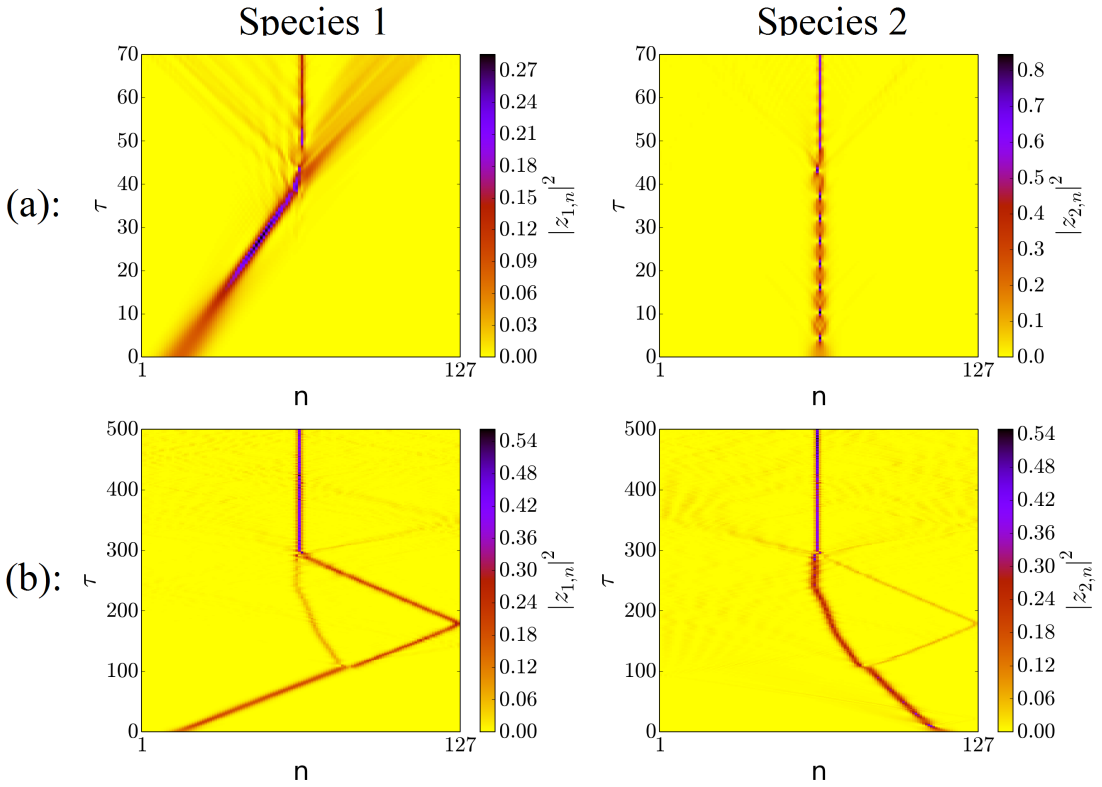

FIGURE 5.7: Inelastic collisions of ytterbium isotopes. In (a), a traveling (^{170}Yb, species 1) and stationary breather (^{168}Yb, species 2) collide for a positive interspecies scattering length of 6.2 nm. The initial condition parameters are $\bar{n}_1 = 16$, $\bar{n}_2 = 64$, $\sigma_1 = 5$, $\sigma_2 = 3$, $\cos p_1 = 0.8$, $\cos p_2 = 1.0$. As in Fig. 5.5(c), the traveling breather is destroyed and a new *symbiotic* soliton is created. In (b) we have the same physical situation as in Fig. 5.6 (a), except that the parameter $\Lambda_{1,2}$ describing the interspecies has now been increased to 4, corresponding to a positive interspecies scattering length of 8.9 nm. In this regime, the two breathers tunnel through each other. Note that a small part of each breather is trapped inside the other forming double-species traveling breathers.

A qualitatively different behavior from the above and similar to that in Fig. 5.5(c), is found in the case of the ^{168}Yb+^{170}Yb pair described by a positive (*repulsive*) scattering length of $a_{1,2} = +6.2$ nm. Due to the large intraspecies interaction of ^{168}Yb it is difficult to construct a clear traveling breather and therefore only stationary ^{168}Yb breathers that are initially stationary can be formed. This situation is presented in Fig. 5.7(a). As in Fig. 5.5(c), at the time of impact ($\tau \approx 40$) the two

breathers literally explode emitting a large amounts of sound waves and forming a double-species symbiotic stationary breather. In this state, the two component wavefunctions are well overlapped. Moreover, the final breather is much narrower than any of the original breathers before the collision. The frequency of oscillation of the two final co-located and co-existing breathers is species dependent. In the case displayed in Fig. 5.7(a) the frequency of the ^{168}Yb breather is about 1.5 times that of the ^{170}Yb breather located on the same site.

To further explore these phenomena simulations were run for the physical situation described in Fig. 5.6(a) of the ^{170}Yb+^{174}Yb mixture but with the interaction parameter $\Lambda_{1,2}$ increased to 4 corresponding to an interspecies scattering length of $a_{1,2} = 8.9$ nm. Such an increase can potentially be achieved using an optical Feshbach resonance. In this situation, interspecies interaction is now positive. The collision is shown in Fig. 5.7(b). Yet another collision behavior is found with these parameters: the two breathers mainly tunnel through each other but at each collision a fraction of the atomic species in one soliton becomes trapped inside the other. Moreover, the breathers appear to accelerate or decelerate for a brief time during the strong interaction. In this simulation, we allow the breathers to collide with each other for a second time, after one has "bounced" off at the reflective boundary. The result is a stationary symbiotic breather.

Quite different results are obtained for the ^{41}K+^{87}Rb mixture, characterized by a large tunneling rate ratio of $\gamma_2/\gamma_1 \approx 6.97$. This, together with the large self-interaction of Rb, changes the physics dramatically.

In Fig. 5.8, collisions of a traveling breather and a self-trapped state of rubidium atoms is shown. Within the range of the simulation parameters that simulates possible experimental realizations, it has proved not possible to initiate a traveling breather state with the Rb condensate due to its large self-interaction. The interspecies interaction parameter is $\Lambda_{1,2} = 3$ for Fig. 5.8(a) and $\Lambda_{1,2} = -9$

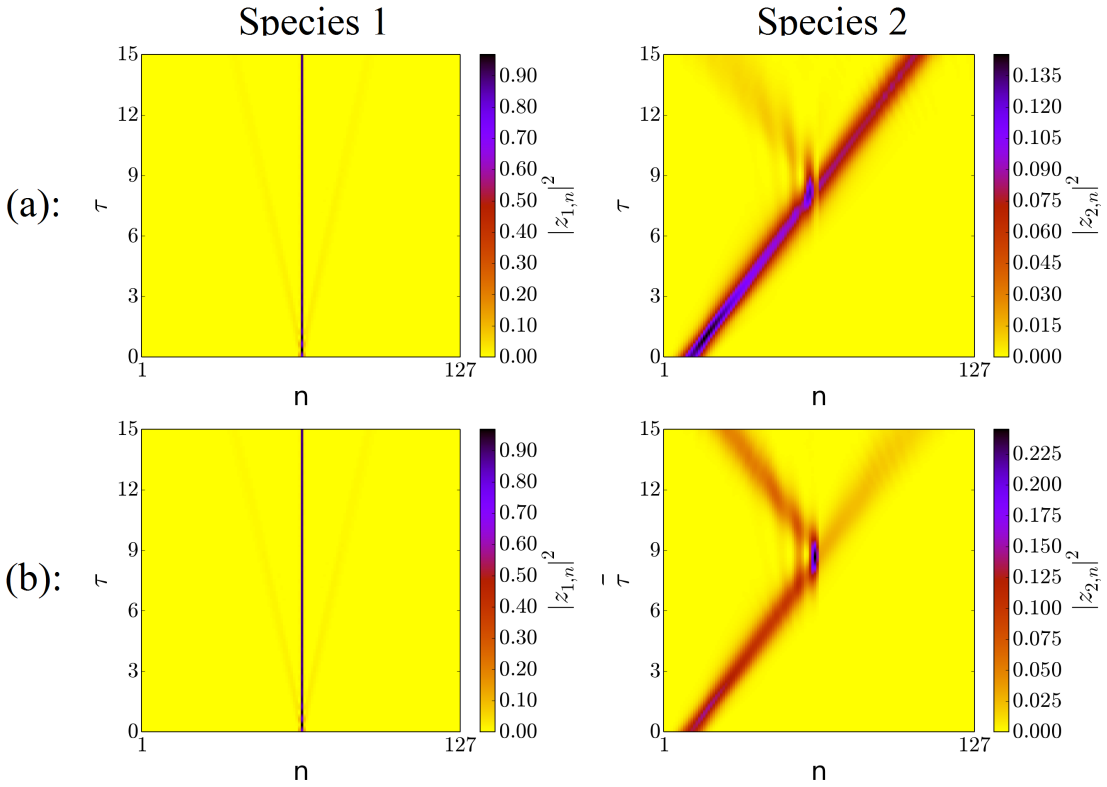

FIGURE 5.8: A collision of a traveling (^{41}K, species 2) and a stationary breather (^{87}Rb, species 1), with the interspecies interaction parameter $\Lambda_{1,2} = 3$ (a) and $\Lambda_{1,2} = -9$ (b). The initial condition parameters are $\bar{n}_1 = 64$, $\bar{n}_2 = 12$, $\sigma_1 = 0.5$, $\sigma_2 = 3$, $\cos p_1 = 1$, $\cos p_2 = -0.9$. In (a), the traveling breather tunnels almost completely through the self-trapped state, while in (b), the traveling breather bounces elastically from the self-trapped state with only a minor proportion tunneling through.

for Fig. 5.8(b). In both cases the rubidium breather acts only as a potential barrier, through which some of the incoming potassium soliton can either reflect or tunnel. This behavior, which contrasts with the phenomena seen in the simulation with ytterbium, can be attributed to the drastically different tunneling rates of potassium and rubidium.

5.4 The collision mechanism

In this section, the dependence of the result of the collisional process with respect to the interspecies interaction $\Lambda_{1,2}$ is investigated. By treating the discrete condensate wavefunctions as distributions the mean lattice site is defined

$$\langle n_i \rangle = \sum_n n \left| z_{i,n} \right|^2 , \tag{5.22}$$

and its standard deviation,

$$\langle \Delta n_i \rangle = \left(\sum_n (n - \langle n_i \rangle)^2 \left| z_{i,n} \right|^2 \right)^{1/2} . \tag{5.23}$$

These two parameters describe the *global* behavior of the condensate. In fact, if a breather splits or is destroyed in a collision, the standard deviation increases dramatically. To assess the *local* behavior, i.e. looking for a new breather created in a collision, the site with the largest number of atoms, $n_{\max,i}$ is found, along with an estimate of the new breather's width (Full Width Half Maximum, FWHM) by counting the adjacent sites which contain at least half the number of atoms of those in the site of the maximum.

Figure 5.9 shows the parameters $\langle n_i \rangle$, $n_{\max,i}$, $\langle \Delta n_i \rangle$ and the FWHM as a function of the mutual interaction parameter $\Lambda_{1,2}$. For each value of $\Lambda_{1,2}$ a simulation was performed up to $\tau = 150$, just past the collision. The initial conditions and interaction parameters are the same as in Fig.5.6, except for the scanned $\Lambda_{1,2}$ and the tunneling ratio γ_2/γ_1, which is set to 1.

Four different regimes can be identified from Fig. 5.9. On the left, for $\Lambda_{1,2}$ lower than about -2.0, two traveling breathers collide elastically and remain basically unaffected by the collision. This is the situation shown in figure 5.6. Then, there is a transition point at $\Lambda_{1,2} \approx -1.5$ where the each breather splits into two as

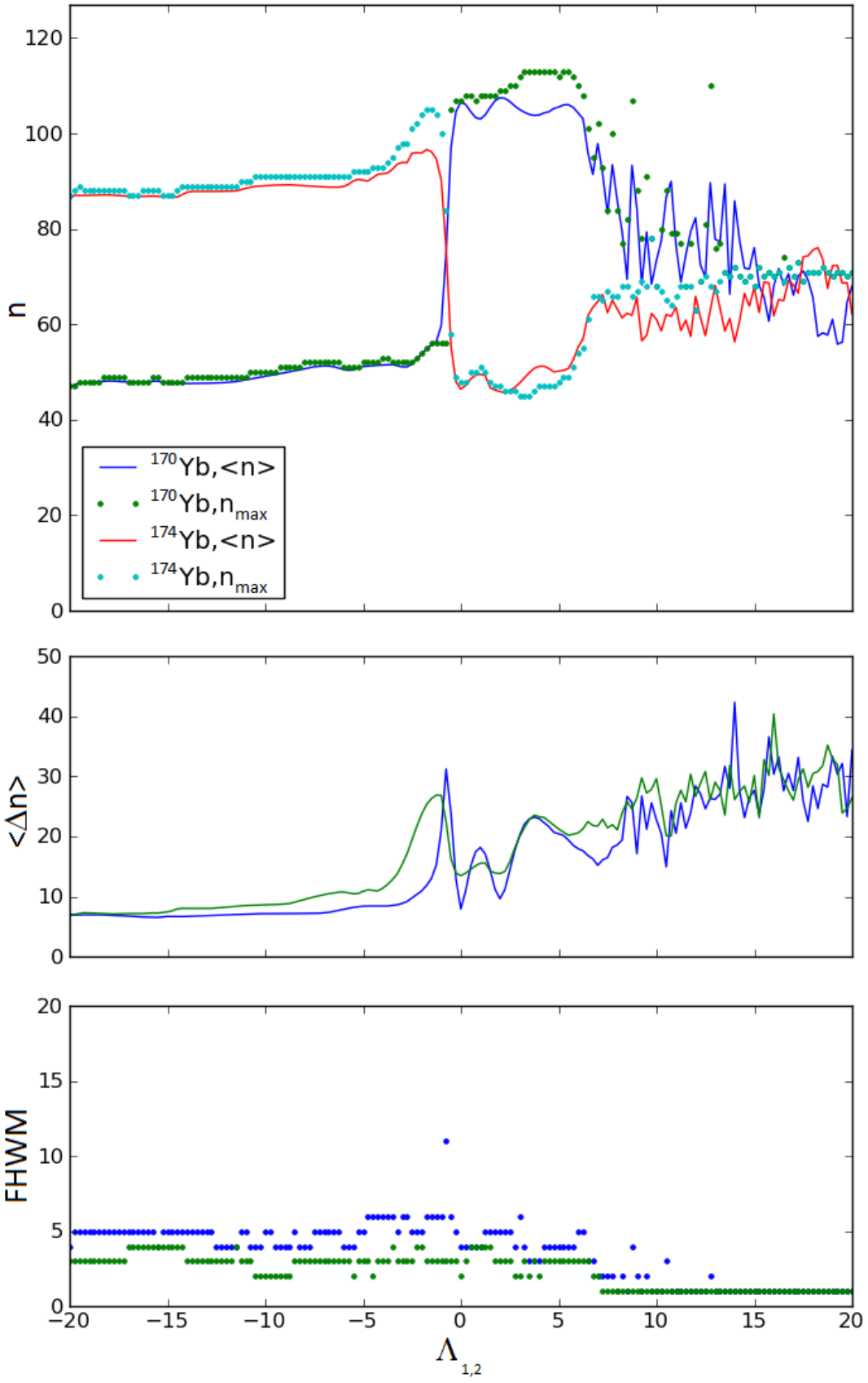

FIGURE 5.9: The collision outcome as a function of the interspecies interaction, $\Lambda_{1,2}$. The top panel displays the mean and the peak site per species, the center panel the standard deviation per species, and the bottom panel the FWHM per species as defined in the text. Symplectic simulations corresponding to the ^{170}Yb+^{174}Yb mixture.

they collide. This results in a sudden increase of $\langle \Delta n \rangle$ for each species. Note that this increase differs between the two species; for ^{174}Yb it's maximum is located at $\Lambda_{1,2} \approx -2$ as opposed to $\Lambda_{1,2} \approx -1$ for ^{170}Yb, quite probably as a result of the different self-interaction parameters.

For small, but positive values of $\Lambda_{1,2}$ (i.e. less than 6) the two breathers tunnel through each other. Note that $\langle \Delta n \rangle$ remains low in this regime (about 15 sites, growing slowly to 20) which means that the breathers are not destroyed. This is shown in Fig. 5.7(b) for $\Lambda_{1,2} = 4$. As the two breathers tunnel through each other, a part of their wavefunction is trapped inside the other soliton; this effect grows as the interspecies interaction increases leading to a slow increase in the standard deviation of the atomic density distributions.

A rather sudden change takes place at about $\Lambda_{1,2} = 6$. The system becomes visibly sensitive to small changes in the mutual interaction. This is the regime where the collision results in the destruction of the two breathers. Fig. 5.7 is an example of such a case. The process is chaotic, yet in many cases leads to the creation of a double-species symbiotic breather manifested by its very low FWHM.

5.4.1 Discussion

The presented results can be reasonably explained by using one of the key phenomena at the base of lattice solitons: the *negative effective mass*. The dynamics of a lattice soliton in an external potential are exactly opposite to what one would expect - a lattice soliton attempts to climb potential hills and in itself is a balance between its negative effective mass that tries to make it collapse and its repulsive self-interaction that prevents it [30, 61]. In fact, the variational model

of a wavepacket used in Trombettoni *et al.* [30] shows that the wavepacket center obeys a Newton-like dynamics when $p \approx 0$ and exactly the contrary when $p \approx \pi$.

This 'contrary' behavior of the solitons seems to be the key to the explanation of these findings. The totally elastic collision encountered when the interspecies interaction is highly *attractive* would be caused by the fact that the solitons 'see' each other as potential walls rather than wells.

The splitting behavior has been investigated in a slightly different context by Matuszewski *et al.* [61] where the dynamics of two already overlapped stationary solitons was analyzed. In our case splitting happens if the attractive interaction is small enough to let the two breathers overlap briefly. Then the system becomes unstable and each breather splits in two. It is also possible to look at this phenomenon from a different angle. Due to its negative effective mass, the split of the breather is quite similar to the case of a wavepacket encountering a potential barrier where, depending on the barrier height (or the interaction between the breathers) part of the wavepacket goes through while the rest is reflected.

In the repulsive interaction regime the breathers behave as if they saw each other as potential wells. This is again an effect of their negative effective mass and, consequently, reversed dynamics. Thus, for the collision's duration, their speed increases (at the cost of wavepacket spreading and of a reduction of their energy due to atomic self-interaction).

The chaotic behavior when the interspecies interaction is large and repulsive is probably caused by the system entering an unstable regime as predicted by Gubeskys *et al.*[58]. The chaotic dynamics would then cause the destruction of the original two breathers and possibly the creation of a stable *intragap* soliton. It is beyond the capabilities of the discrete model to establish if it is possible for an *intergap* soliton to emerge during the collision since the tight-binding approximation is limited to the lowest band-gap by definition.

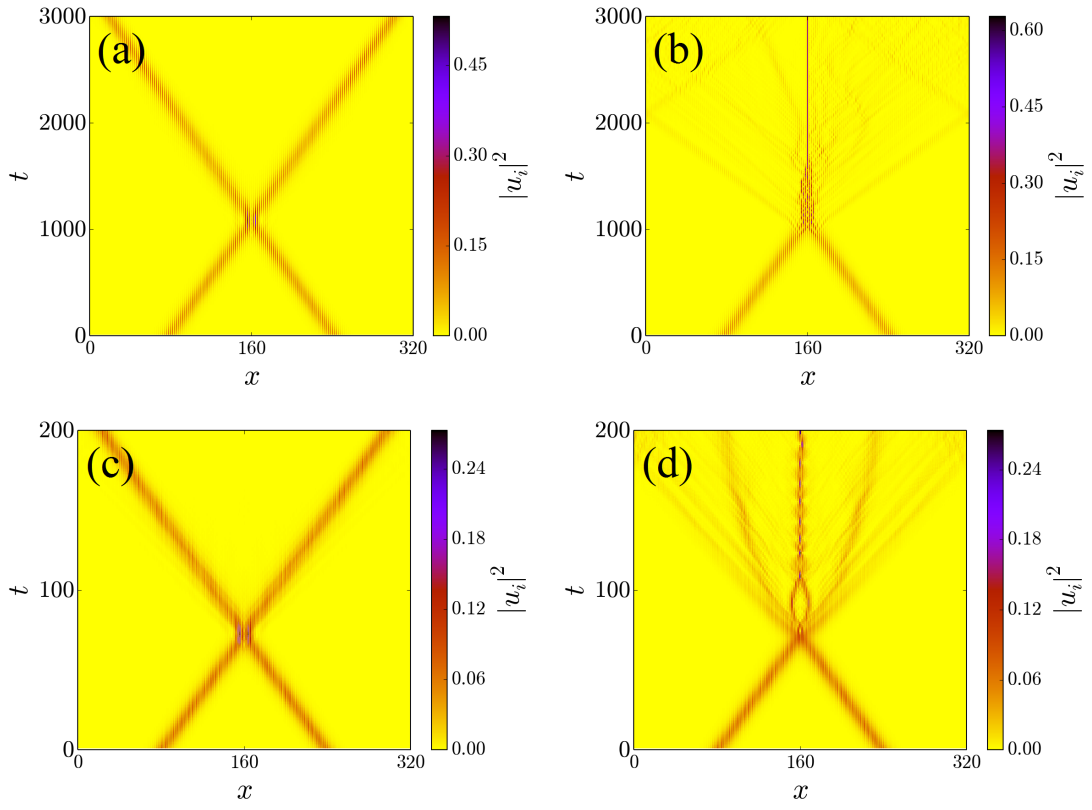

FIGURE 5.10: Collision of two TLSs in the continuous case (5.24). Panels (a) and (b) show collisions of TLS with one intensity peak per potential well (defined in 3.5), while panels (c) and (d) show collisions of TLS with two peaks per potential well (defined in 3.4). In both cases, a negative values of $\beta_{i,i}$ (-2 in (a) and -18 in (c)) gives an elastic collision, while symbiotic solitons are created with positive ones (2 in (b) and 20.4 in (d). These results are similar to those displayed in Fig. 5.5(b) and (c) for the DNLS model.

5.5 Collisions of Travelling Lattice Solitons in the Continuous Model

The DNLS model describes BECs in optical lattices in the limit of deep potential wells. The interactions and collision mechanisms of breathers in two-species BECs presented in Sections 5.2, 5.3 and 5.4 survive the tight-binding approximation. Here, a scaled version of the one-dimensional Gross-Pitaevskii equation (similar

to Eq.2.20) extended to two-species BECs in optical lattices is:

$$i\dot{u}_i = \left(-\frac{\partial^2}{\partial x^2} + V_0 \sin^2\left(\frac{\pi x}{2}\right) + \sum_{j=1,2} \beta_{i,j}|u_j|^2 \right) u_i \,, \tag{5.24}$$

where u_i is the wavefunction of the i-th species, $V_0 = 10$ is the potential depth scaled to the recoil energy, $\beta_{i,i}$ and $\beta_{1,2} = \beta_{2,1}$ are the intra- and interspecies interaction parameters respectively. The spatial variable x is now continuous and the Laplacian term describes the momentum of the atoms in the lattice. It is shown here that the collision mechanisms survive from the discrete to continuous limit by simulating an optical lattice of 160 potential wells.

In Fig. 5.10 (a) and (b), collisions of two TLSs with one intensity peak per potential well, as defined by Eq. 3.5, are shown. In (a), with $\beta_{1,1} = \beta_{2,2} = 0.04$ and an attractive interspecies interaction of $\beta_{1,2} = -2$, an elastic collision is obtained by the numerical integration of Eq. (5.24). Likewise, inelastic collisions take place with repulsive interactions as shown in Fig. 5.10(b), with $\beta_{i,j} = 2$. The inelastic collision here ends in the formation of a symbiotic lattice soliton.

Collisions of two TLSs with two intensity peaks per potential well, as defined in Eq. 3.4, are shown in Fig. 5.10(c) and (d). Despite this TLS not having an analogue in the discrete case due to its shape, the same basic results as both the discrete breathers and single-peaked TLSs is observed. An elastic collision is observed in (a), with $\beta_{1,1} = \beta_{2,2} = 1.0$ and a large attractive interspecies interaction of $\beta_{i,j} = -18$. Similarly, repulsive interactions give inelastic collisions, shown in Fig. 5.10(d), with $\beta_{i,j} = 20.4$. As with the single peak, the example shown here produces a symbiotic lattice soliton.

The simulations of the continuous model (5.24) take at least six times as long as those of the discrete model, even with the similar number of potential wells (160 in the continuous compared to 127 in the discrete). It should also be noted

that the numerical method used for the continuous case is not symplectic and uses periodic boundary conditions that limit its application. In spite of these limitations, the results of the continuous model simulations confirm those of the DNLS model in the deep potential case as demonstrated in Fig. 5.10. For these reasons, the DNLS model represent an accurate and trustworthy testbench for the realistic investigation of the collision mechanism of breathers in two-species BECs as shown for example in the exhaustive Fig. 5.9.

5.6 Conclusion

In this chapter, the behavior of interacting and colliding discrete breathers in BECs composed of different atomic species in optical lattices has been studied. We have found that the interaction depends on the initial distance of the two breathers and led either to the formation of a symbiotic solitons or to the setup in motion of one of the two breathers. The collision outcome depends both on the tunneling rate ratios of the two species, as well as the interspecies interactions. When the tunneling rates differ greatly, as in the ^{41}K+^{87}Rb mixture, one of the breathers acts as an effective potential wall to the other and the whole process can be viewed as a case of one-particle scattering on a potential wall.

In the case where the tunneling rates are comparable (like in the case of mixtures of ytterbium isotopes) we have identified four collision regimes. For large negative scattering lengths the collision is elastic and the two traveling breathers remain intact, with considerable momentum transfer between the two. For small negative scattering rates, the breathers overlap briefly and split in two, as originally predicted in [61]. When the interspecies interaction is weakly repulsive, the two breathers tunnel through each other unharmed for a wide range of interspecies interacions. Finally, with the interspecies interaction sufficiently large, the

dynamics becomes chaotic and the two breathers are destroyed with a possible creation a new two-component soliton similar to an *intragap* soliton as predicted in [58]. Feasible explanations to the above phenomena have been provided using the concept of negative effective mass and the resulting reversed dynamics.

Interaction and collision properties of localized excitations in BECs in optical lattices can have interesting applications in the realization of ultracold Bose-Fermi mixtures where lattice solitons can be viewed as matter-wave counterparts of quantum dots and antidots [92]. Changing the species interaction allows one to tune the character of the collisions from fully elastic to fully inelastic and/or tunneling with clear advantages in the manipulation of information in matter-wave systems.

Chapter 6

Conclusions

Since the realisation of the first BEC in 1995, it was realised that many atoms can display macroscopic phases, wave features and nonlinear interactions at very low temperatures. This has lead to the re-discovery of every single phenomenon of nonlinear and quantum optics in the atomic domain.

In this thesis we have focused on localisation and the formation and interaction of solitons that were fist discovered in the nonlinear optics domain and later extended to the BEC regimes via universality. New features such as higher order travelling lattice solitons, boundary induced localisations, and interacting breathers in two species BECs have been identified and, in an interesting turn of events, extended from the BEC configurations to arrays of optical waveguides. In particular a theoretical study of localisation in BECs in optical lattices has been presented, in both a continuous model via the Gross-Pitaevskii equation, and a discrete model via the Discrete Nonlinear Schrödinger equation. This was studied in three different situations.

Firstly, in Chapter 3, a model of a BEC in a ring optical lattice with atomic dissipation was studied in the continuous GPE with angular coordinates. The

localized dissipation can be applied at a stationary or moving location on the ring and was shown to generate and stabilise stationary and travelling lattice solitons. It was seen that, in a similar way to the discrete case of the DNLSE [35], localised modes could be found by applying localised atomic dissipation. Also, the dissipation could clear noisy backgrounds (which would persist in a conservative model) and stabilise the localized mode. A novel travelling lattice soliton with two intensity peaks per potential well was presented in Section 3.3 of Chapter 3. This cannot be reproduced in the discrete model due to its shape. Then, collisions between stationary and travelling lattice solitons was investigated. It was found that the amplitude of the SLS affected the interaction. Collisions between two travelling lattice solitons, both with either one or two peaks per potential well, were also investigated. During the collision, some of the atomic densities of each TLS passed through and some was reflected. This was done in such a way that the shape of the TLSs after the collision was the same. The fraction of atoms that were reflected or transmitted was found to change with different potential depths of the lattice.

In Chapter 4, collisions of travelling lattice solitons with a potential barrier in the form of a Gaussian peak or trough was studied. Collisions of two different types of TLS and of a discrete breather with the barrier were considered, along with the dependence of the collision on the barrier height. For each of these, regions were found corresponding to complete reflection, where the travelling solitons reflected off the barrier, maintaining their shape and velocity. Regions were also found in which the TLS was split in two. The ring lattice allowed us to consider a situation similar to a Mach-Zehnder interferometer in which the two split TLSs were allowed to recombine with the barrier. This situation has been considered previously but without an optical lattice in [43]. The use of the lattice allows for all these considerations to extend to the case of repulsive condensates. Collisions of the double-peaked TLS with the barrier produced unexpected results,

including trapping in regions in which there should be none, and repeated regions of reflection and transmission, possibly from interference effects.

In Chapter 5, we investigated discrete breathers in two-species BECs, in which the interaction between atoms of different species provides a further nonlinearity. It was found that the interaction between two stationary breathers is dependent on the distance between them. Results of this ranged from the formation of symbiotic breathers composed of both species, to the transformation of one of the breathers from a stationary one into a travelling one. The collisions of breathers were found to depend heavily on the interspecies interaction parameter. For two breathers composed of different species and with similar tunneling rates, four collision regimes were identified, ranging from elastic when the interspecies interaction is large and attactive to mutual destruction when the interaction is large and repulsive. The results of the discrete regime were extended and verified in the continuum case thus strengthening the feasibility of experimental observation.

Although the work presented in this thesis has covered a large number of continuous and discrete lattice solitons, their stability and their interactions, the research into localisation of atomic density in BECs in optical lattices or light in arrays of optical waveguides is far from complete.

One method of supporting solitons in nonlinear media is that of localized gain (for a review, see [95]). There is also great interest in parity-time symmetric systems [96], for which, when applied to a BEC, localized gain and dissipations are balanced (for recent reviews about nonlinear systems, see [97]). It should be possible to implement this technique in the models described in this thesis, with the gain being provided by an atom laser [98]. Indeed, such a setup is described in [99] for a ring trap without a lattice.

Since the GPE and the DNLSE have been obtained under the mean-field approximation, which is valid in the limit of large numbers of atoms, purely quantum

effects arising from atom-atom correlation, such as the collapse and revival of the matter wave field [100] or many-particle entanglement [101, 102], have not been considered here. A detailed investigation of these effects is beyond the scope of this thesis, although recent studies concerning localization of a BEC in an optical lattice in the presence of localized dissipations and beyond the mean-field approximation can be found in [32, 102, 103]. All these simulations confirm that the fundamental result of self-localization via localized losses, originally obtained in [35], survives in the quantum regimes beyond the mean-field approximation.

Discrete breathers in the DNLSE have been associated with negative temperature states. A study of this was presented in [82]. It would be interesting to generalise this to the continuous GPE and lattice solitons.

Other areas of interest include generalisations to fermions instead of bosons, disordered lattices, bound states, spin properties, quantum features, coupled transport, interferometry and even analogues of solid state systems. These are just a few areas of future research where our work can find new and useful applications.

Appendix A

Numerical Methods

Here the methods of numerical integration used in this thesis are described. In the continuous case, a split-step method is used for Eq. 2.20 in which the linear terms are integrated spectrally and the nonlinear terms using a second-order Runge-Kutta method. The discrete model is integrated using a symplectic method. Both these methods are detailed below.

A.1 Numerical Methods for Continuous Model

A.1.1 Runge-Kutta methods

Euler's method is described as

$$y_{n+1} = y_n + hf\left(t_n, y_n\right) \tag{A.1}$$

Here, the solution is moved from t_0 to $t_1 = t_0 + h$ where h is the step-size, and is determined by a single-step. This increases the error of the solution. The error (ie

the difference between the exact solution and the one given by Euler's method) is $O(h^2)$.

The second-order Runge-Kutta method uses an intermediate step to reduce this error. The values at this midpoint are used to evaluate the full step. This reduces the error to $O(h^3)$ [104]. An example of a second-order Runge-Kutta method is:

$$\begin{aligned} k_1 &= hf\left(t_n, y_n\right) \\ k_2 &= hf\left(t_n + \frac{1}{2}h, y_n + \frac{1}{2}k_1\right) \\ y_{n+1} &= y_n + k_2 \end{aligned} \tag{A.2}$$

A fourth order Runge-Kutta method can be given by generalising this approach further, in which four evaluations are used for each term [105]:

$$\begin{aligned} k_1 &= hf\left(t_n, y_n\right) \\ k_2 &= hf\left(t_n + \frac{1}{2}h, y_n + \frac{1}{2}k_1\right) \\ k_3 &= hf\left(t_n + \frac{1}{2}h, y_n + \frac{1}{2}k_2\right) \\ k_4 &= hf\left(t_n + h, y_n + k_3\right) \\ y_{n+1} &= y_n + \frac{1}{6}k_1 + \frac{1}{3}k_2 + \frac{1}{3}k_3 + \frac{1}{6}k_4 \end{aligned} \tag{A.3}$$

This reduces the error further to $O(h^5)$ [104]. This can be generalised further but the second-order and fourth-order Runge-Kutta methods are the most common ones. The second-order Runge-Kutta method is used in the continuous model in this thesis since the split step operation introduces a computational error of similar size.

A.1.2 Split-step method

The Gross-Pitaevskii (GP) equation, as used for the continuous model can be written as:

$$\frac{\partial u}{\partial t} = \mathcal{L}u + \mathcal{N}u \tag{A.4}$$

where $\mathcal{N}$ is a nonlinear operator, describing the potential, nonlinear and dissipative terms, and $\mathcal{L}$ is a linear operator describing the spatial derivatives, or the diffraction term. This can be integrated over a time-step dt to give

$$\begin{aligned} u\left(t+dt\right) &\approx \exp\left(\left(\mathcal{L}+\mathcal{N}\right)dt\right)u(t) \\ &\approx \exp\left(\mathcal{L}dt\right)\exp\left(\mathcal{N}dt\right)u(t) \end{aligned} \tag{A.5}$$

This is not an exact solution. An error is introduced due to the operators not commutating. This can be minimised by rearranging the equation like so:

$$u\left(t+dt\right) \approx \exp\left(\frac{\mathcal{L}}{2}dt\right)\exp\left(\mathcal{N}dt\right)u(t)\exp\left(\frac{\mathcal{L}}{2}dt\right) \tag{A.6}$$

In Eq. A.6, a half step is first taken with $\mathcal{L}$, the a full step is taken with $\mathcal{N}$ and finally a second half-step is taken with $\mathcal{L}$.

Splitting up the operators in such a way allows the separate parts of the equation to be solved fairly easily. The linear parts can be solved spectrally by using fast Fourier transforms to the frequency domain. The inverse Fourier transform is then used to go back to the time domain. The nonlinear part of the equation has no spatial dependence, and so can be solved using a Runge-Kutta method. For this thesis, a second-order Runge-Kutta method (as in Eq. A.2) was sufficient enough for this.

A.2 Symplectic Method for Discrete Model

With the wavefunction split into real and imaginary parts (i.e. $z = a + ib$), the DNLSE can be written as

$$\begin{aligned} \dot{a}_n &= -\left(a_n^2 + b_n^2\right) b_n - \left(b_n + b_{n-1}\right) \\ \dot{b}_n &= \left(a_n^2 + b_n^2\right) a_n + \left(a_n + a_{n-1}\right) \end{aligned} \tag{A.7}$$

from the Hamiltonian

$$H\left(a,b\right) = \sum_n \frac{1}{4}\left(a_n^2 + b_n^2\right)^2 + \sum_n \left(a_n a_{n+1} + b_n b_{n+1}\right) \tag{A.8}$$

This system has two integrals of motion as it conserves both the energy H and the density

$$D\left(a,b\right) = \frac{1}{2}\sum_n \left(a_n^2 + b_n^2\right) \tag{A.9}$$

The Hamiltonian is split into two parts, ie $H = H_1 + H_2$, where

$$H_1 = \sum_n \frac{1}{4}\left(a_n^2 + b_n^2\right)^2 \tag{A.10}$$

and

$$H_2 = \sum_n \left(a_n a_{n+1} + b_n b_{n+1}\right) \tag{A.11}$$

The operators $e^{\tau L_{\mathcal{A}}}$ and $e^{\tau L_{\mathcal{B}}}$ can be found analytically (see [106]). From this splitting we construct the second-order symplectic integrator, known as the leap-frog or Verlet integrator (see, for example, [107]):

$$Y_2\left(\tau\right) = e^{\frac{\tau}{2}L_{\mathcal{A}}} e^{\tau L_{\mathcal{B}}} e^{\frac{\tau}{2}L_{\mathcal{A}}} \tag{A.12}$$

Yoshida [81] showed that with appropriate coefficients $x_1 = \frac{1}{2-2^{1/3}}$ and $x_0 = -2^{1/3}x_1$ a fourth-order symmetric integrator can be constructed:

$$Y_4(\tau) = Y_2(x_1\tau)\, Y_2(x_0\tau)\, Y_2(x_1\tau) \tag{A.13}$$

We have used this algorithm when the conservation of energy and atomic density is required.

Bibliography

[1] S.N. Bose, Z. Phys. **26**, 178 (1924)

[2] A. Einstein, Sitzungsber. K. Preuss. Akad. Wiss., Phys. Math. Kl. **261** (1924)

[3] A. Einstein, Sitzungsber. K. Preuss. Akad. Wiss., Phys. Math. Kl. **3** (1925)

[4] F. London, Phys. Rev. **54**, 947954 (1938)

[5] M. H. Anderson, J. R. Ensher, M. R. Matthews, C. E. Wieman, and E A Cornell, Science, **269**, 198 (1995)

[6] K. B. Davis, M.-O. Mewes, M. R. Andrews, N. J. Van Druten, D. S. Durfee, D. M. Kurn and W. Ketterle, Phys. Rev. Lett. **75**, 3969 (1995)

[7] E. A. Cornell and C. E. Wieman, Rev. Mod. Phys. **74**, 175 (2002)

[8] W. Ketterle, Rev. Mod. Phys. **74**, 1131 (2002)

[9] O. Morsch and M. Oberthaler, Rev. Mod. Phys. **78**, 179 (2006)

[10] P. J. Y. Louis, E. A. Ostrovskaya, C. M. Savage and Y. S. Kivshar, Phys. Rev. A **67**, 013602 (2003)

[11] N. K. Efremidis and D. N. Christodoulides, Phys. Rev. A **67**, 063608 (2003)

[12] J. S. Russell, Report of the 14th Meeting of the British Association for the Advancement of Science, Plates XLVIILVII, pp. 311390 (1845)

[13] L. Khaykovich, F. Scherck, G. Ferrari, T. Bourdel, J. Cubizolles, L.D. Carr, Y. Castin and C. Salomon, Science **296**, 1290 (2002)

[14] K. E. Strecker, G. B. Partridge, A.G. Truscott and R.G. Hulet, Nature (London) **417**, 150 (2002)

[15] B. Eiermann, Th. Anker, M. Albiez, M. Taglieber, P. Treutlein, K.-P. Marzlin and M. K. Oberthaler, Phys. Rev. Lett. **92**, 230401 (2004)

[16] S. Burger, K. Bongs, S. Dettmer, W. Ertmer and K. Sengstock, Phys. Rev. Lett. **83**, 5198 (1999)

[17] A. L. Jones, J. Opt. Soc. Am. **55**, 261 (1965)

[18] S. Somekh, E. Garmire, A. Yariv, H. L. Garvin and R. G. Hunsperger, Appl. Phys. Lett. **22**, 46 (1973)

[19] D. N. Christodoulides and R. I. Joseph, Opt. Lett. **13**, 794 (1988)

[20] H. S. Eisenberg, Y. Silberberg, R. Morandotti, A. R. Boyd and J. S. Aitchison, Phys. Rev. Lett. **81**, 3383 (1998)

[21] F. Lederer, G. I. Stegeman, D. N. Christodoulides, G. Assanto, M. Segev and Y. Silberberg, Phys. Rep. **463**, 1 (2008)

[22] F. Dalfovo, S. Giorgini, L. P. Pitaevskii and S. Stringari, Rev. Mod. Phys. **71**, 463 (1999)

[23] N. N. Bogoliubov, J. Phys. (Moscow) **11**, 23 (1947)

[24] J. Weiner, *Cold and Ultracold Collisions in Quantum Microscopic and Mesoscopic Systems*, Cambridge University Press, 2003

[25] T. Köhler, K. Góral and P. S. Julienne, Rev. Mod. Phys. **78**, 1311 (2006)

[26] A. J. Moerdijk, B. J. Verhaar and A. Axelsson, Phys. Rev. A **51**, 4852 (1995)

[27] J. L. Roberts, N. R. Claussen, S. L. Cornish and C. E. Wieman, Phys. Rev. Lett. **85**, 728 (2000)

[28] C. Kittel, *Introduction to Solid State Physics* (Wiley; 7th edition, 1995)

[29] H. Sakaguchi and B. A. Malomed, J. Phys. B, **37**, 1443 (2004)

[30] A. Trombettoni and A. Smerzi, Phys. Rev. Lett. **86**, 002353 (2001).

[31] W. Kohn, Phys. Rev. **115**, 809 (1959)

[32] H. Hennig and R. Fleischmann, Phys. Rev. A **87**, 033605 (2013).

[33] R. Franzosi, R. Livi, G.-L.Oppo, and A. Politi, Nonlinearity **24**, R89 (2011)

[34] H. Hennig, T. Neff and R. Fleischmann, Phys. Rev. E **93**, 032219 (2016)

[35] R. Livi, R. Franzosi, and G.-L. Oppo, Phys. Rev. Lett. **97**, 060401 (2006)

[36] S. Franke-Arnold, J. Leach, M. J. Padgett, V. E. Lembessis, D. Ellinas, A. J. Wright, J. M. Girkin, P. Ohberg, and A. S. Arnold, Opt. Express **15**, 8619 (2007)

[37] L. Amico, A. Osterloh and F. Cataliotti, Phys. Rev. Lett. **95**, 063201 (2005)

[38] K. Henderson, C. Ryu, C. MacCormick and M. G. Boshier, New Journal of Physics **11**, 043030 (2009)

[39] S. Moulder, S. Beattie, R. P. Smith, N. Tammuz, and Z. Hadzibabic, Phys. Rev. A **86**, 013629 (2012)

[40] M. Johansson and S. Aubry, Nonlinearity **10**, 1151 (1997)

[41] Y. S. Kivshar and D. K. Campbell, Phys. Rev. E **48**, 3077 (1993); J. Gòmez-Gardeñes, L. M. Floria, M. Peyrard and A. R. Bishop, Chaos **14**, 1130 (2004)

[42] R. Franzosi, R. Livi, and G.-L. Oppo, J. Phys. B **40** 1195 (2007)

[43] J. L. Helm, T. P. Billam and S. A. Gardiner, Phys. Rev. A **85**, 053621 (2012)

[44] J. L. Helm, S. J. Rooney, C. Weiss, and S. A. Gardiner, Phys. Rev. A **89**, 033610 (2014)

[45] J. L. Helm, S. L. Cornish and S. A. Gardiner, Phys. Rev. Lett. **114**, 134101 (2015)

[46] J. Holmer, J. Marzuola and M. Zworski, Commun. Math. Phys. **274**, 187 (2007)

[47] J. Holmer, J. Marzuola and M. Zworski, J. Nonlinear Sci. **17**, 349 (2007)

[48] J. Polo and V. Ahufinger, Phys. Rev. A **88**, 053628 (2013)

[49] A. D. Martin and J. Ruostekoski, New J. Phys. **14**, 043040 (2012)

[50] C. Lee and J. Brand, Europhys. Lett. **73**, 321 (2006)

[51] T. Ernst and J. Brand, Phys. Rev. A **81** (2010)

[52] V. A. Brazhnyi and M. Salerno, Phys. Rev. A, **83**, 053616 (2011)

[53] V. A. Brazhnyi, C. P. Jisha and A. S. Rodrigues, Phys. Rev. A, **87**, 013609 (2013)

[54] D. S. Hall, M. R. Matthews, J. R. Ensher, C. E. Wieman, and E. A. Cornell, Phys. Rev. Lett. **81**, 1539 (1998)

[55] P. Öhberg and S. Stenholm, Phys. Rev. A **57**, 1272 (1998)

[56] S. Hooley and K. A. Benedict, Phys. Rev. A **75**, 033621 (2007)

[57] J. Ruostekoski and Z. Dutton, Phys. Rev. A **76**, 063607 (2007)

[58] A. Gubeskys, B. A. Malomed, and I. M. Merhasin, Phys. Rev. A **73**, 023607 (2006)

[59] S. K. Adhikari and B. A. Malomed, Phys. Rev. A, **77**, 023607 (2008)

[60] B. A. Malomed, D. J. Kaup, and R. A. Van Gorder, Phys. Rev. E **85**, 026604 (2012)

[61] M. Matuszewski, B. A. Malomed, and M. Trippenbach, Phys. Rev. A **76**, 043826 (2007)

[62] Sk. Golam Ali and B. Talukdar, Annals of Physics **324**, 1194 (2009)

[63] H. A. Cruz, V. A. Brazhnyi, V. V. Konotop, G. L. Alfimov, and M. Salerno, Phys. Rev. A **76**, 013603 (2007)

[64] F. Kh. Abdullaev, A. Gammal, M. Salerno, and L. Tomio, Phys. Rev. A, **77**, 023615 (2008).

[65] Z. Shi, K. J. H. Law, P. G. Kevrekidis, and B. A. Malomed, Phys. Lett. A **372**, 4021 (2008)

[66] S. K. Adhikari, J. Phys. B **44**, 075301 (2011)

[67] Z. M. He, D. L. Wang, J. W. Ding, and X. H. Yan, Eur. Phys. J. D **66**, 139 (2012)

[68] V. M. Perez-Garcia and J. B. Beitia, Phys. Rev. A. **72**, 033620 (2005)

[69] Y. Takasu, K. Maki, K. Komori, T. Takano, K. Honda, M. Kumakura, T. Yabuzaki, and Y. Takahashi, Phys. Rev. Lett. **91**, 040404 (2003)

[70] T. Fukuhara, S. Sugawa, and Y. Takahashi, Phys. Rev. A **76**, 051604(R) (2007)

[71] S. Sugawa, R. Yamazaki, S. Taie, and Y. Takahashi, Phys. Rev. A **84**, 011610(R) (2007)

[72] T. Fukuhara, S. Sugawa, Y. Takasu, and Y. Takahashi, Phys. Rev. A **79**, 021601(R) (2009)

[73] K. Kasamatsu and M. Tsubota, J. Low Temp. Phys. **150**, 599 (2008).

[74] K. Enomoto, M. Kitagawa, K. Kasa, S. Tojo, and Y. Takahashi, Phys. Rev. Lett. **98**, 203201 (2007)

[75] M. Kitagawa, K. Enomoto, K. Kasa, Y. Takahashi, R. Ciurylo, P. Naidon, and P. S. Julienne, Phys. Rev. A **77**, 012719 (2008)

[76] R. Ciurylo, E. Tiesinga, and P. S. Julienne, Phys. Rev. A **71**, 030701(R) (2005)

[77] K. Enomoto, K. Kasa, M. Kitagawa, and Y. Takahashi, Phys. Rev. Lett. **101**, 203201 (2008)

[78] M. Borkowski, R. Ciurylo, P. S. Julienne, S. Tojo, K. Enomoto, and Y. Takahashi, Phys. Rev. A **80**, 012715 (2009)

[79] M. Borkowski, R. Ciurylo, P. S. Julienne, R. Yamazaki, H. Hara, K. Enomoto, S. Taie, S. Sugawa, Y. Takasu, and Y. Takahashi , Phys. Rev. A **84**, 030702 (2011)

[80] G. Thalhammer, G. Barontini, L. De Sarlo, J. Catani, F. Minardi, and M. Inguscio, Phys. Rev. Lett **100**, 210402 (2008)

[81] H. Yoshida, Phys. Lett. A **170**, 262 (1990)

[82] S. Iubini, R. Franzosi, R. Livi, G.-L.Oppo, and A. Politi, New Journal of Physics **15**, 023032 (2013)

[83] A. Marte, T. Volz, J. Schuster, S. Dürr, G. Rempe, E. G. M. van Kempen, and B. J. Verhaar, Phys. Rev. Lett. **89**, 283202 (2002)

[84] G. Modugno, M. Modugno, F. Riboli, G. Roati, and M. Inguscio, Phys. Rev. Lett. **89**, 190404 (2002)

[85] H. Wang, A. N. Nikolov, J. R. Ensher, P. L. Gould, E. E. Eyler, W. C. Stwalley, J. P. Burke, Jr., J. L. Bohn, C. H. Greene, E. Tiesinga, C. J. Williams, and P. S. Julienne, Phys. Rev. A **62**, 052704 (2000)

[86] J. Catani, L. De Sarlo, G. Barontini, F. Minardi, and M. Inguscio, Phys. Rev. A **77**, 011603(R) (2008)

[87] I. Bloch, J. Dalibard, and W. Zwerger, Rev. Mod. Phys. **80**, 885 (2008)

[88] M. Matuszewski, W. Krolikowski, M. Trippenbach, and Y. S. Kivshar, Phys. Rev. A **73**, 063621 (2006)

[89] J. Gomez-Gardenes, L. M. Floria, M. Peyrard, and A. R. Bishop, Chaos **14**, 1130 (2004)

[90] L. Fallani, F. S. Cataliotti, J. Catani, C. Fort, M. Modugno, M. Zawada, and M. Inguscio, Phys. Rev. Lett. **91**, 240405 (2003)

[91] S. Flach and A. V. Gorbach, Phys. Rep. **467**, 1 (2008)

[92] M. Salerno, Phys. Rev. A **72**, 063602 (2005)

[93] T. Gericke, P. Würtz, D. Reitz, T. Langen and H. Ott, Nat. Phys. **4**, 949 (2008)

[94] V. A. Brazhnyi, V. V. Konotop, V. M. Pérez-García and H. Ott, Phys. Rev. Lett. **102**, 144101 (2009)

[95] B. A. Malomed, J. Opt. Soc. Am. B, **31**, 2460 (2014)

[96] C. M. Bender and S. Boettcher, Phys. Rev. Lett. **80**, 5243 (1998)

[97] Y.-J. He and B. A. Malomed, in "Spontaneous Symmetry Breaking, Self-Trapping, and Josephson Oscillations", ed. by B. A. Maolomed (Springer, Heidelberg, 2013), page 125; V. V. Konotop, J. Yang, and D. A. Zezyulin, Rev. Mod. Phys. **88**, 35002 (2016)

[98] R. J. C. Spreeuw, T. Pfau, U. Janicke, and M. Wilkens, Europhys. Lett. **32**, 469 (1995); N. P. Robins, P. A. Altin, J. E. Debs, and J. D. Close, Phys. Rep. **529**, 265 (2013)

[99] D. A. Zezyulin and V. V. Konotop, Phys. Rev. A **94**, 043853 (2016)

[100] M. Greiner, O. Mandel, T. Hänsch and I. Bloch, Nature (London) **419**, 51 (2002).

[101] L. Pezzé and A. Smerzi, Phys. Rev. Lett. **102**, 100401 (2009)

[102] D. Witthaut, F. Trimborn, H. Hennig, G. Kordas, T. Geisel and S. Wimberger, Phys. Rev. A **83**, 063608 (2011)

[103] G. Kordas, S. Wimberger and D. Witthaut, Phys. Rev. A **87**, 043618 (2013)

[104] W. H. Press, B. P. Flannery, S. A. Teukolsky and W. T. Vetterling, *Numerical Recipies: The Art of Scientific Computing*, Cambridge University Press, 1986

[105] M. W. Z. Kutta, Math. u. Phys. **46**, 435 (1901)

[106] E. Gerlach, J. Meichsner and C. Skokos, Eur. Phys. J. Special Topics **225**, 1103 (2016)

[107] E. Hairer, C. Lubich and G.Wanner, *Geometric Numerical Integration. Structure-Preserving Algorithms for Ordinary Differential Equations Springer Series in Computational Mathematics*, Vol. 31 (Springer, New York, 2002)